ÉCOLE POLYTECHNIQUE
FÉDÉRALE DE LAUSANNE

Bi-directional Photogoniometer for the Assessment of the Luminous Properties of Fenestration Systems

CTI Project - Scientific Report

Laboratoire d'Energie solaire et de Physique du bâtiment - ITB - DA

May 2000

ÉCOLE POLYTECHNIQUE
FÉDÉRALE DE LAUSANNE

Bi-directional Photogoniometer for the Assessment of the Luminous Properties of Fenestration Systems

Scientific Report

INSTITUTIONAL PARTNER		INDUSTRIAL PARTNER	
LESO-PB / EPFL		Baumann-Hüppe AG	
Prof.J.-L.Scartezzini	Project Leader	H.-P. Baumann	Consultant
M. Andersen	Physics Eng.	R. Brunkhorst	Head of Dept.
L. Michel, PhD	Physics Eng.	H. Coldewey	Head of Dept.
C. Roecker	Electrical Eng.		

CTI Project No. 3661.2

Laboratoire d'Energie solaire et de Physique du bâtiment - ITB - DA May 2000

SUMMARY

Most energy saving applications of advanced fenestration systems (solar blinds, novel types of glazing and daylight redirecting devices) require a precise knowledge of their directional light transmission features. These photometric properties can be described by a Bi-directional Transmission Distribution Function (BTDF) whose experimental assessment requires appropriate equipment.

A novel bi-directional transmission photogoniometer, based on digital imaging techniques, was designed and set up for that purpose. The apparatus takes advantage of a modern video image capturing device (CCD digital camera) as well as of powerful image analysis software (pattern recognition) to considerably reduce the scanning time of a BTDF measurement, in comparison to existing devices that use a conventional approach (mobile photometer).

A detailed calibration and validation procedure was used to obtain optimal experimental accuracy for the device during the assessment of BTDF data. It included a spectral, a photometric and a geometrical calibration of the digital video system, as well as several additional corrections, leading to an overall relative accuracy better than 11% for BTDF data.

A special effort was made to improve the user-friendliness of BTDF measurement by facilitating the data acquisition and treatment (definition of a data acquisition and electronic data format) and by offering different possibilities of BTDF visualisation (hemispherical representation, axonometric view of photometric solids, C-planes).

Overall, the photometric equipment was used to assess the BTDFs of more than 20 novel fenestration products of the industrial partner of the project (Baumann-Hüppe Storen AG). The experimental data produced was successfully used by the company to optimise the visual and energy saving performance of their products, which confirms the adequacy of the novel bi-directional photogoniometer for practical building applications.

RESUME

La connaissance précise des propriétés de transmission lumineuse de composants de vitrage avancés (protections solaires, systèmes d'éclairage naturel) est nécessaire pour atteindre des économies d'énergie effectives dans la pratique, ainsi qu'une amélioration du confort visuel des usagers. Ces caractéristiques photométriques sont décrites par la fonction bidirectionnelle de distribution du facteur de transmission (BTDF) qui ne peut être mesurée qu'à l'aide d'un équipement photométrique idoine.

Un photogoniomètre bidirectionnel de mesure de transmission basé sur des techniques d'imagerie numérique a été conçu et réalisé dans le cadre de ce projet. Grâce à l'utilisation d'une caméra vidéo CCD et de logiciels de traitement digital d'images performants, ce dispositif permet de réduire considérablement le temps nécessaire à l'acquisition de la fonction BTDF de matériaux de vitrage par comparaison avec des dispositifs conventionnels faisant appel à des photomètres mobiles.

Des procédures détaillées de calibration et de validation ont été appliquées au photogoniomètre en vue de réduire autant que possible l'erreur expérimentale associée à la mesure de la BTDF. Grâce à une calibration spectrale, photométrique et géométrique, ainsi qu'à un certain nombre de corrections additionnelles, la précision expérimentale de la mesure de la BTDF a pu être amenée à une valeur inférieure à 11% en termes relatifs.

Un effort important a été consacré, par ailleurs, aux développements d'interfaces conviviales pour ce qui concerne l'acquisition et le traitement des données photométriques: un format de mesures (choix des directions d'incidence et d'émergence) ainsi qu'un format d'archivage électronique (fichiers informatiques) ont ainsi été définis. Différentes possibilités de visualisation de la fonction BTDF (représentation hémisphérique, vue axonométrique du solide photométrique, plans perpendiculaires) ont été rendues possibles, par ailleurs, grâce à ces efforts.

Le photogoniomètre bidirectionnel a été utilisé pour déterminer les propriétés lumineuses de transmission de plus de 20 matériaux de fenêtre innovants, produits par le partenaire industriel du projet (Baumann-Hüppe Storen AG). Ces données photométriques ont permis à ce dernier d'améliorer encore et d'optimiser les prestations de confort visuel et d'économies d'énergie de ces produits, confirmant ainsi l'adéquation de ce dispositif aux besoins de l'industrie du bâtiment.

TABLE OF CONTENTS

1. INTRODUCTION 1

1.1 AIMS OF THE PROJECT 1
1.2 ADOPTED APPROACH 2
1.3 STRUCTURE OF REPORT 3

2. BI-DIRECTIONAL PHOTOMETRIC MEASUREMENTS 5

2.1 DEFINITION OF PHOTOMETRIC QUANTITIES 5
2.2 CONFIGURATION OF EXISTING DEVICES 7
2.3 USE OF DIGITAL IMAGING TECHNIQUES 9

3. BI-DIRECTIONAL TRANSMISSION PHOTOGONIOMETER 11

3.1 DESCRIPTION OF THE EQUIPMENT 11
3.1.1 General Functioning Principle 11
3.1.2 Description of Components 12
3.2 CALIBRATION PROCEDURES 19
3.2.1 Spectral Calibration 19
3.2.2 Photometric Calibration 20
3.2.3 Geometric Calibration 22
3.2.4 Additional Corrections 27
3.3 DEVICE COMMAND AND DATA PROCESSING 37
3.3.1 Piloting Software 37
3.3.2 Image Acquisition and Processing 40
3.3.3 Data Conversion 46
3.3.4 Experimental Validation 51
3.4 VALORISATION OF DATA 59
3.4.1 Integral Data Set 59
3.4.2 Representation of Photometric Solids 63
3.4.3 Application Case Studies 66

4. CONCLUSION 77

REFERENCES 81

ANNEXES

Annex A: Plan and Cross-Section View of the Bi-directional Photogoniometer A-1
Annex B: Data Format of Bi-directional Measurements B-1
Annex C: Solar blinds, manufactured by Baumann-Hüppe AG, characterised through BTDF measurements C-1

1. INTRODUCTION

1.1 AIMS OF THE PROJECT

As a consequence of a larger consensus regarding the concept of sustainable development in buildings, daylight and solar radiation control through fenestration systems nowadays receive greater attention both in research [Wir97] and practice [CSD97]. Advanced fenestration systems, which include novel solar blinds, new glazing materials and daylight re-directing devices can play a significant role in this field [Wir99].

Efficient collection and/or redistribution of direct sunlight for optimal visual and thermal comfort conditions in buildings [Rav95], remains one of the most important objectives of fenestration systems. They can improve the penetration of daylight into deep rooms, which, among others, reduces electricity consumption, and they can also lead to larger solar gains in winter and lower solar loads in summer, which again reduces non renewable energy consumption.

For this, the directional photometric properties of fenestration systems must be fully known, just like those of lighting fixtures [IES93] [SLG92] (cf. Fig.1.1).

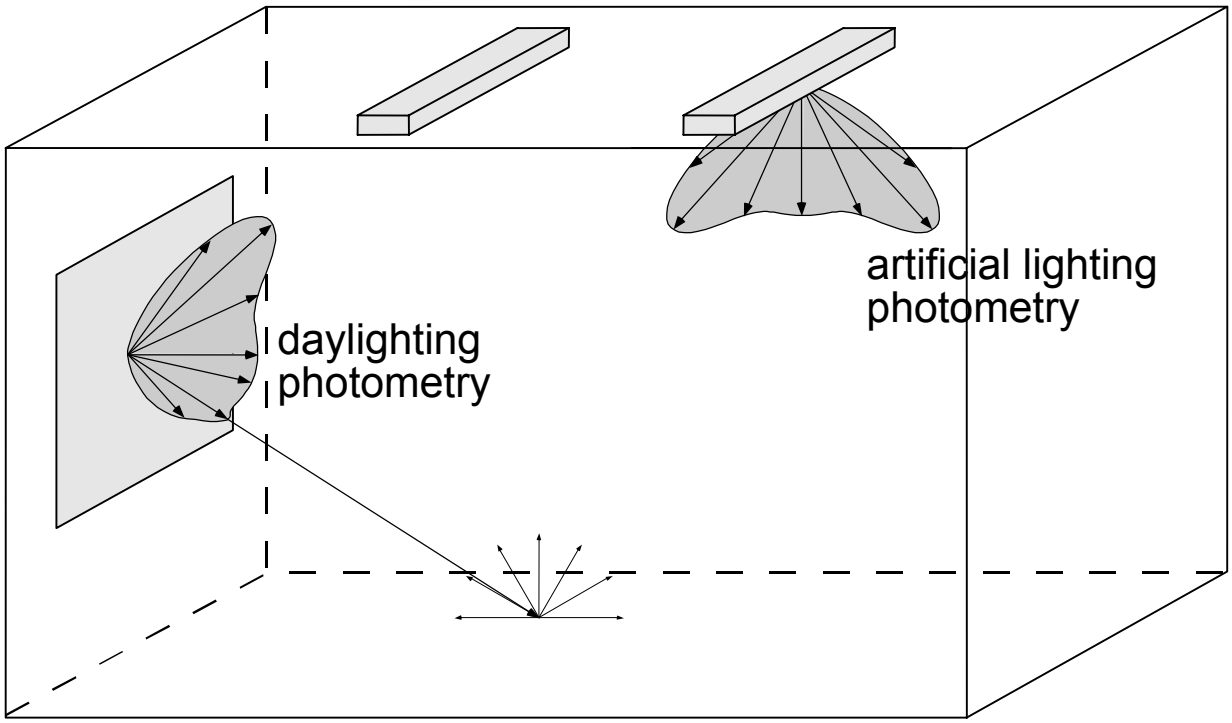

Fig. 1.1. Directional photometric properties of fenestration systems (left) and lighting fixtures (right) necessary to assess the distribution of solar radiation and light into buildings

The aim of this project is to set up experimental equipment (a bi-directional photogoniometer) for efficient measuring and characterising of light transmission properties of such building components. These properties, described by the Bi-directional Transmission Distribution Function (BTDF), are intended to be used by the building industry:

- to optimise the luminous performance of innovative solutions for fenestration systems

- to facilitate the choice of different industrial products (solar blinds, novel kinds of glazing, etc.) during the building construction process

- as a common physical description of the photometric properties of fenestration and glazing materials (similar to that of lighting fixtures)

A novel bi-directional photogoniometer based on digital imaging techniques was designed and set up for this purpose [And00] [Sca97]. After a detailed calibration and validation procedure, it was used to assess the BTDF of several new fenestration products produced by the company Baumann-Hüppe (industrial partner of the project). The BTDF data, reported in a technical report [And 99], were used by the company to optimise and improve further the visual and thermal performance of their products.

1.2 ADOPTED APPROACH

Several bi-directional photogoniometers have recently been developed to perform BTDF measurements of glazing and fenestration materials [Api94] [Bak95] [Bre98]. Most are based on a conventional design (cf. § 2.2) and use a movable photo sensor to track and measure in all possible directions the outgoing luminance of the light flux transmitted through the sample.

Their performance is accurate and reliable, but they show two significant drawbacks:

- they are time consuming because numerous movements of the mobile photo sensor are required to achieve an appropriate angular resolution

- glazing materials with a high dynamical luminance range cause serious technical difficulties (local refinement of angular resolution, possible saturation of the illuminance sensor, etc.).

To overcome these difficulties, the novel type of bi-directional photogoniometer developed within the framework of this project uses advanced digital imaging techniques [Sca97]. Several major advantages are thus obtained:

- a significant reduction of the BTDF data processing time (2-4 minutes instead of several hours for one incident angular direction)

- BTDF data based on quasi-continuous knowledge of the transmitted hemisphere (only discretised by the pixellisation of the images)

- handling of material samples showing large dynamical range of luminances in transmission ("sharp" transmission figures).

Several other significant services are offered by this device thanks to its data treatment capability, made possible by the use of digital image handling software: correction of error sources and final graphical representation are more easily made available. Several critical calibration procedures before photogoniometer operation are required for this, however.

1.3 STRUCTURE OF REPORT

This scientific report gives a description of the equipment, which was submitted to several calibration procedures, and an assessment of potential error sources [And00]. A comparison of BTDF data measured by several photogoniometers including this device was carried out on an international basis [Ayd97] [Ayd99].

Chapter 2 gives an overview of the configuration of existing bi-directional photogoniometers based on conventional techniques. A definition of the photometric quantities involved in the experimental procedures is given as well.

Chapter 3 describes the novel equipment and gives a clear understanding of the calibration procedures used to set up the different operating functions of the device. The final data treatment, as well as the graphical representation of BTDF data, are outlined in this chapter.

The Annexes to this report illustrate the photometric features of advanced glazing materials. A comprehensive technical report shows similar figures for a large series of industrial products, measured for the project's partner (Baumann-Hüppe Storen AG). This illustrates the suitability of the new device for practical applications.

2. BI-DIRECTIONAL PHOTOMETRIC MEASUREMENTS

2.1 DEFINITION OF PHOTOMETRIC QUANTITIES

Directional propagation of light through transparent or diffusing dielectric materials can be described by the Bi-directional Transmission Distribution Function (BTDF), also designated by Luminance Coefficient q [sr^{-1}] in the CIE corresponding nomenclature [Ayd99] [CIE98].

Such a function, illustrated by Fig. 2.1, is given for homogeneous and achromatic materials by the equation (2-1):

$$BTDF(\theta_1,\phi_1,\theta_2,\phi_2) = \frac{L_2(\theta_1,\phi_1,\theta_2,\phi_2)}{L_1(\theta_1,\phi_1)\cos\theta_1 d\omega_1}\left[sr^{-1}\right] \qquad (2\text{-}1)$$

where the corresponding symbols are defined as :

(θ_1, ϕ_1)	Polar co-ordinates of incoming light flux [°]
(θ_2, ϕ_2)	Polar co-ordinates of emerging (transmitted) light flux [°]
$L_1(\theta_1, \phi_1)$	Luminance of element of incoming light flux [cd m^{-2}]
$L_2(\theta_1, \phi_1, \theta_2, \phi_2)$	Luminance of emerging (transmitted) element of light flux [cd m^{-2}]
$d\omega_1$	Solid angle subtended by incoming light flux [sr]

For practical reasons, the following equation is preferred, as an equivalent definition of the BTDF function:

$$BTDF(\theta_1,\phi_1,\theta_2,\phi_2) = \frac{L_2(\theta_1,\phi_1,\theta_2,\phi_2)}{E_1(\theta_1)}\left[\frac{cd}{m^2 lx}\right] \qquad (2\text{-}2)$$

where $E_1(\theta_1)$ represents the illuminance on the sample plane due to the incident light flux. The corresponding beam is generally collimated, showing a constant illuminance on the section of the fenestration material sample.

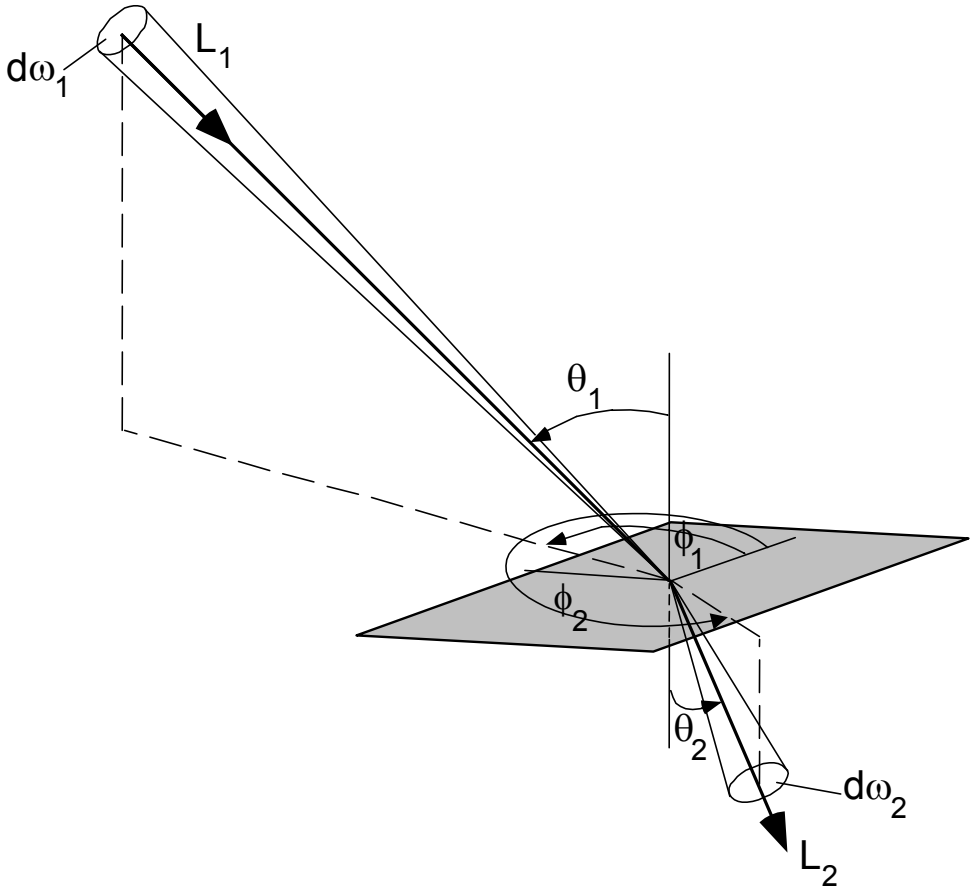

Fig. 2.1. Photometric and geometrical quantities used to define the bi-directional transmission distribution function (BTDF) of a fenestration material

This other BTDF formulation is closer to the CIE nomenclature, which defines the luminance coefficient q [$cd \cdot m^{-2} \cdot lx^{-1}$] as "the quotient of the luminance of a surface element in a given direction, by the illuminance incident on the sample".

Some authors restrict the application of the BTDF (or the luminance coefficient q) to scattered daylight, not taking into account the possibly existing regular component of transmitted light flux [Ayd97]. It is believed that this constraint was imposed by the difficulty of conventional photogoniometers to handle regular components, associated in general with a large dynamical luminance range ("peaky transmission" can not be easily handled by movable photo sensors). Video digital imaging techniques allow to overcome these experimental difficulties: both regular and diffuse components are, in consequence, taken into account for the definition and assessment of the BTDF within this project.

An analogous definition and expressions similar to equations (2-1) and (2-2) can be derived to define the Bi-directional Reflection Distribution Function (BRDF) of both opaque and diffusing building materials [NBS77]. This photometric quantity can, however, not be experimentally assessed by the bi-directional photogoniometer, but requires special equipment dedicated to the measurement of BRDF data.

The definitions of other relevant photometric quantities (e.g. illuminance, intensity, luminance) are given in a detailed manner in different references [SLG92] [IES93]: the reader is for instance referred to [Sca94], which contains a comprehensive glossary of photometric terminology.

2.2 CONFIGURATION OF EXISTING DEVICES

Serious effort has been made to develop bi-directional photogoniometric devices, capable of measuring BTDFs (and/or BRDFs) in an appropriate way. Various novel designs have been proposed with the aim to reduce the onerous scanning process required for monitoring hundreds of possible incoming and outgoing light flux directions on material samples for which BTDF data are needed.

One of the first bi-directional photogoniometers, designed for BTDF measurements of fenestration materials, was developed at Lawrence National Berkeley Laboratory (LBNL) in the late eighties [Pap88]. Fig. 2.2 illustrates this device, which is able to handle samples of about 40 x 40 cm.

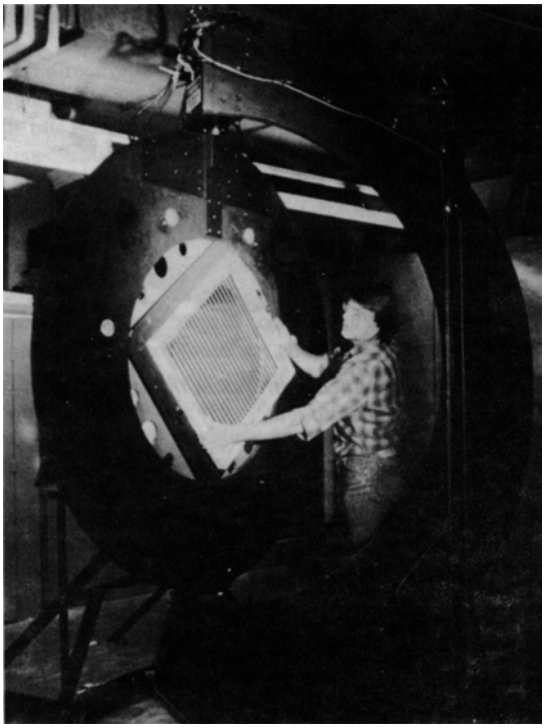

Fig. 2.2. View of the LBNL bi-directional photogoniometer for fenestration materials

Fig. 2.3 illustrates the measuring principles of this device: for the measurement of the luminance values of the light flux transmitted through the fenestration material, a photometric sensor is moved around, so that it points at the illuminated sample from different outgoing directions (θ_2, ϕ_2).

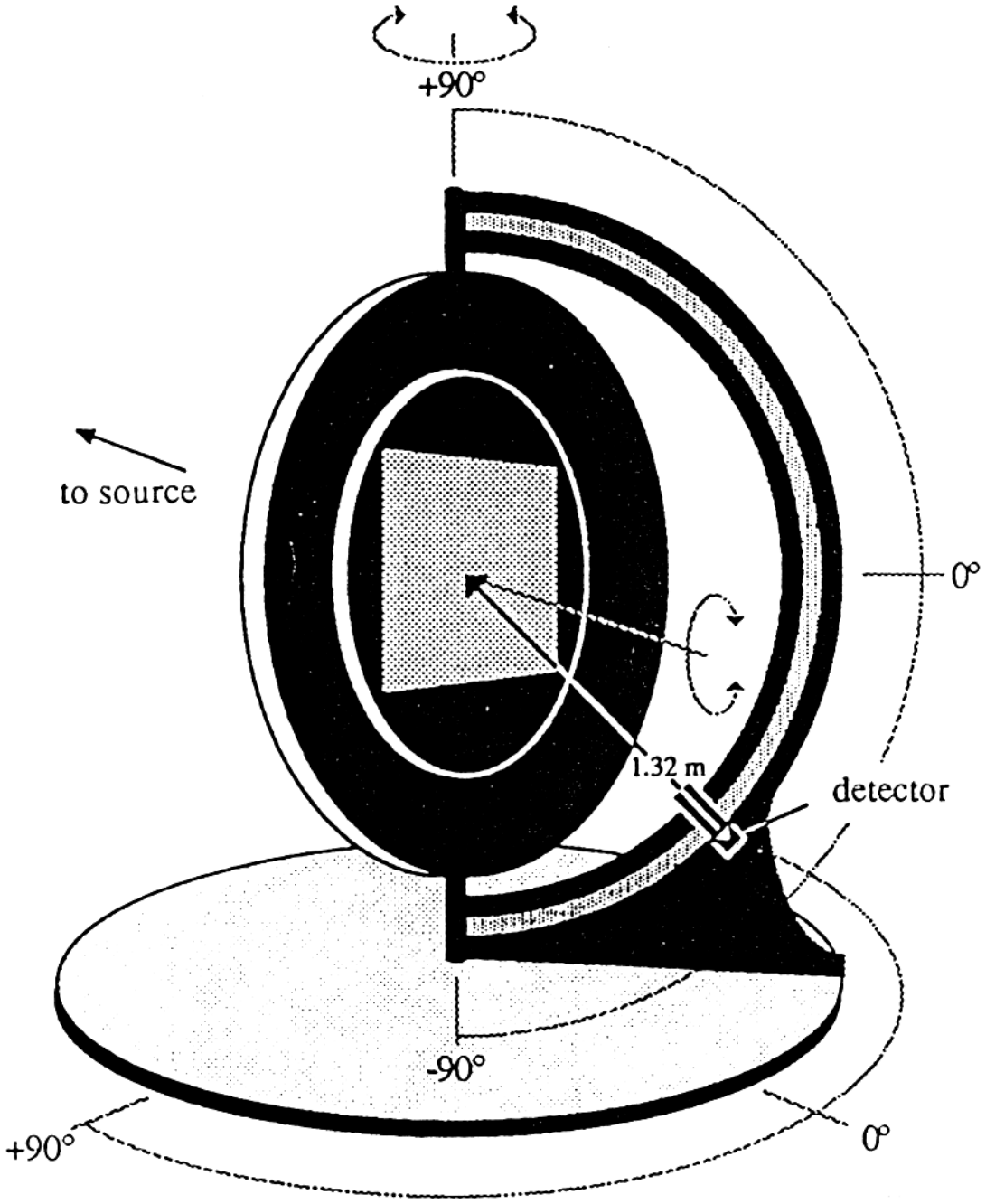

Fig. 2.3. Measurement principles of the LBNL photogoniometer, based on a movable photometric sensor

Mechanical movements around the main axis, driven by electrical motors, allow varying the directions (θ_1, ϕ_1) of the light rays impinging on the sample. A combination of all movements leads to a scanning of all possible incident and outgoing directions, which is necessary to gather a full set of BTDF data (generally more than 50'000 discrete values). This leads to significant drawbacks for the experimental assessment of BTDF data, which was discussed previously (cf. § 1.2): among them the considerable time required for a full BTDF data set handling is certainly the most significant.

Some other types of bi-directional photogoniometers dedicated to BTDF and/or BRDF data measurements of fenestration materials, were set up more recently: references [Api94], [Bak95], [Ayd97] and [Bre98] give a good overview of these photometric devices. Some of them were used in the framework of International Energy Agency Task 21 "Daylighting in Buildings" to compare BTDF data produced by different laboratories on an international basis [Ayd99].

Several experiment planning techniques are used for some photogoniometers to refine the angular resolution of BTDF data assessment around directions of high luminance dynamical range ("beaks" of transmission). This requires, however, full pre-scanning of the whole (2π) solid angle of the outgoing rays hemisphere to identify the corresponding "light peaks", increasing the time requested for the BTDF data processing [Api94].

Other data treatment techniques must be used to interpolate the BTDF for the full outgoing rays hemisphere, in order to account for the low resolution of angular directions, which is used to reduce the processing time [Pap88].

2.3 USE OF DIGITAL IMAGING TECHNIQUES

The use of video techniques, together with digital image handling software, has proven to be a very fruitful and encouraging approach in the field of photometry, especially since the advent of CCD image sensors [Och96]. Several authors have demonstrated the benefits of video digital techniques for the development of video-based luminance mappers [Pas94], visual comfort meters [Ber95] and sky luminance scanners [And98]; more recent works confirmed the adequacy of this technique for the assessment of the luminous performance of buildings [Mil95].

The use of a CCD video camera to assess bi-directional photometric properties of surface materials was already employed by Ward in 1992 [War92]. This device, which used a silver mirrored half-transparent hemisphere, was however designed to measure a few centimetre large samples; it had moreover to be based on an approximation of an ellipsoid by a hemisphere, because of construction constraints, which leads to heavy geometric corrections.

For all these devices, the overall video digital system must follow detailed calibration and correction procedures, which probably makes up the main difficulty of this approach. The reliability of the data assessment, together with the related accuracy, depend on the execution of these procedures, generally defined for the CCD camera as follows:

Spectral calibration

The CCD video camera has to be calibrated spectrally, which means that its spectral response has to be close to the human eye's spectral sensitivity $V(\lambda)$ [IES93]

Photometric calibration

Grey levels have to be converted into luminance values. These conversions depend on the integration time of the CCD camera. The image uniformity has to be verified by controlling that a uniform luminance distribution produces an image of equal grey values (CCD component sensitivity and lens effects).

Geometric calibration

The relation between the pixel co-ordinates of the final image (x, y) and the corresponding outgoing light ray directions (θ_2, ϕ_2) must be determined.

An overview of these procedures is given in the next chapter. Additional possible sources of error for the camera must be checked as well; including

- stability of electronic circuit responsible for the gain of the CCD camera
- sensitivity of the CCD sensor to ambient temperature
- reliability of the control of the main function parameters of the device (exposure time, aperture diameter, etc.).

Reference [And98] gives a detailed description of the handling of these sources of error.

The correction procedures concerning the other components of the photogoniometer are explained in § 3.2.4.

3. BI-DIRECTIONAL TRANSMISSION PHOTOGONIOMETER

3.1 DESCRIPTION OF THE EQUIPMENT

3.1.1 General functioning principle

The bi-directional photogoniometer has three major components:

- a calibrated light source that provides a collimated and spectrally optimal light beam
- a computer controlled movable mechanical support that allows modifying the incident light direction on the material sample
- a computer controlled "light detection device" that consists of a triangular flat projection screen associated to an image capturing CCD video camera.

Fig. 3.1 gives a view of the equipment, with its different parts dismantled for better comprehension. Fig. 3.2 gives a CAD representation of the bi-directional photogoniometer, which includes a calibrated light source placed above the photogoniometer and a light proof cage to avoid parasitic light reflections on the CCD video system. The overall equipment has benefited from the recent development of an automated heliodon (sun simulator), which has been operating satisfactorily since 1991 [Rhy91] at the LESO-PB/EPFL. Similar technology was used for the new photogoniometric device to design the optical and the robotic parts of the equipment (light source, motion control software, etc.).

Fig. 3.1. View of the bi-directional photogoniometer. The light detection device is mounted behind the adjustable moving plate and protected against parasitic light by a lightproof cache (placed on the floor for convenience). The CCD camera (absent in this picture) is fixed on the rotating ring at the cross mark.

3.1.2 Description of components

Light source

The light source is made of a short arc discharge lamp (OSRAM 2.5 kW HMI), which combines high luminous efficacy (96 Lm/W), a daylight close spectrum ($T_C \approx 5600$ K) and high colour rendering (Ra > 90). Its optical system is made of a floodlight projector, characterised by a hyperbolic mirrored reflector, a Fresnel front lens and a supplementary conic optical element, aimed to improve beam light collimating and illuminance uniformity on beam cross-sections [Sca94].

The light source is located 6 meters above the moving plate of the photogoniometer, which holds the sample during the measurements. All the equipment is placed at the centre of a 5 x 5 x 8 meter black chamber, to avoid parasitic light penetration and reflection.

Movable mechanical supports

The geometrical and mechanical concepts of the photogoniometer are similar to those of the automated heliodon described in [Rhy91] [Sca94]. It has two main movable axes, corresponding to the two degrees of freedom of the incident light beam (angles θ_1 and ϕ_1).

The first axis allows an inclination from 0° to 90° relative to the horizontal direction of the plane that contains the sample, which corresponds to the variations of angle θ_1 (see Fig. 3.2). The second allows a 360° rotation of the sample support which corresponds to angle ϕ_1.

Both axes are motorised (DC power motors); the first one uses an accurate and reliable gear technology (harmonic drives) to achieve precise movements and maximal torque. A PC computer (IBM-compatible) drives the two motors with Creonics motion control cards.

The mechanical support of the photogoniometer is made of carbon fibres to achieve maximal strength at minimal momentum of inertia. A light proof cache, made with the same material, is fixed underneath the moving plate of the device. It contains the light detection equipment which senses the transmitted light flux though the sample, and protects the detection equipment against parasitic light reflections.

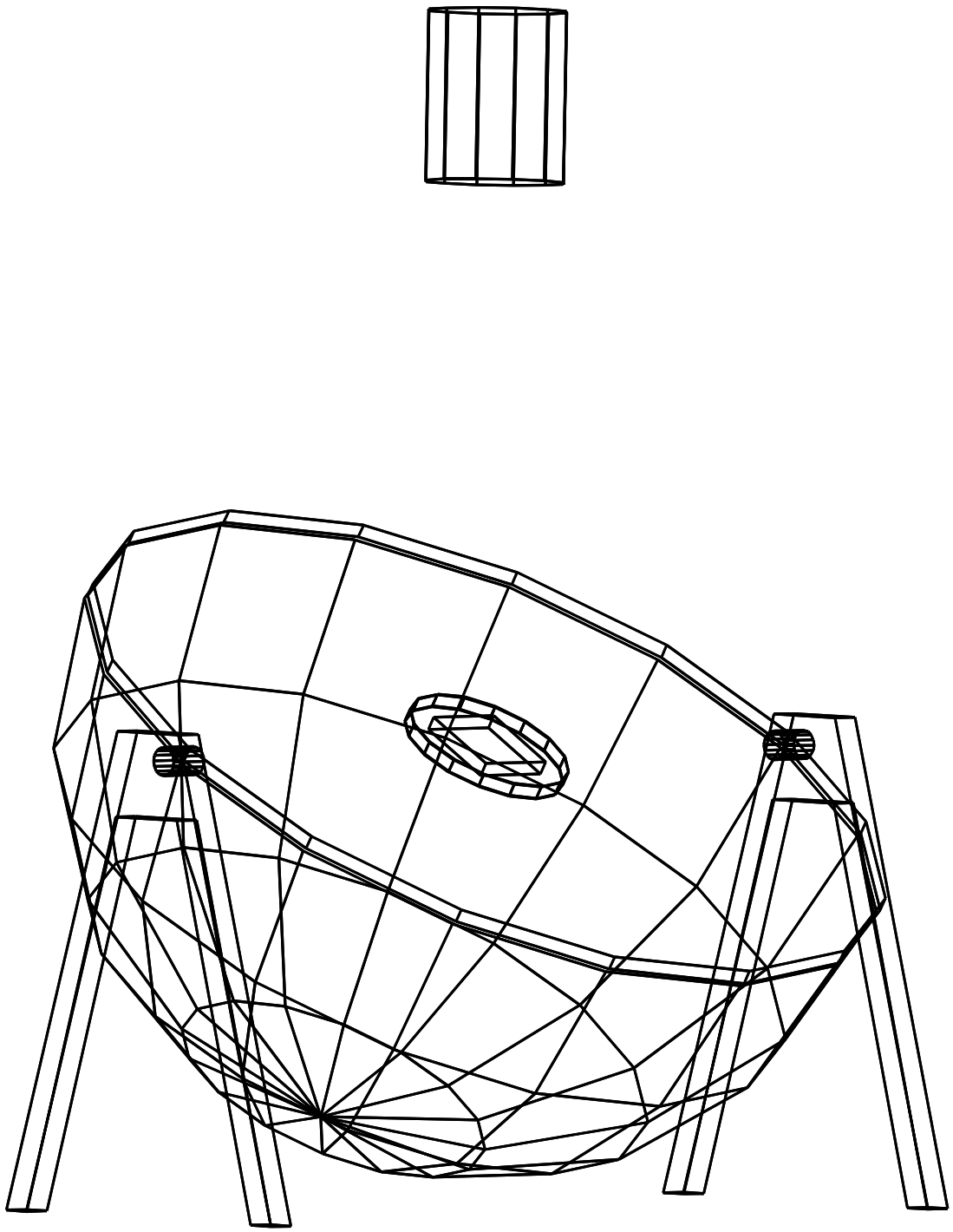

Fig. 3.2. Schematic computer representation of the photogoniometer. The support moves in response to different incident light directions.

The mechanical support is painted in black to reduce interreflections. It is equipped with different safety sensors to avoid damage due to inappropriate movements. Different sample sizes can be handled, thanks to special clipping frames to be fixed on the moving plate. The maximum sample size is 40 x 40 cm^2. Diaphragms of different circular

aperture sizes (from 100 mm to 200 mm) can be used to reduce the sample area sensed by the light detection device. In case of rather homogenous optical materials with small-scale physical structures (clear and opalescent glass, etc.), small diameter diaphragms can be used; in case of materials with larger physical structures (solar blinds, louvers, etc.), larger diaphragms must be chosen. This principle applies to any kind of photogoniometric equipment, whatever the measurements.

Luminance detection techniques

Detection of light flux transmitted through the fenestration sample is made underneath the moving plate of the photogoniometer through digital video equipment. A high definition miniaturised CCD video camera (Kappa CF 8/1 DXCair, 752 x 582 pixels) is used, however, instead of movable illuminance sensors.

The CCD camera is computer controlled through a DC computer (Intel Pentium II 300 MHz) and appropriate digital images acquisition and handling software (IMAGE-PRO PLUS®, Media Cybernetics, LP.). It offers integration intervals comprised between 10 μs and several hours; the lowest integration time interval used for BTDF assessment is 40 ms, to avoid beating effects with the pulsation of the light source (50 Hz AC supply). The CCD camera diaphragm aperture is fixed and set manually. The camera is calibrated on a grey scale in order to be used like a multiple point luminance meter. A detailed description of the CCD camera's functioning principles, characteristics and piloting may be found in [And98]. The optical system used for the photogoniometer is composed of a wide-angle lens (6 mm / 1.2, type H0612FI) fixed on a C-mount. The focal length can not be varied, but the diaphragm aperture can be set manually.

The camera is tightened to a 360° rotating ring: it aims precisely at a flat, triangular structure made of carbon fibres and is fixed to the same ring, which rotates with the camera (cf. Fig. 3.3). The triangular element is painted in white and used as a "projection screen" for the different contributions of the transmitted light: their reflection can then be sensed by the camera which is aiming at the "screen". A perfectly flat "projection screen" was chosen to avoid parasitic interreflections from one screen point to another. This would not be the case for a "projection hemisphere", which for symmetry reasons might have appeared a more natural alternative to the flat triangular element, but was rejected for that reason.

Thanks to the appropriate shrouds (see Fig. 3.1), the projection screen is fixed at an inclination of θ = arctan $2/\sqrt{3} \approx 49°$ for geometric reasons: through an orthogonal projection, it has to appear like an equilateral triangle (see Fig. 3.5).

The projection screen is covered with diffusing LMT white paint: this paint is made of barium sulphate ($BaSO_4$) as the pigment, and of a water-soluble binder with a mixture of selected black pigment. Its important property is to be spectrally neutral, as illustrated in Fig. 3.4 where its spectral response variation shows a variation of less than 1.5%.

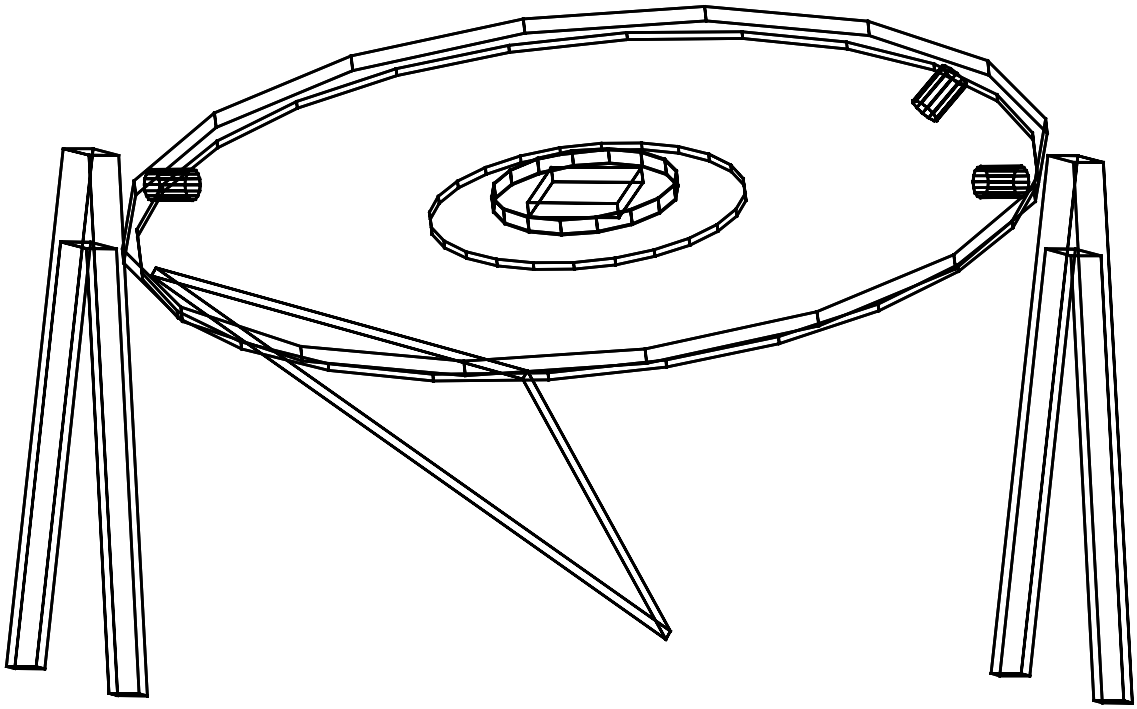

Fig. 3.3. Principle of detection of light transmitted through the sample.

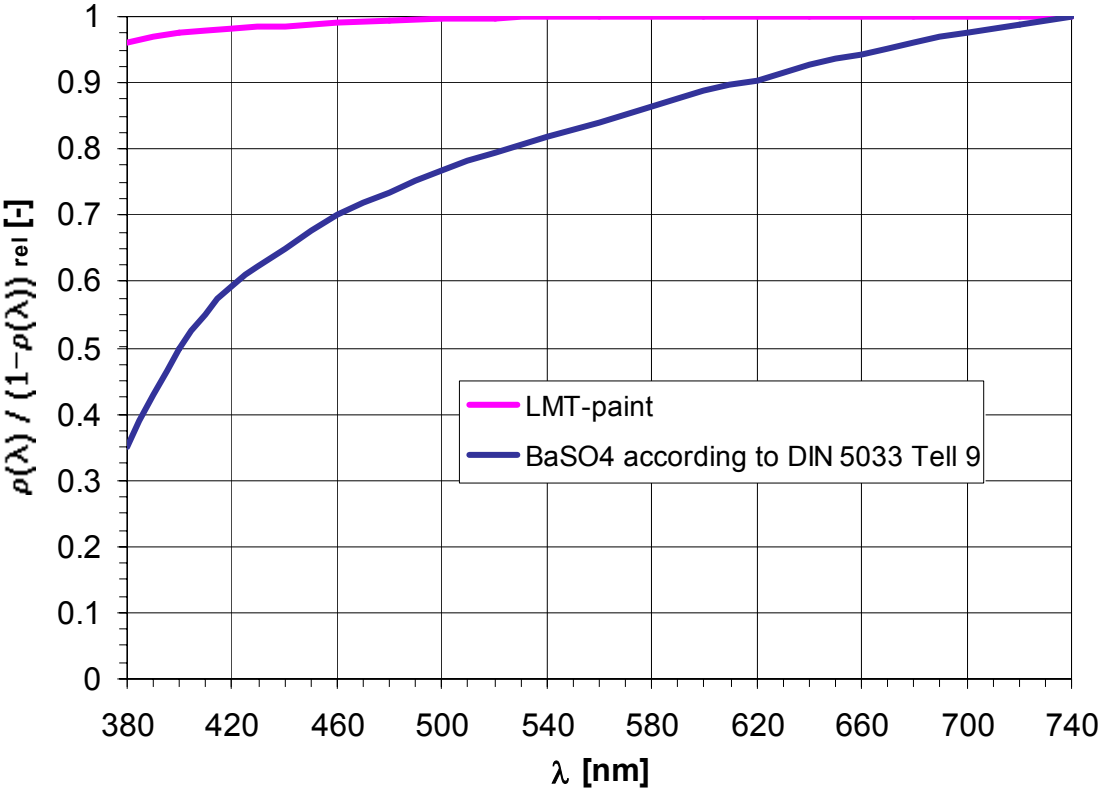

Fig. 3.4. Spectral response of the term $\rho(\lambda)$ / (1-$\rho(\lambda)$) for LMT photometer paint PHP 80 compared to pure $BaSO_4$ powder. $\rho(\lambda)$ is the reflection coefficient value at a given wavelength (source: LMT catalogue)

In order to be used as a multiple points luminance meter, the camera carries out a luminance mapping of the "projection screen". To be able to cover the (2π) steradians solid-angle of all possible outgoing directions, the camera and the screen perform 6 rotations of a 60° angle magnitude each. A third computer-controlled motor, fixed on the moving flat plate of the photogoniometer, drives these movements.

The six screen positions, represented in Fig. 3.5, lead to the visualisation of the whole (2π) steradian hemisphere of the transmitted rays, without any disturbances of measurements due to internal reflections.

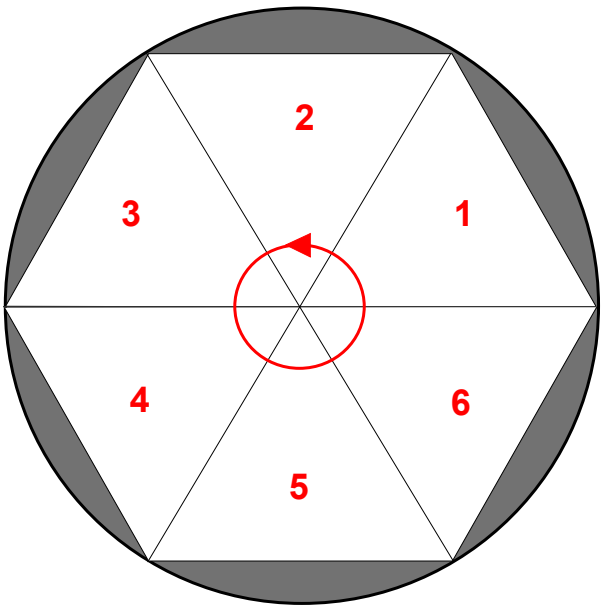

Fig. 3.5. Rotation of main platform and sample holder

The measurement of the illuminance on the sample plane $E_1(\theta_1)$ is performed by an illuminance-meter (LMT, Pocket-Lux 2B), placed on the edge of the sample holder and connected to a data acquisition card (NI-DAQ, PCI 1200) that transmits the information to the computer.

3.2 CALIBRATION PROCEDURES

The CCD camera has to be calibrated in order to be used like a multiple-points luminance-meter. First of all, its spectral sensitivity has to be as close as possible to the human eye sensitivity V(λ), shown in Fig. 3.7. The black and white images must then be converted into luminance maps, thanks to the photometric calibration, by providing integration time dependent relations between grey levels and associated luminances. A geometric calibration will provide the transformation between polar co-ordinates (θ_2, ϕ_2) and pixel co-ordinates (X, Y) on the image. Some additional factors have finally to be examined, like the image uniformity, the diffusion of the screen or the parallelism and homogeneity of the light beam for instance.

3.2.1 Spectral calibration

To spectrally calibrate the CCD camera, two experiments have been carried out, both using the disposal represented in Fig. 3.6: a halogen source is placed in front of the input port of a monochromator, which selects a monochromatic radiation of the colour separated light beam through the output port (resolution = 5nm). The emerging beam is then reflected by an achromatic diffusing screen, presenting a constant reflectivity over the whole visible spectrum, and redirected towards a calibrated detector (spectrophotometer ORIEL Multispec^{TM} 1/8M Spectrograph) and the CCD camera. Both sensors will simultaneously analyse the energetic luminance, the spectrophotometer by providing its value in [mW · m^{-2} · sr] and the camera by giving the pixels' grey levels (0 to 255), the integration time being fixed. A set of measurements is carried out by decreasing the light beam intensity until the detected values become of the same order as their own error. The relation between grey level and associated energetic luminance, independent on the wavelength, is therefore determined.

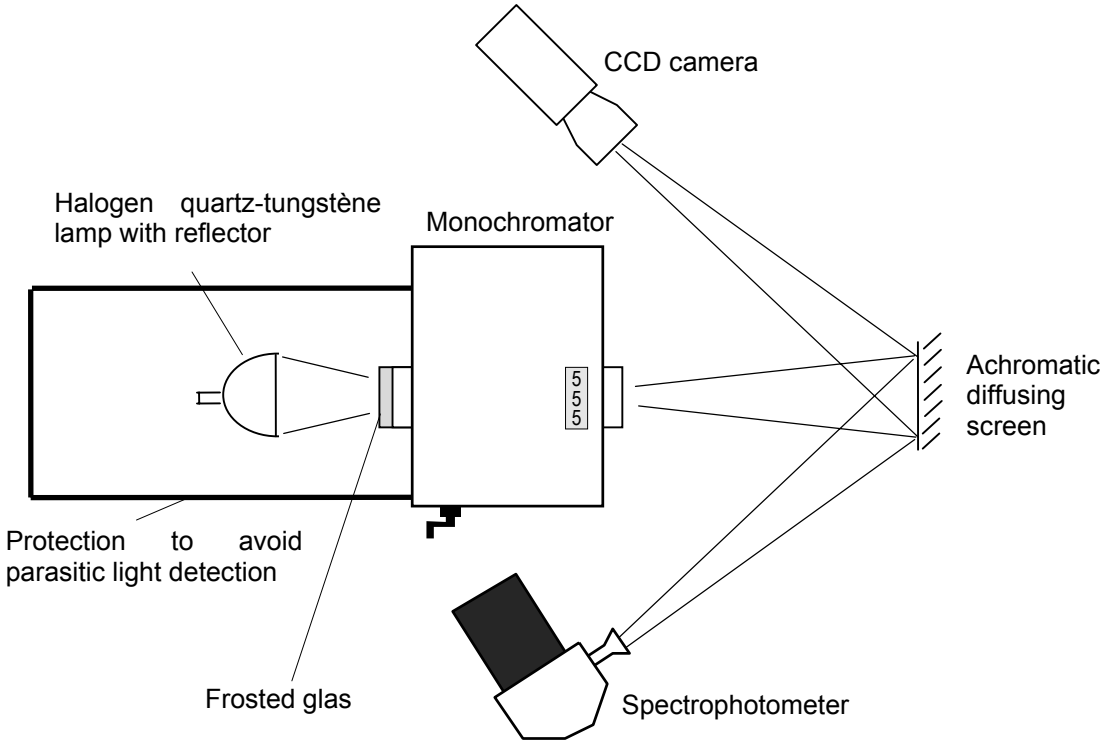

Fig. 3.6. Experimental disposal for spectral calibration

The second experience is quite identical to the first one, except on the point that the wavelength of the emerging radiation is modified, the beam intensity being kept constant. The grey levels obtained are converted into the corresponding energetic luminances, and compared to the values simultaneously measured by the spectrophotometer. Their ratio leads to the spectral sensitivity curve of the CCD camera, shown in Fig. 3.7; this curve is normalised to 1 at 555nm. It is observed that the camera is much too sensitive in the blue and the red parts of the spectrum compared to the human eye; photopic filters are therefore needed in order to minimise these differences.

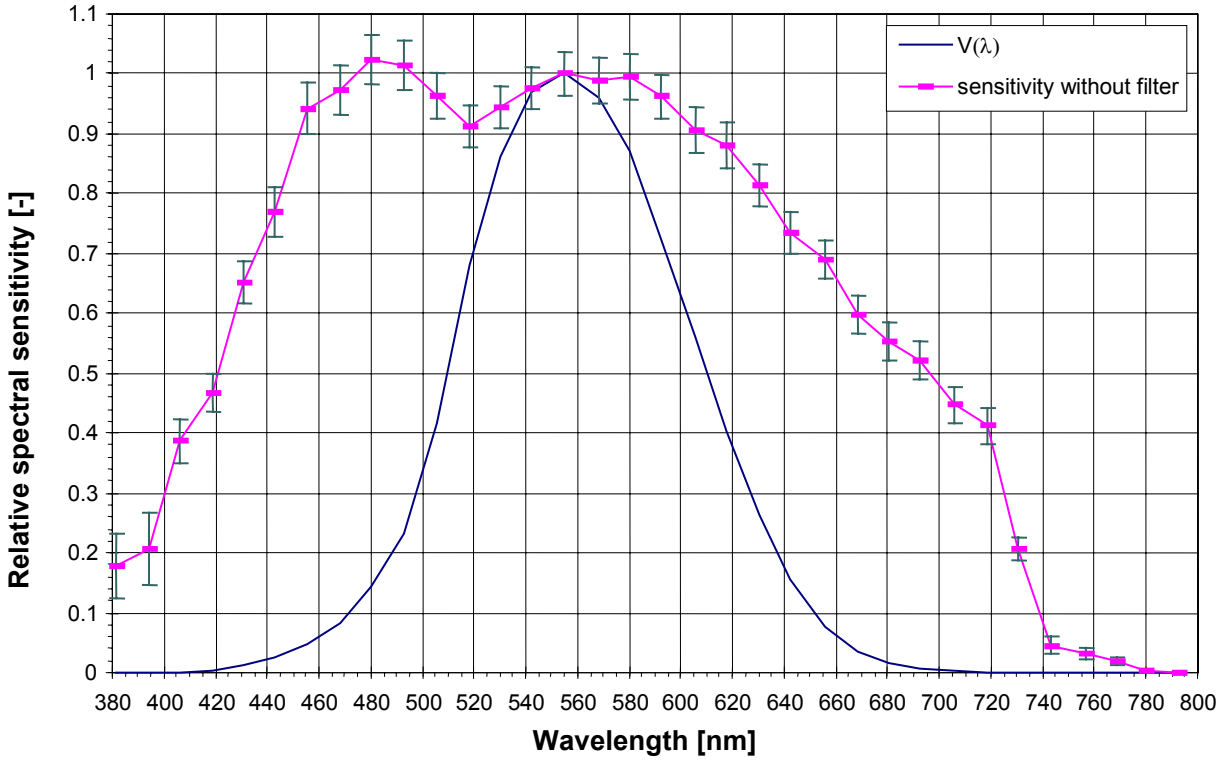

Fig. 3.7. CCD camera relative spectral sensitivity . Comparison with human eye's sensitivity V(λ).

The determination of the type and the optimal thickness of photopic filters, that will correct the spectral sensitivity and render it as close as possible to V(λ) is based on a least-square method [Wri69]: the function to minimise is given by (3-1); details on this procedure may be found in [And98].

$$\sum_{k=1}^{N}\left[\frac{1}{(V(\lambda_k)+0.01)}\cdot\left(V(\lambda_k)-0.92^{\left(N_F-\sum_{n=1}^{N_F}\frac{e_n}{e_{n0}}\right)}\cdot\zeta\cdot S(\lambda_k)\cdot\prod_{n=1}^{N_F}(T_{n0}(\lambda_k))^{e_n/e_{n0}}\right)^2\right] \qquad (3\text{-}1)$$

where

- 0.01 is a term added to minimise the relative error on points of very low sensitivity
- N is the number of measured points (N = 34)
- N_F is the number of filters (N_F =3)
- S(λ) is the relative spectral sensitivity of the camera

- the factor 0.92 takes reflection effects into account, inducing a loss of transmitted light through optical filters
- T_{n0} is the transmission of filter n at thickness e_{n0}
- e_n and e_{n0} are, respectively, the thickness of filter n for optimal correction and the thickness at which its transmission T_{n0} has been measured
- ζ is a scale factor to normalise the second term, expressed by (3-2):

$$\zeta = \frac{1}{\max_{k=1}^{N} \left[0.92^{\left(N_F - \sum_{n=1}^{N_F} \frac{e_n}{e_{n0}} \right)} \cdot S(\lambda_k) \cdot \prod_{n=1}^{N_F} (T_{n0}(\lambda_k))^{e_n / e_{n0}} \right]} \qquad (3\text{-}2)$$

The variables to determine are therefore the e_n values. The choice of optical filters adapted to our purpose is based on photopic filters catalogues and on reference [Ber96]; the selected filters are Kopp n°3384, Kopp n°3307 and Schott BG39. The right thickness' are calculated with the MICROSOFT EXCEL® Solver, accounting for the following limits:

- $\Sigma e_n \leq 8$mm (in order to install them easily on the camera's objective)
- $e_n \geq 0 \ \forall n$.

The results are : 0.47mm for the Kopp n°3384, 3.09mm for the Kopp n°3307, 1.20mm for the Schott BG39; the corresponding predicted transmissions and their combination is shown in Fig. 3.8.

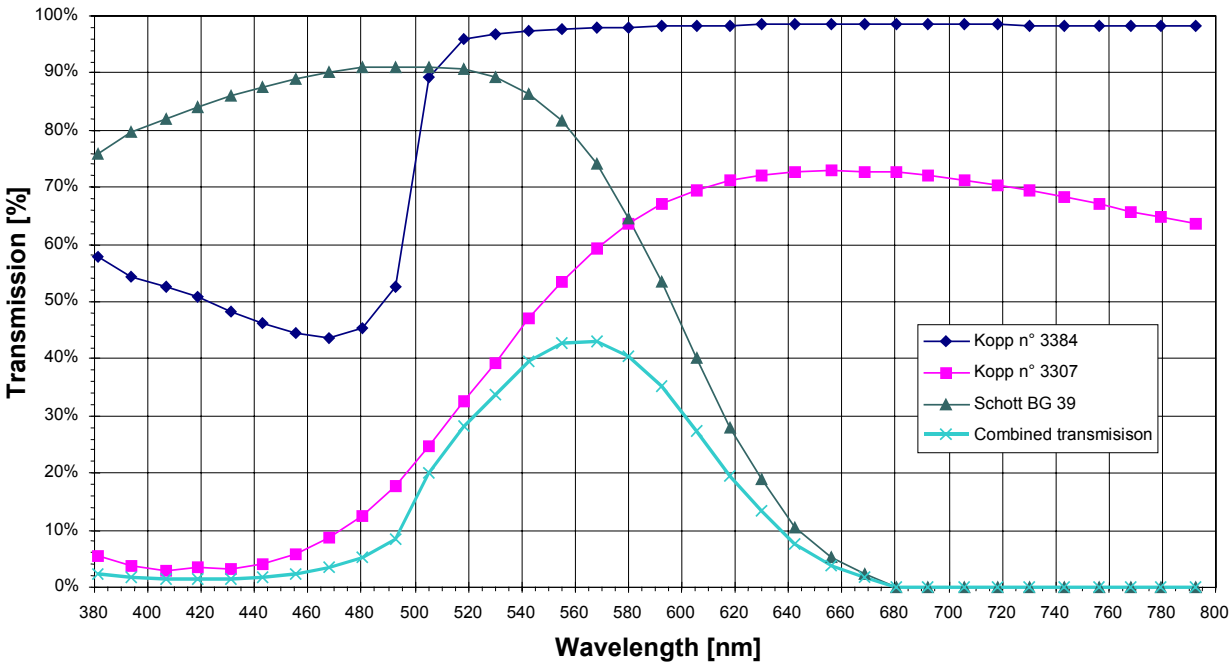

Fig. 3.8. Mathematically predicted filter transmission curves, at calculated optimal thicknesses.

The corrected spectral sensitivity may thus be predicted too, by calculating the new values of $\zeta \cdot S(\lambda_k) \cdot T_{glob}(\lambda_k)$ for each λ_k. The corresponding curve is shown in Fig. 3.9 and compared to $V(\lambda)$; as they very well fit together, the filters were cut at the calculated thickness and then placed in front of the camera's objective.
The measured sensitivity is represented in Fig. 3.9 too: the curve is quite similar to the one based on a mathematical prediction, except for wavelengths from 420nm to 500nm,

where the Kopp n°3384 filter seems to have a particular behaviour when it is very thinly cut. Anyway, the correspondence between V(λ) and the corrected sensitivity experimentally determined remains of good quality: it induces a relative error f'_1, indicating the degree to which the corrected sensitivity matches V(λ) [CIE87], of about 10%. As explained in § 3.3.4, this incertitude has not an important effect on the measurements quality.

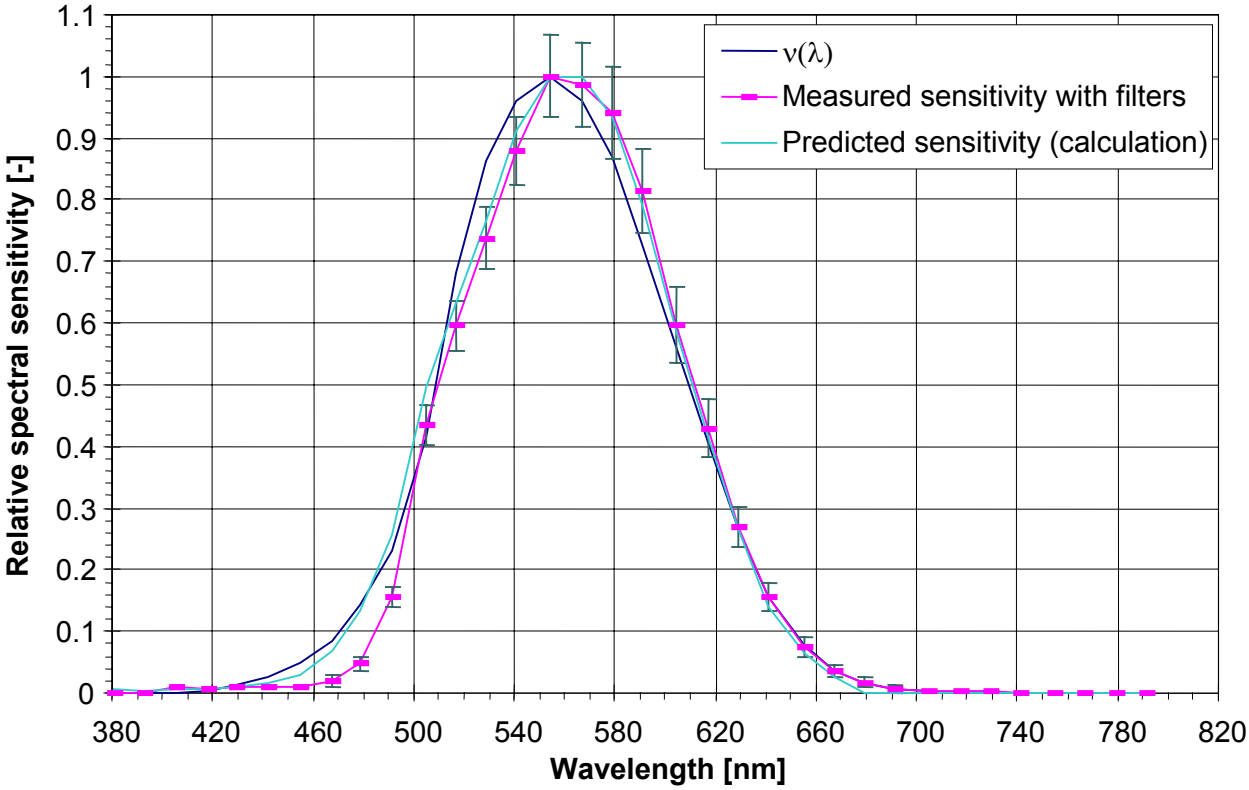

Fig. 3.9. Relative spectral sensitivity of the CCD camera: measured and calculated corrected curve, compared to V(λ).

3.2.2 Photometric calibration

The photometric calibration determines the relations between picture grey levels and corresponding luminance values, which depend on the CCD camera integration time. These conversions shall be applied on the camera exposures, in order to produce floating-point images composed of luminance-calibrated pixels.

The experiment to be carried out is illustrated in Fig. 3.10: simultaneous measurements of a diffusing white screen illuminated by a 500 Watts halogen lamp are performed with the CCD camera on one side, and a calibrated luminance-meter on the other side, by placing the source at different distances from the screen.

All integration times that are used for sample characterisations (i.e. 40 msec to 2.56 sec) must be analysed and calibrated. The lowest one is chosen to be 40ms, in order to avoid beating effects with the light source's own pulsations (50 Hz AC supply). The diaphragm aperture is manually fixed to an opening inducing no pixel saturation at 40ms when the measured luminance is of about 850 Cd/m^2, which is the value obtained after reflection on the lambertian triangular screen by the light source (see § 3.1.2). During photometric

calibration, the light source is thus taken back from the screen step by step, starting at this maximal luminance, and decreased until the pixels become under-exposed at the highest integration time (2.56 sec in our case). This extreme value allows a resolution of high quality for low luminance values and keeping a reasonable exposure time.
The grey level to luminance conversion is illustrated by Fig. 3.11 for the different used integration intervals. The non-linear property of the response curves is deliberately chosen to achieve a good resolution for low luminance levels: a linear relation could not offer large enough grey level dynamics for small luminance differences in dark regions.

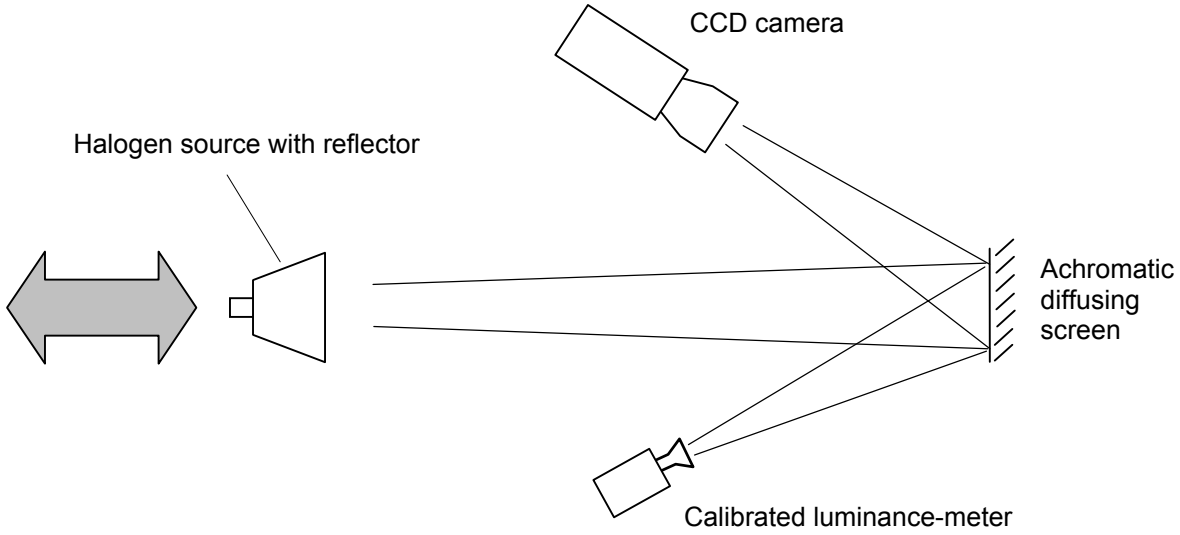

Fig. 3.10. Experimental disposal for photometric calibration.

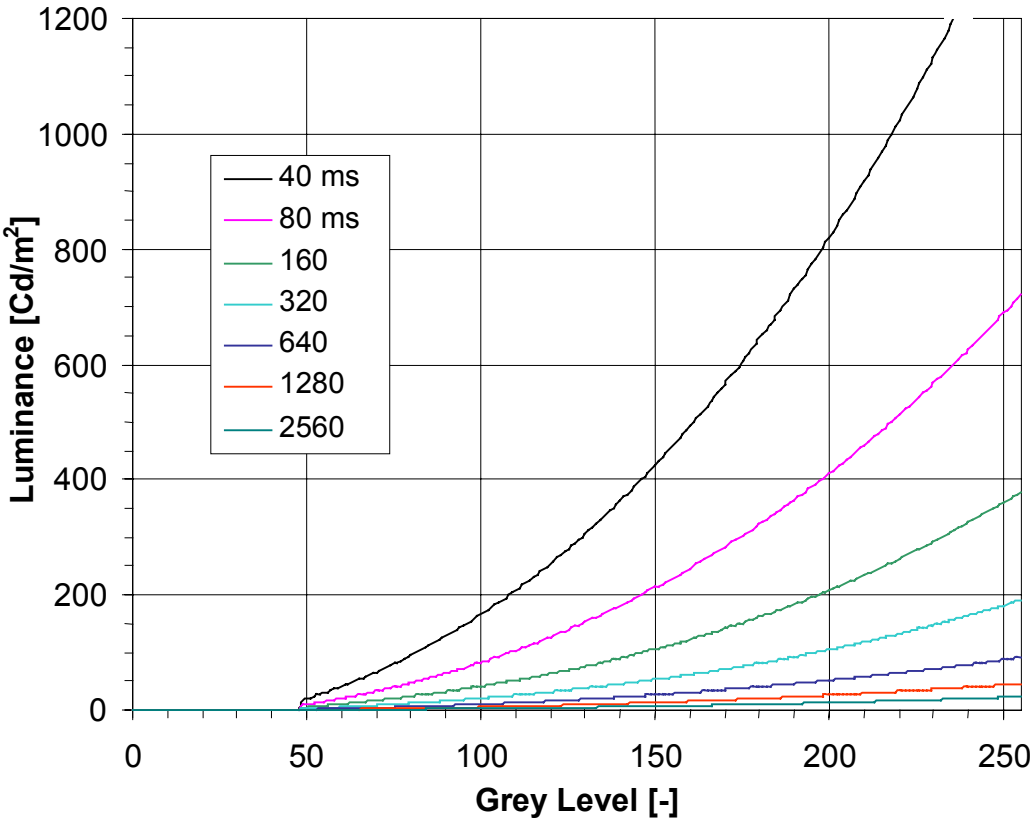

Fig. 3.11. Photometric calibration curve for the different used integration times. The relative measurement errors remain in general lower than 1%.

3.2.3 Geometric calibration

The aims of the geometric calibration are to determine the relationship between the spherical co-ordinates (θ_2, ϕ_2) and the pixel co-ordinates (X, Y) on the image plane. This relation can be divided into three conversions:

- first the correspondence between the spherical co-ordinates (θ_2, ϕ_2), defined for the whole hemisphere, and the polar co-ordinates (θ_2, ψ_2), defined for each screen position (see Fig. 3.12). The polar angle ψ_2 is comprised between –30° and +30° and determines the azimuth value of a particular point for a given screen position. It is null on the central axis of the screen.

- then a transformation from polar co-ordinates (θ_2, ψ_2) into planar co-ordinates (i,j), illustrated by Fig. 3.12, determining a point on the triangular screen.

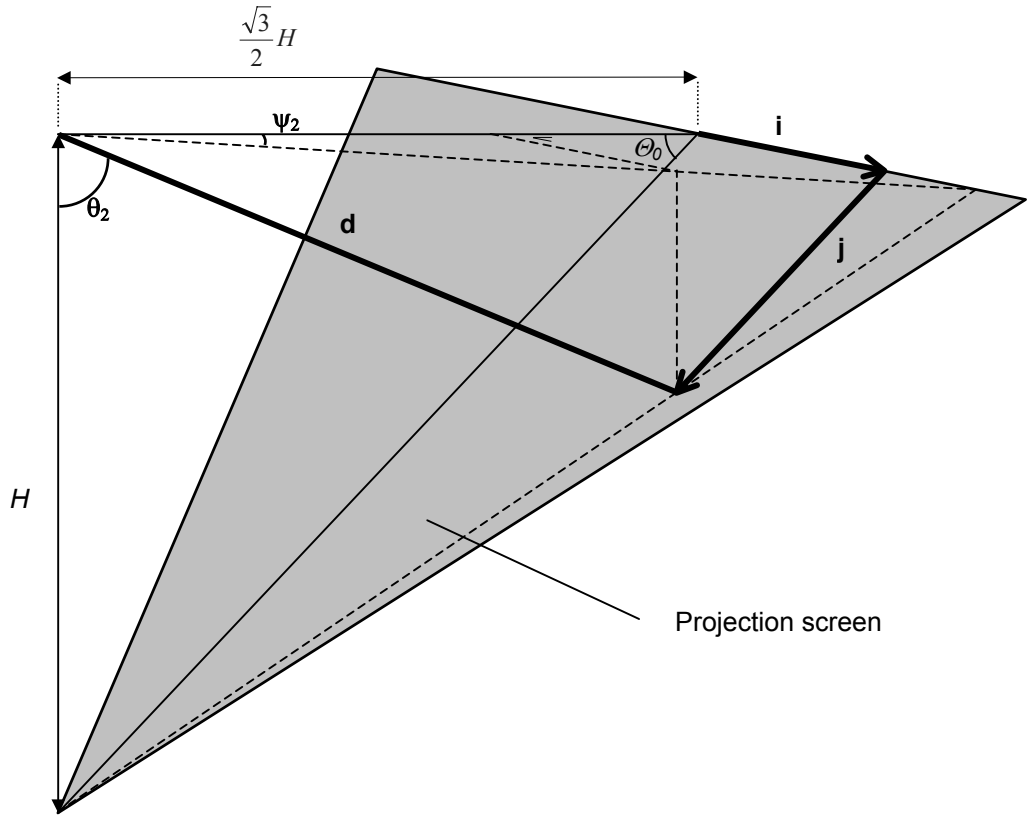

Fig. 3.12. Relation between polar co-ordinates (θ_2, ψ_2) and associated cartesian screen co-ordinates (i,j).

- finally the association between the position on the screen given by (i, j) and the location of the associated image pixel, determined by co-ordinates (X, Y). This second conversion cannot be only geometrically established, as image distortions may appear. In order to take this effect into account, the relation is based on locating points of given polar co-ordinates directly on the image, as explained below.

The first conversion is a simple transformation from global azimuth ϕ_2 into screen azimuth ψ_2, only depending on the screen position concerned.

The second conversion is given by equations (3-3), asking for three dimensional trigonometric considerations:

$$d\sin\theta_2 = \frac{\frac{\sqrt{3}}{2}H - j\cos\Theta_0}{\cos\psi_2} \qquad d\cos\theta_2 = j\sin\Theta_0 \quad \rightarrow \quad d\sin\theta_2 = \frac{\frac{\sqrt{3}}{2}H - d\frac{\cos\theta_2}{\tan\Theta_0}}{\cos\psi_2}$$

which leads to

$$d = \frac{\sqrt{3}\cdot H}{2\cdot\left(\sin\theta_2\cdot\cos\psi_2 + \frac{\sqrt{3}}{2}\cos\theta_2\right)} \qquad i = d\cdot\sin\theta_2\cdot\sin\psi_2 \qquad j = d\frac{\cos\theta_2}{\sin\Theta_0} \qquad (3\text{-}3)$$

where

- d is the distance from the sample centre to the screen, along direction (θ_2,ψ_2) (or (θ_2,ϕ_2)) [m]
- H is the vertical distance from the screen apex to the base plane (H = 1.15) [m]
- Θ_0 is the angle between the screen plane and the main platform [°] (Θ_0 = atan $2/\sqrt{3} \cong$ 49.1°); it has been chosen so that an orthogonal projection of the screen leads to an equilateral triangle (cf. Fig. 3.4)
- (i, j) are the cartesian screen co-ordinates [m].

Based on equations (3-3), a grid composed of lines of different altitude angles θ_{2n} and azimuth angles ψ_{2n} is drawn on a screen and exposed to the camera. The screen has the same thickness and dimensions as the diffusing triangular panel installed in the photogoniometer.

Fig. 3.13 shows the map screen defining 901 different points at the line intersections for angular resolutions of 2.5° in both directions. The same type of grid is used to define the angular resolution on the “transmission hemisphere” of the outgoing directions of light rays: angular resolutions of 10° for altitude angle and 15° for azimuth are shown as an example in Fig. 3.14.

This procedure takes into account image distortions due to possible imperfections of the camera lenses, without adding a supplementary geometrical correction factor.

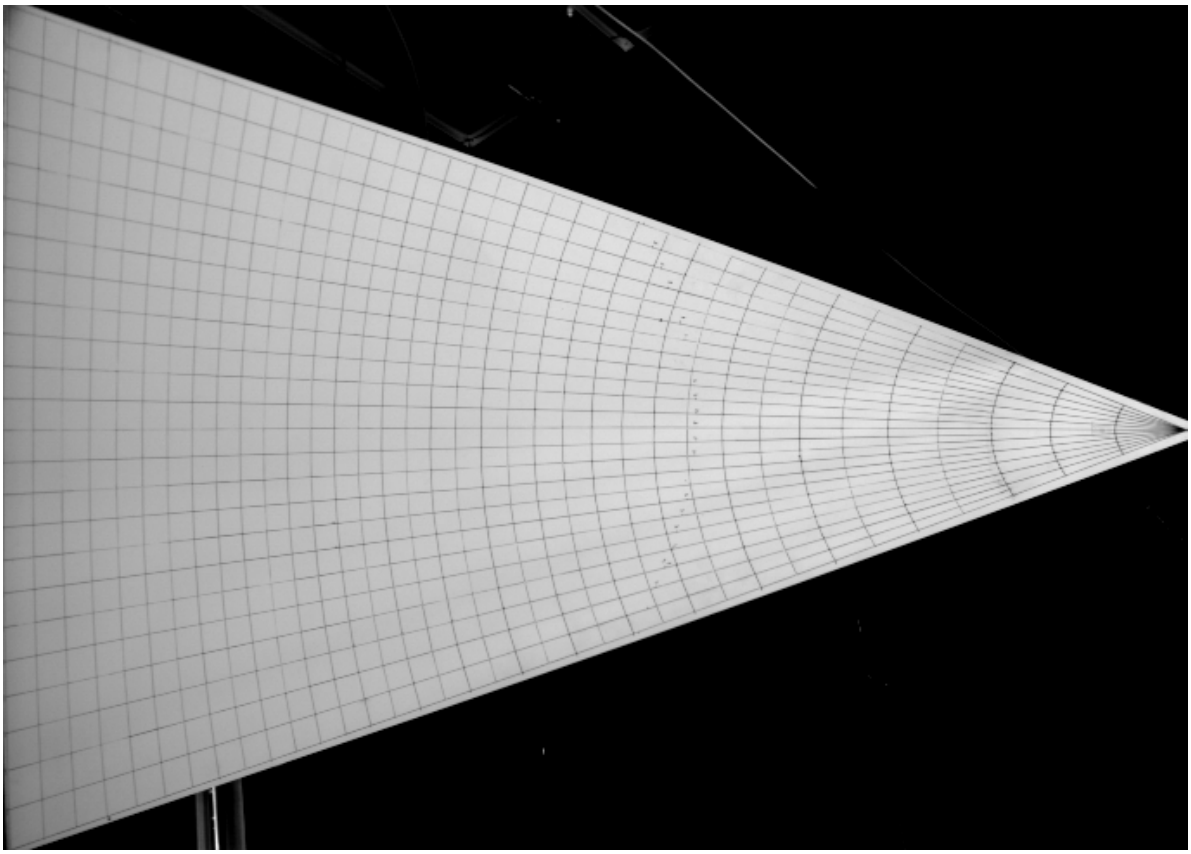

Fig. 3.13. Support grid with 2.5° of angular resolution for geometric calibration.

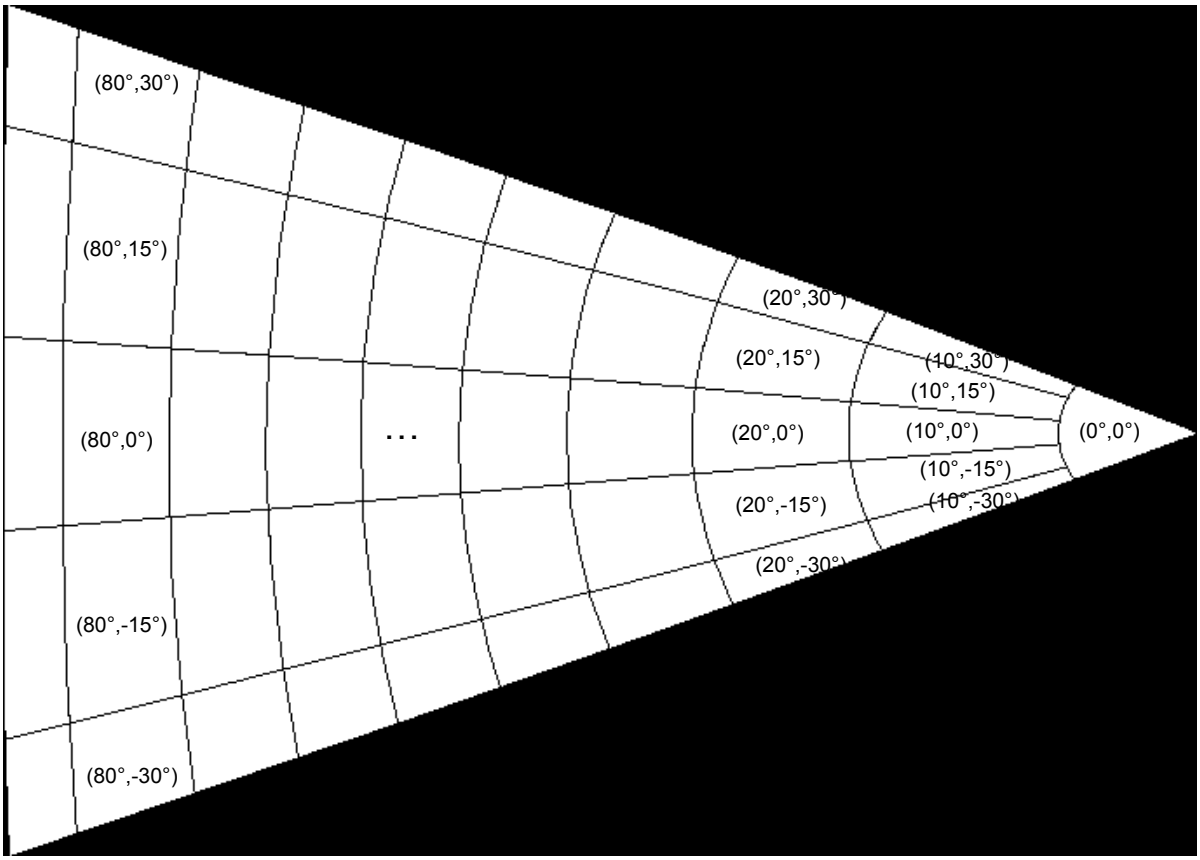

Fig. 3.14. Outgoing directions grid for $(\Delta\theta_2, \Delta\phi_2)$=(10°,15°).

3.2.4 Additional corrections

Image Uniformity

The image uniformity is checked to ensure that luminance measurements of different points on the CCD camera field are independent from their position on the latter. A stable luminous configuration, characterised by a constant luminance, is filmed through the CCD camera at different relative positions on the image field.
The averaged values of different positions, obtained after calibration, are shown in Fig. 3.15: luminance relative differences of 3% are observed when approaching the triangle edges, with a relative darkening of 10% for the triangle apex. A software correction, explained below, is applied to correct these small effects.

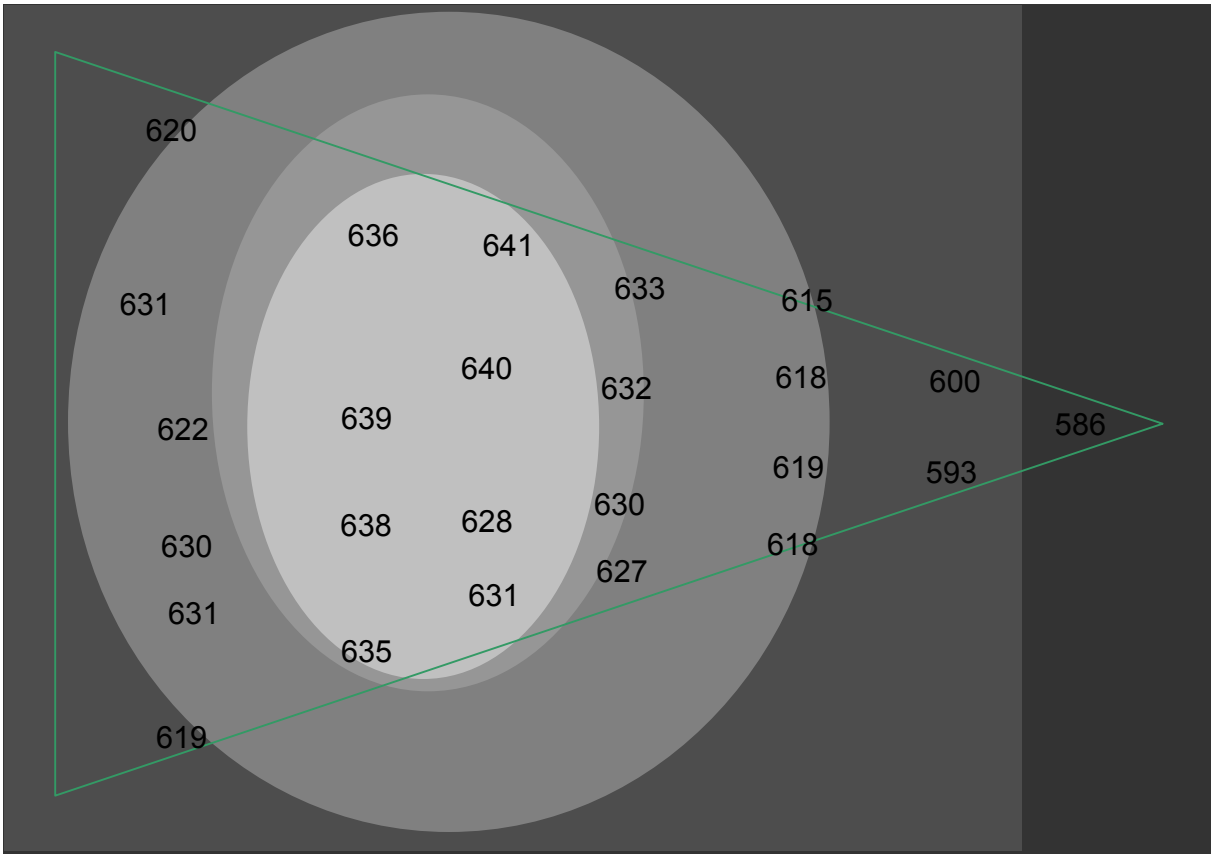

Fig. 3.15. Control of image uniformity. The given values are luminances [cd/m^2], deduced from calibrated grey level images.

Screen diffusion quality

The characteristics of diffusion of the triangular screen, together with the uniformity of the reflection coefficient, have been measured with two experimental set-ups.
A Minolta CR-200b surface chromameter, evaluating the reflected proportion of a luminous flux provided by a flash on a diffusing surface, was used to measure the reflection coefficient ρ of different points over the whole screen, showing a mean value for ρ of 0.743, with relative fluctuations lower than 0.7%.

Luminance values measured at different emerging angular directions from the triangular panel, and under several incident angles β_k, were used to assess the diffusion characteristics of the LMT white paint: a Lambertian diffusion was ideally expected to be observed. Fig. 3.16 shows the measured luminance distribution, which fits a Lambertian model curve within a 10% relative range; this minor imperfection in diffusion is corrected as detailed below.

The grazing incidence (i.e. large value of angle β_k) leads, however, to poorer results, as illustrated in Fig. 3.17, showing a significant component of specular reflection: this does however not have a serious impact on the photogoniometer's performances, as incidence angles on the triangular projection panel are lower than 50° in any case (by the way of geometrical position of the sample, see Fig. 3.12).

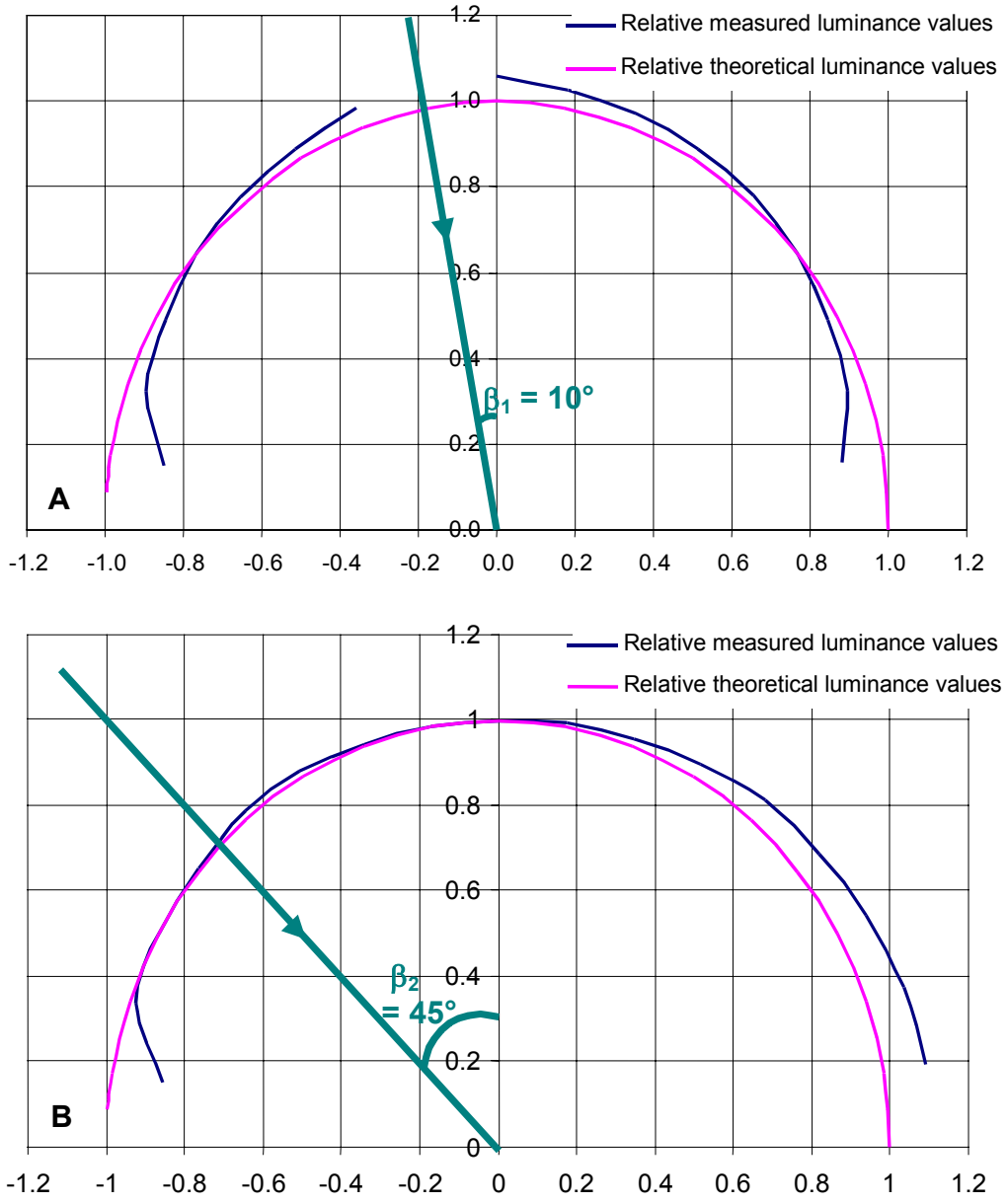

Fig. 3.16. Measured luminance distribution after reflection on LMT photometer paint, for different incident directions: **A** β_1 = 10° **B** β_2 = 45°. The theoretical values are deduced from the lambertian model (ideal diffusion).

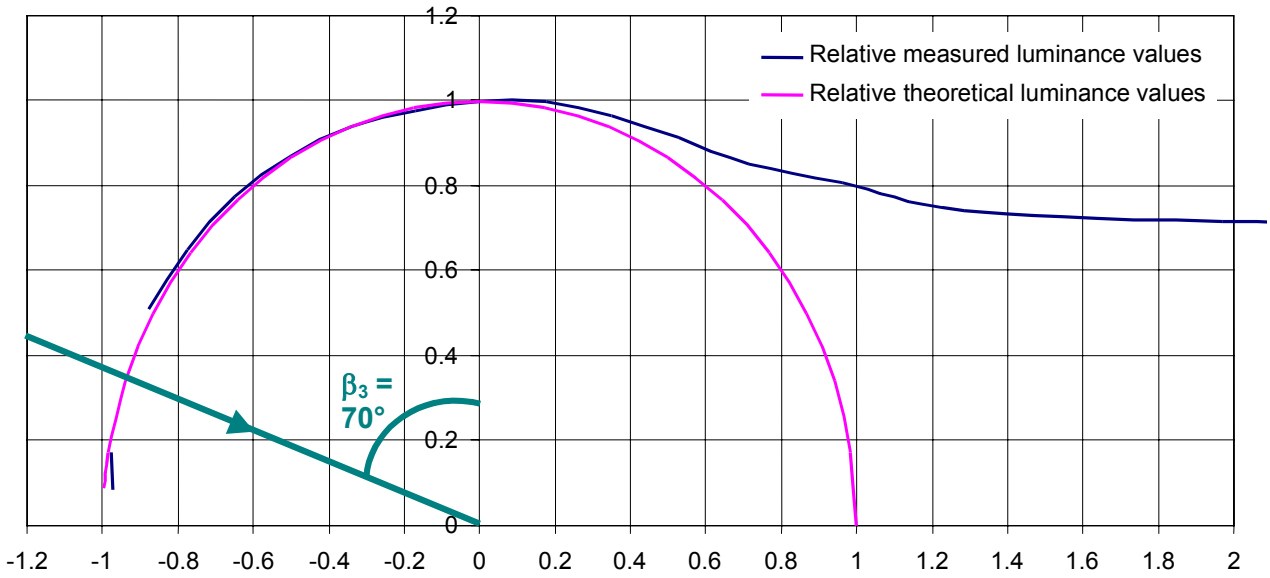

Fig. 3.17. Specular effect for grazing incidence (β_3 = 70°) on LMT photometer paint.

Correction of image non-uniformity and imperfect diffusion of screen

As the camera and the sample remain within the same relative positions and directions with regard to the screen, the sample thickness being neglected, the effects of image non-uniformity and non-perfect diffusion remain constant on the final treated image: both effects can therefore be corrected through the same procedure.
For this purpose, screen snapshots are taken for two kinds of situations:

- with a lambertian diffuser (plexiglas sample), showing a rotational symmetry, placed on the aperture (Fig. 3.18A)
- with no sample on the aperture, the light beam reaching the triangular panel without any perturbation (Fig. 3.18B).

The first configuration is used to determine groups of pixels of expected equal luminance, taking distance and light tilting effects into account (the analytical correction to apply is explained in § 3.3.3): these groups of pixels are characterised by equal θ_2 values, as shown in Fig. 3.18A (white dots forming circular lines).

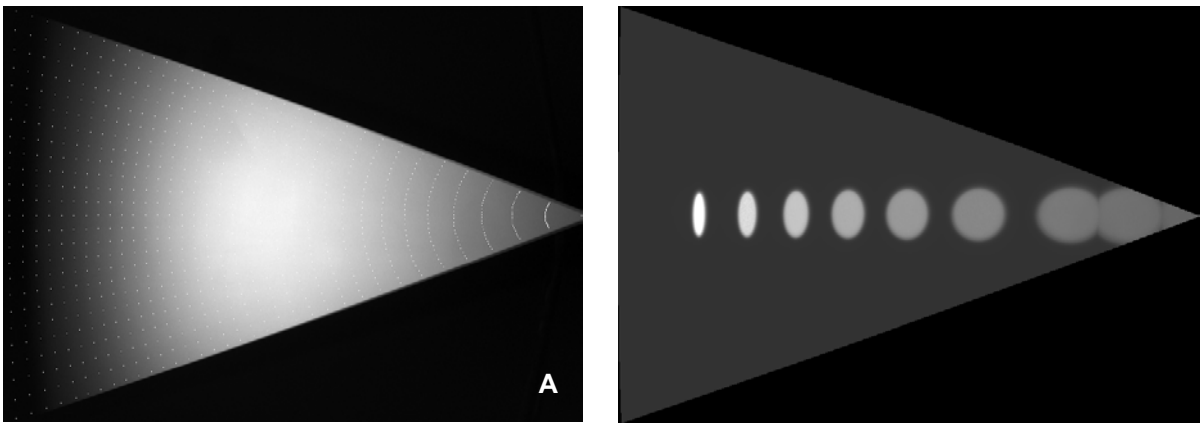

Fig. 3.18. **A** Plexiglas sample. Points of equal altitude θ_2 are expected to be of equal luminance values, once their distance and light tilting effects have been compensated. **B** Superposition of images obtained without sample (hole). The centre pixels inside each illuminated zone are expected to have values deduced from equation (3-4).

The values of the pixels belonging to the central axis of the screen, along which the ellipses of Fig. 3.18B are placed, are considered as a reference for each group; correction factors are thus determined by comparison for the other pixels inside the groups, and then interpolated in-between.

The second configuration can be used to assess the expected screen luminance given by equation (3-4), obtained assuming a perfectly diffusing surface (see Fig. 3.19). Practically, the images are divided by the simultaneously measured illuminance on sample plane E_P in order to avoid any light source fluctuation effects. Once they have been calibrated, the images are thus made of pixels representing values of $L_{P'}/E_P$ ratios.

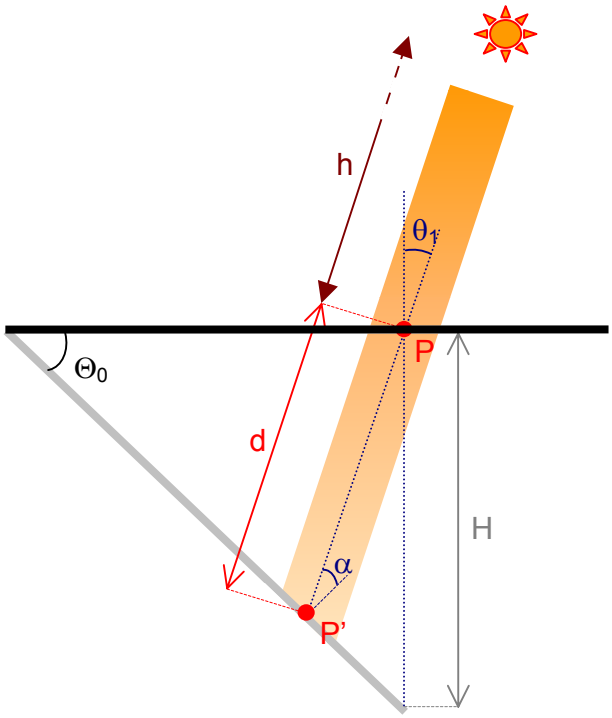

Fig. 3.19. Geometric characteristics of an incident beam reaching the screen without any sample.

$$E_P = \frac{I_0 \cos(\theta_1)}{h^2} \qquad E_{P'} = \frac{I_0 \cos\alpha}{(h+d)^2} = \frac{\pi L_{P'}}{\rho} \quad \rightarrow \quad \frac{L_{P'}}{E_P} = \frac{\rho E_{P'}}{\pi E_P} = \frac{\rho h^2 \cos\alpha}{\pi (h+d)^2 \cos\theta_1} \qquad (3\text{-}4)$$

where

- I_0 is the light source intensity in the direction of point P [cd]
- h is the distance from the sample to the light source [m]
- E_P is the illuminance of the sample plane at point P [lx]
- $E_{P'}$ is the illuminance of the triangular screen at point P' [lx]
- $L_{P'}$ is the luminance of the reflected light flux at point P' [cd · m^{-2}]
- ρ is the reflection factor of the triangular screen [-]
- α is the angle between the normal to the screen and the direction (θ_2,ϕ_2) [°].

The theoretical values expected along the central screen axis may be compared to the ones obtained for the calibrated "hole" images (Fig. 3.18B), measured at the center of the "hole" projections (ellipses) ; a correction curve for the central axis can be deduced: it is represented in Fig. 3.20.

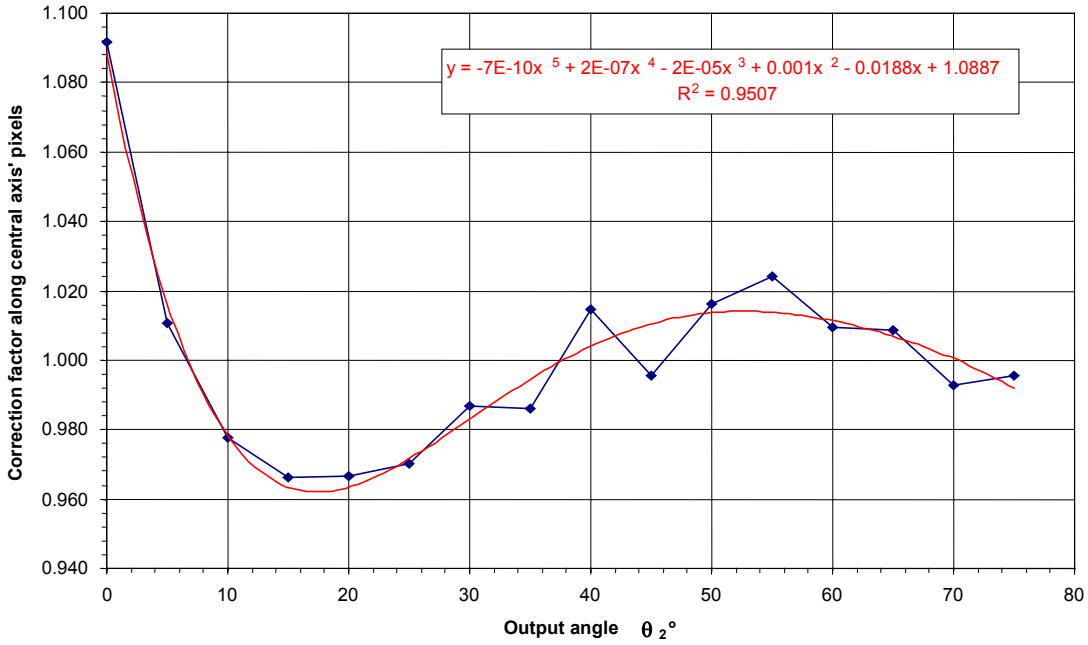

Fig. 3.20. Correction factor evolution along central screen axis' pixels; the curve fitted to these correction factors for different θ_2 angles is shown and expressed by a polynomial of the fifth degree.

The correction is then extended to all other pixels, by multiplying the results of both configurations : the factors obtained are represented in Fig. 3.21 by grey levels.
During its processing, each final image is thus multiplied by this correction figure to compensate non-uniformity and imperfect diffusion of the triangular screen.

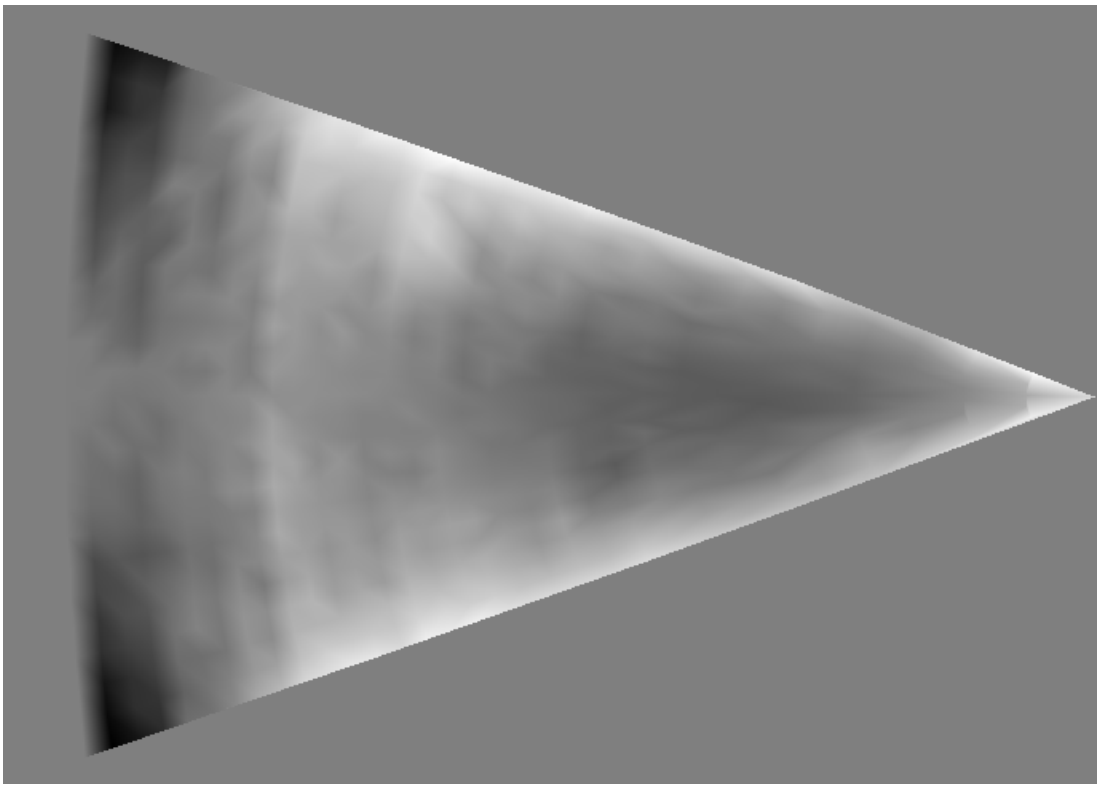

Fig. 3.21. Correction figure for image non-uniformity and imperfect diffusion of triangular screen. Grey levels are to be associated with correction factor values: 0.88 (black) to 1.13 (white) ; the image region outside the measured area (screen) is arbitrarily fixed to 1.

Incident beam properties

The light beam uniformity over the 40x40cm^2 sample area has to be checked. For that purpose, an illuminance meter is moved over the concerned region and the illuminances are measured, taking the light source fluctuations into account by pondering the results by another simultaneously measuring fixed illuminance sensor.
The uniformity of the illuminance reaches an average value of 3700 lux, with a mean relative deviation of only 1.8%. The great distance from the source to the sample, relative to its size and cross section, reduces further the effect of inverse-square law (Bouguer law) on the sample illuminance: the maximum relative deviation reaches 3.7% for a movement from horizontal to fully vertical. This result reveals a good quality in the sample's illuminating homogeneity.

Another analysis concernd the collimation of the incident beam, a significant divergence causing an error in the area factor (see § 3.3.3). An experimental procedure was therefore carried out to estimate the possible angular spread of the beam, by comparing the measured and the theoretical diameter of a zone defined by the light beam on the triangular screen, after passing through the aperture of the photogoniometer (sample position)
The theoretical diameter D_p is calculated geometrically by considering a hole of diameter D at the sample position and a perfectly collimated beam (parallel rays), showing no scattering nor divergence, as illustrated in Fig. 3.22. Its expression is given by equation (3-5).

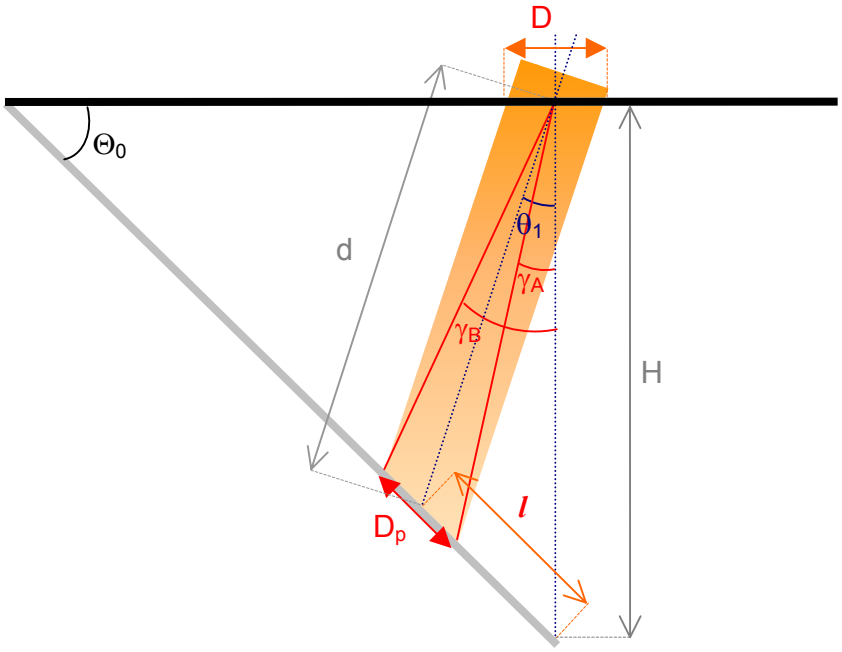

Fig. 3.22. Geometric characteristics of parallel beam incident on triangular screen.

$$D_p = \frac{D\cos\theta_1}{\cos(\theta_1 - \Theta_0)} \qquad (3\text{-}5)$$

In order to have a link between this theoretical segment D_p and the number of corresponding pixels that should be bright on the image if the beam was perfectly

collimated, the relations between the projected diameter extremities and the polar angles γ_A and γ_B associated (see Fig. 3.22) have to be determined: they are given by equations (3-6).

$$\gamma_A = \arctan \frac{\left(\frac{H \sin\theta_1}{\cos(\Theta_0 - \theta)} - \frac{D \cos\theta_1}{2\cos(\theta_1 - \Theta_0)} \right) \cos\Theta_0}{H - (l - \frac{D_p}{2}) \sin\Theta_0}$$

$$\gamma_B = \arctan \frac{\left(\frac{H \sin\theta_1}{\cos(\Theta_0 - \theta)} + \frac{D \cos\theta_1}{2\cos(\theta_1 - \Theta_0)} \right) \cos\Theta_0}{H - (l + \frac{D_p}{2}) \sin\Theta_0} \qquad (3\text{-}6)$$

The geometric calibration is then used to deduce the pixel X co-ordinates corresponding to these angles, and the theoretical value of D_p may thus be found in pixels, illustrated by the step curve in Fig. 3.23. The experimentally obtained value D'_p is determined by applying a line contour on the image (see Fig. 3.23) and integrating the corresponding values.

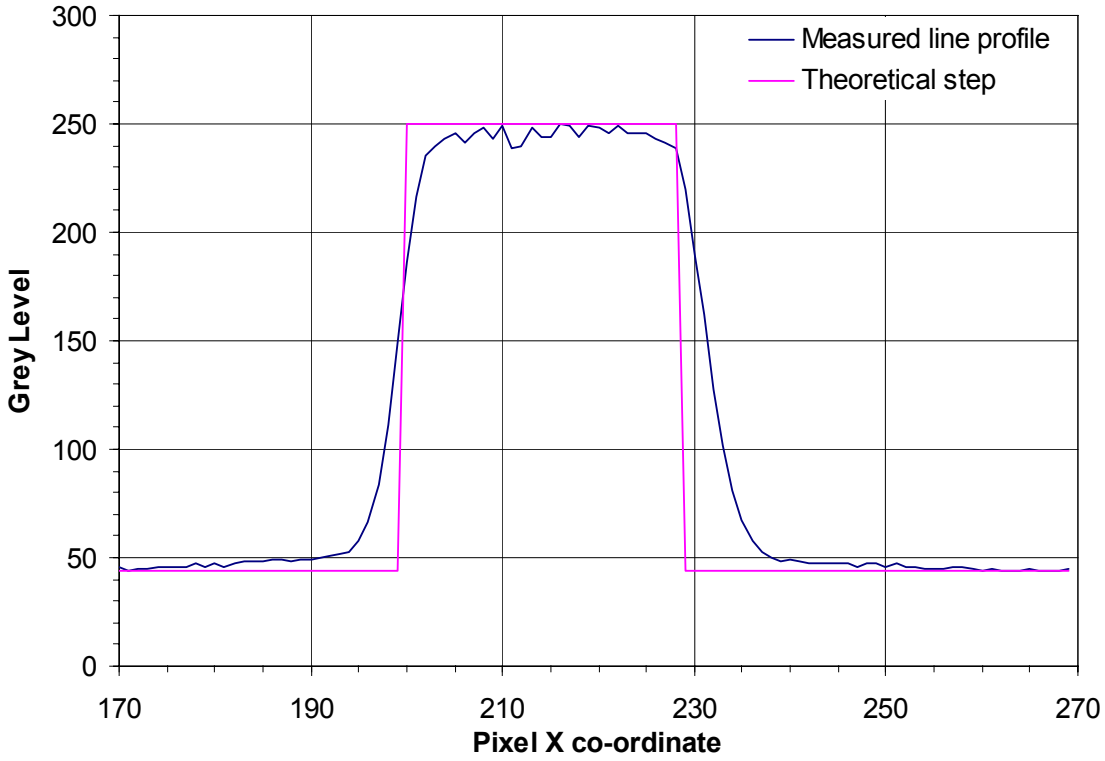

Fig. 3.23. Illuminated zone (profile) compared to the theoretical step corresponding to a perfectly collimated beam model, for an incidence normal to the screen surface ($\theta_1 = \Theta_0$).

This analysis is carried out for several incident directions θ_1. The comparisons between theoretical and measured values for the illuminated zone's diameter show that the incident light beam presents a small divergence.

The diameter D' necessary to lead to a computed diameter value equal to the measured D'_p with a perfectly parallel beam (see Fig. 3.24) is obtained through equation (3-7) as a mean value of D'_A and D'_B , which are deduced from γ'_A and γ'_B respectively; these angles are easily calculated from the pixel differences between theoretical and measured projected diameters.
Averaging the different ratios of D_p and D'_p found with the different incident directions θ_1 chosen for this experience, a mean value for D'/D may be determined: this latter value is equal to 1.14, corresponding to an spread angle η of about 0.35°. The light source beam collimation can therefore be considered as of good quality.

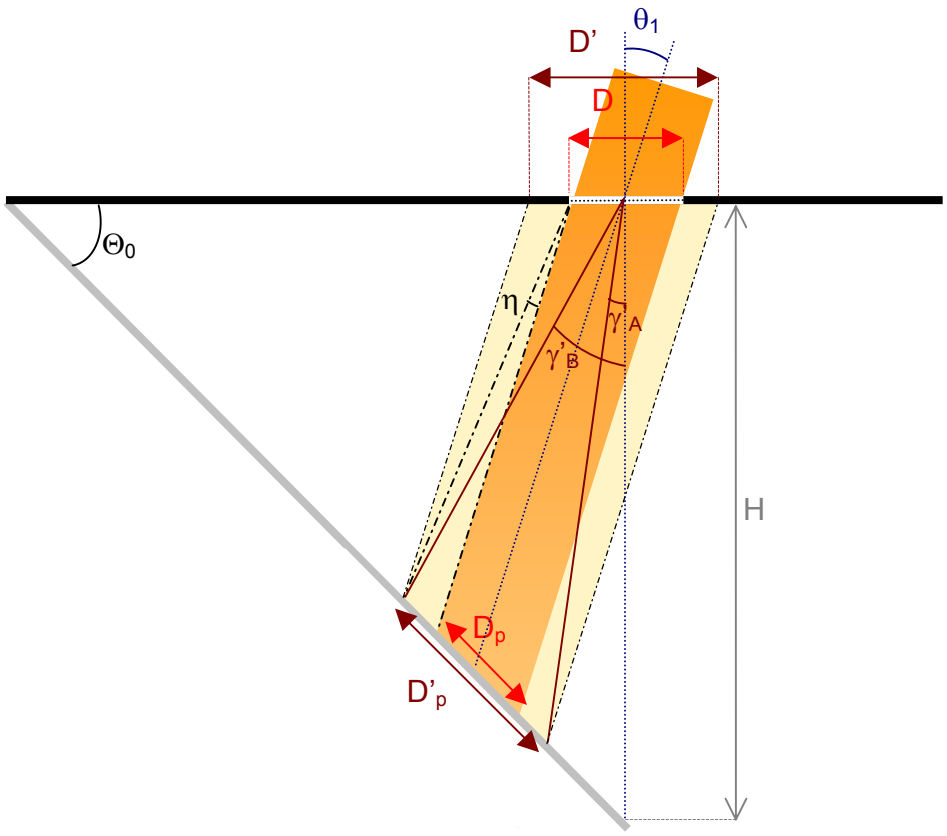

Fig. 3.24. Light beam divergence η deduced from angles γ'_A, γ'_B, and from virtual diameter D'.

$$D'_A = -\frac{2H\cos(\Theta_0-\theta_1)}{\cos\theta_1}\left(\frac{\sin\gamma'_A}{\cos(\Theta_0-\gamma'_A)}-\frac{\sin\theta_1}{\cos(\Theta_0-\theta_1)}\right)$$

$$D'_B = \frac{2H\cos(\Theta_0-\theta_1)}{\cos\theta_1}\left(\frac{\sin\gamma'_B}{\cos(\Theta_0-\gamma'_B)}-\frac{\sin\theta_1}{\cos(\Theta_0-\theta_1)}\right)$$

$$\rightarrow \quad D' \sim \tfrac{1}{2}\,(D'_A + D'_B) \qquad (3\text{-}7)$$

As the impact of this parameter in the BTDF evaluation (see § 3.3.3) is of great importance, an analytic correction is required. The factor of 1.14 is obtained when the reference situation to compare with is a perfectly collimated beam (η = 0°).
However, the real sunlight divergence being of 0.25°, we can admit this situation as an acceptable reference and choose to correct only the source beam's excess in divergence with regard to this reference. In consequence, a 1.04 correction factor is found and shall be applied to the diameter of the diaphragm, which corresponds to a correction of 8% in relative terms on the area ($A = \pi D^2/4$).

Parasitic light

Any incoming parasitic light may cause rather large measurement errors, especially if the luminance range is low. It is therefore essential to render the device impermeable to any external light except in the sample area and to avoid any possibility of glare for the camera.

The conic cap fixed on the main platform and surrounding the measurement space excludes parasitic light coming from the device's environment (dark room, mechanical support, etc.). Every internal component (rotating ring, screen support shrouds, inside face of main platform, etc.) is covered with a highly light absorbing black velvet (ρ_{velvet} < 1%).
Some images provided by the CCD camera in particular situations showed a glare effect due to parasitic reflections inside the objective lens system. This problem has been avoided thanks to a range of precisely determined dimensions and positions in order to obstruct the visualisation of the space above the screen basis (see Fig. 3.25B).

The critical area to control is therefore the sample holder: no incident light may find its way in the transmission hemisphere out from the characterised area on the sample. As this area has to present a circular symmetry, diaphragms of different opening diameter (10cm, 17cm, 24cm and 30cm) are built; they can easily be fixed on or taken away from the sample holder frame, on its external side.

On the inner side of the main platform, an opaque disk presenting a squared hole of the same dimensions as the sample holder frame is fixed.
The inevitable residual space between the platform and this disk in order to allow the latter to turn jointly with the sample holder for non null azimuths may induce light infiltration. This infiltration had therefore to be prevented with to a light trap placed around the disk.

There is a certain obstruction to emerging rays that occur for thin samples because of the non null thickness of the device components and of the parasitic light avoiding elements. This obstruction can be quantified through geometrical considerations illustrated in Fig. 3.25 and be expressed by the limit altitude angle θ_{lim} defined in (3-8):

$$\theta_{\lim} = \frac{\pi}{2} - \arctan \frac{\sin\delta \cdot \frac{\sin\Theta_0 \cdot (\frac{\sqrt{3}}{2} H - \frac{D_{out}}{2} - \frac{e}{\tan\Theta_0})}{\sin(\Theta_0 + \delta)}}{\frac{D_{out}}{2} + \cos\delta \cdot \frac{\sin\Theta_0 \cdot (\frac{\sqrt{3}}{2} H - \frac{D_{out}}{2} - \frac{e}{\tan\Theta_0})}{\sin(\Theta_0 + \delta)}} \qquad \delta = \arctan \frac{h_{obst} - e}{d_{obst} - \frac{D_{out}}{2}} \qquad (3\text{-}8)$$

where

- θ_{lim} is the maximal altitude angle reachable without any obstruction [°]
- D_{out} is the illuminated sample diameter on the output interface [m] ($D_{out} \cong D$, the divergence through the sample being generally negligible)
- h_{obst} is the determinant obstacle's height [m]
- d_{obst} is its distance to the sample center [m]
- e is the sample thickness [m]
- δ is the obstruction angle [°] (see Fig. 3.25B).

This obstruction leads to an unexplored part of the BTDF for a fraction of the "transmission hemisphere", which increases with the considered sample area (diaphragm diameter) and decreases with the sample thickness e. For thin samples, the value of θ_{lim} stays close to about 10°.

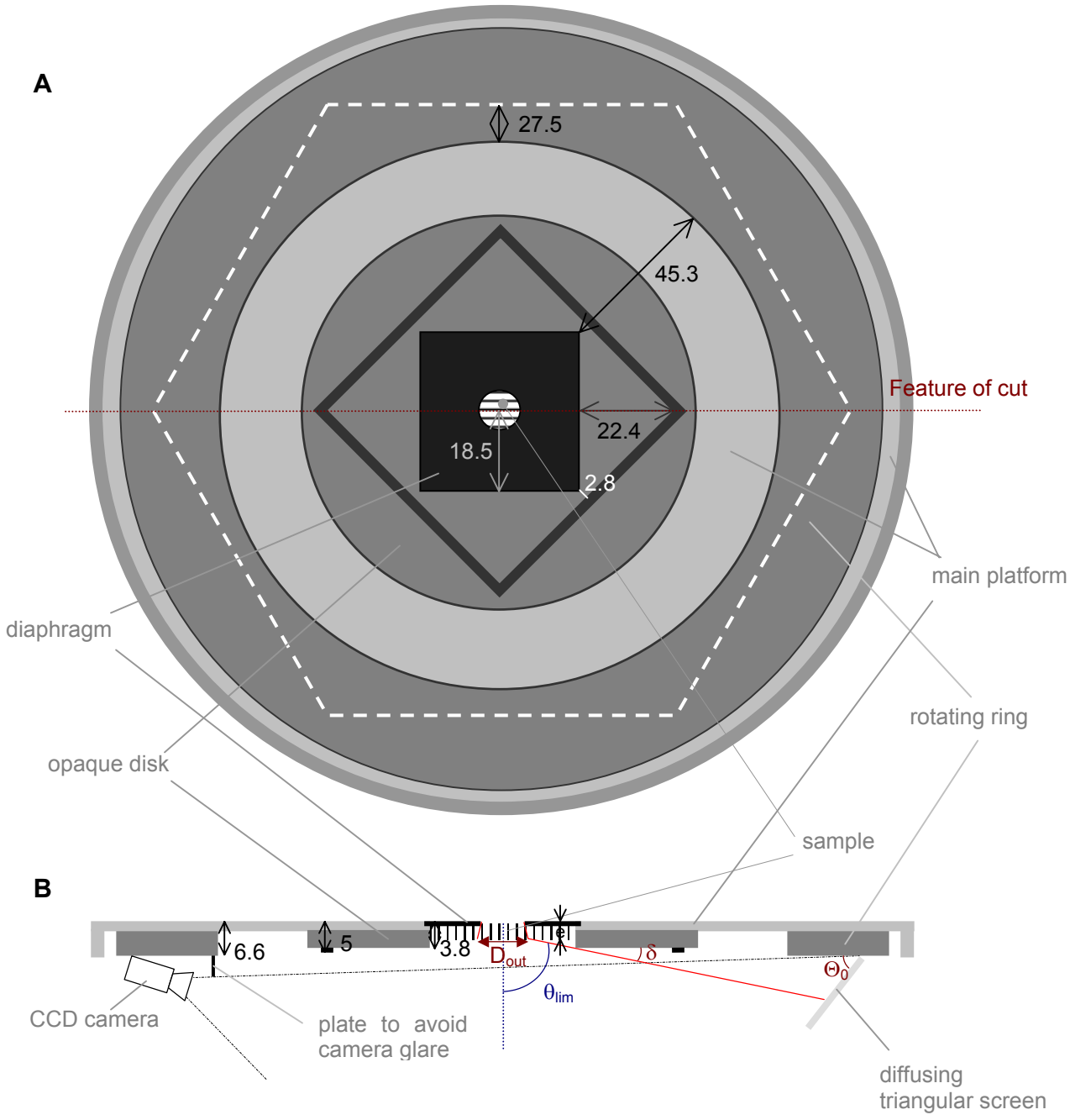

Fig. 3.25. Schematic illustration of the photogoniometer's components dimensions. The measurements are given in [cm] **A** Plan view of the device's inner side. **B** Section view along a vertical plane, with obstruction angle δ directly related to limit altitude angle θ_{lim}.

3.3 DEVICE COMMAND AND DATA PROCESSING

An automation of the characterisation procedure of fenestration samples (BTDF data) is essential to make the measurement device powerful. It is therefore necessary to work out a user-friendly driving software, which at the same time efficiently controls the driving of the photogoniometer as well as the image acquisition and final processing.

3.3.1 Piloting software

The driving software has been developed in VISUAL BASIC® (version 5.0), to achieve a fully automated sample characterisation. The main user interface is shown in Fig. 3.26; as observed in the graphical part of this interface, the default incident directions set comprises 145 different angular directions, which matches the subdivision of the sky hemisphere for luminance measurements defined by Tregenza for the International Daylighting Measurement Program [Tre87].

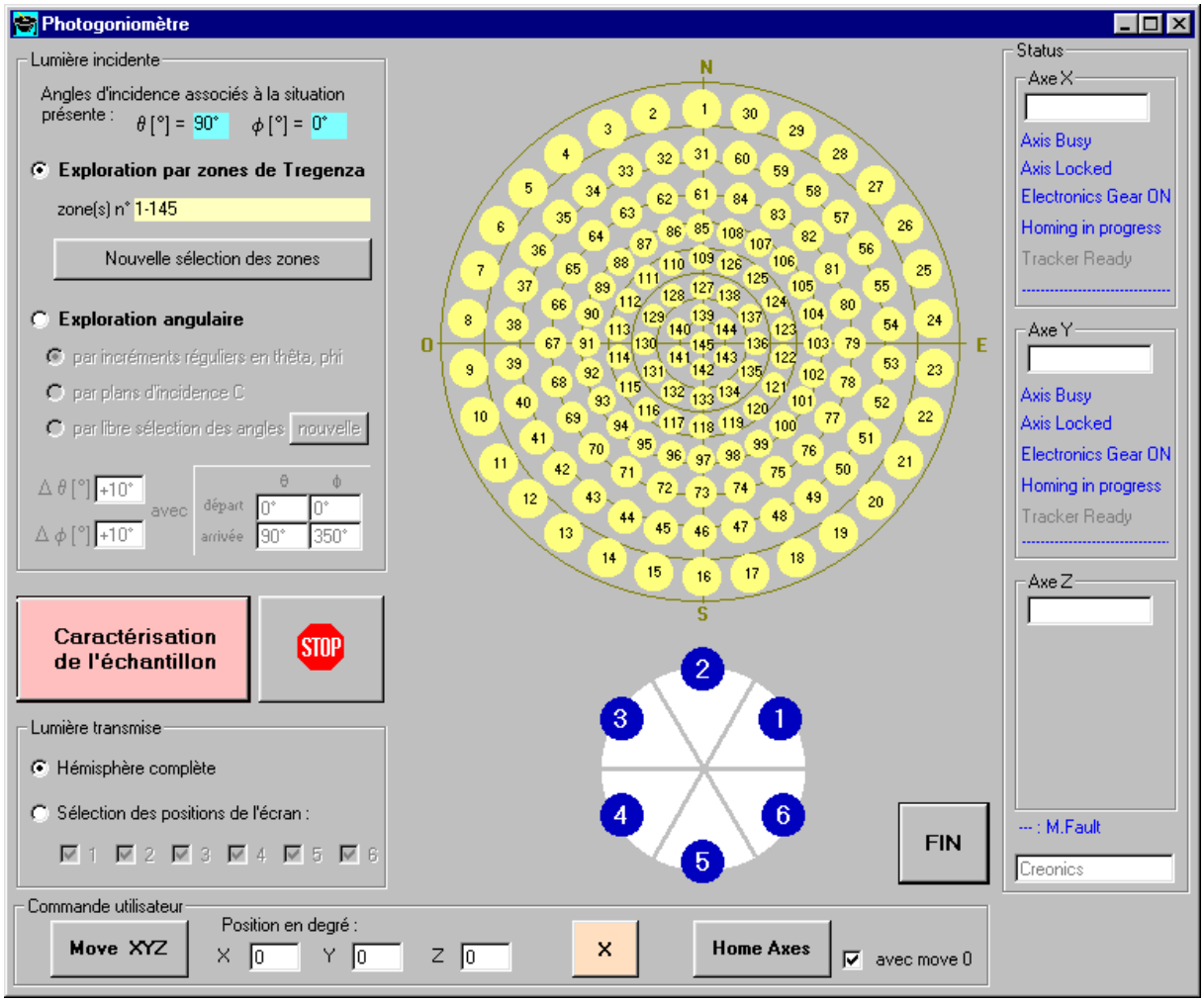

Fig. 3.26. Complete driving software interface for sample characterisations. The left and bottom parts are generally hidden: they allow a status control and device movements without any picture snap or processing.

- The desired directions within the Tregenza configuration can be selected by mouse-clicking on the stereographic view, or by choosing:
  (see Fig. 3.27 A).

- Any other angular exploration can be chosen if desired: as illustrated in Fig. 3.27 B, regular angular steps in incidence may be selected through the option:

  with free start and end points:

- Another possibility is a selection of incidences along C planes (Fig. 3.27C):

  with free altitude steps:

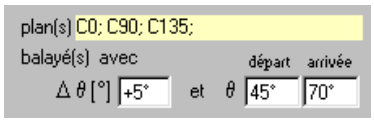

- Finally, one can openly choose a set of directions given by angle couples, thank to the additional window represented in Fig. 3.27 D, that appears when choosing:

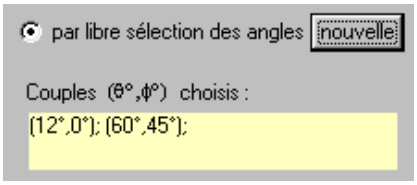

A graphical representation of the future exploration type appears for each option, through a stereographic projection of the incidence hemisphere.

For the output (transmission) part, the six screen positions shall generally be selected to allow a full knowledge of the transmission properties of the material. However, they can be selected individually, which may be useful for testing procedures for instance.
This individual selection is possible through option:

Or by mouse-clicking on the represented screen position numbers:

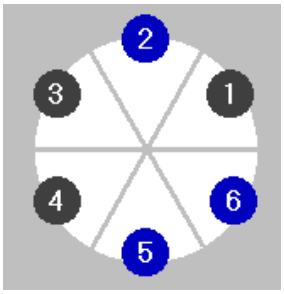

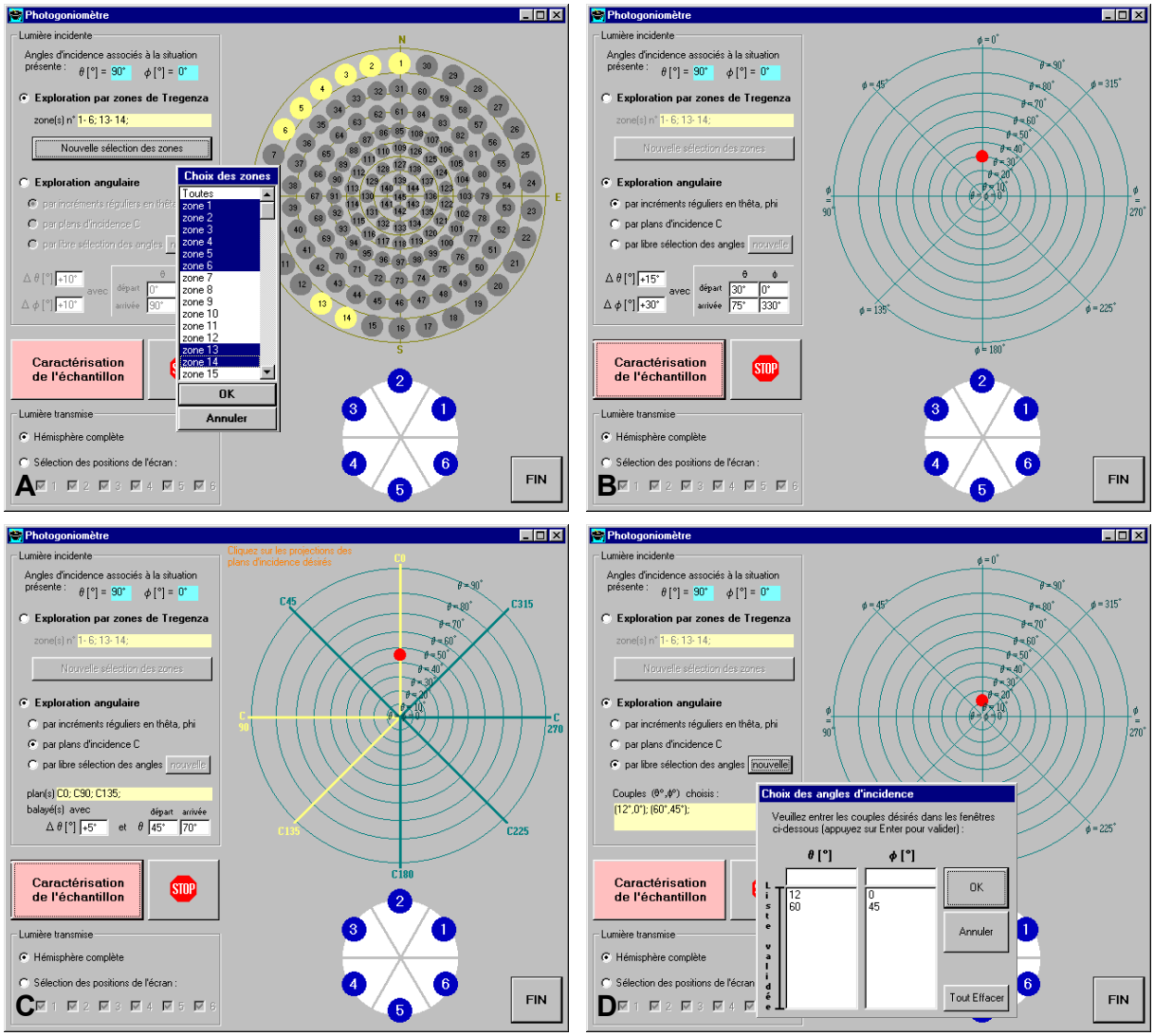

Fig. 3.27. Different possibilities offered for exploration. **A** Incident directions associated to Tregenza zones. **B** Regular angular steps in altitude and azimuth. **C** Exploration along C planes. **D** Free angle couples.

Once the exploration parameters are fully defined, the characterisation can be started by clicking on

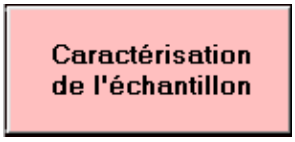

A window appears to allow the user to register the sample properties, given in Fig. 3.28A: name, manufacturer, diaphragm diameter, thickness, known symmetries, additional comments.

The characterisation may then be launched, and its march can be followed on the stereographic view, with colouring or movements of the cursor, and on the screen positions representation underneath, as represented in Fig. 3.28 B. On this example, the sample has been registered as presenting a symmetry along the vertical and horizontal axes; when choosing the complete Tregenza directions distribution, an automatic reduction of the incident positions set is applied.

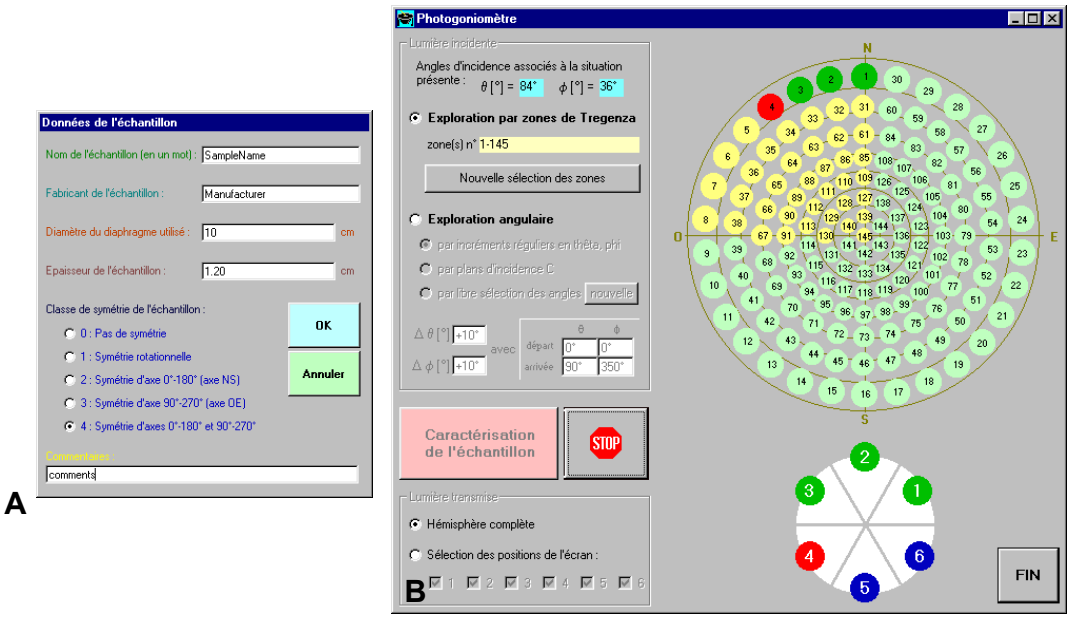

Fig. 3.28. Characterisation software interfaces. **A** Sample properties window. **B** Characterisation unfolding under Tregenza exploration type with axial symmetries along 0°-180° and 90°-270° axes.

For each incident direction, the different screen positions are investigated, with an appropriate image acquisition and data processing. The screen data are saved separately, and gathered in a single file at the end of each incident direction analysis. The calibrated screen images are resized and appropriately combined to form a hemispherical figure of the sample transmission features for the concerned incidence.

It must be noted that only about 2 to 4 minutes are necessary to acquire a complete set of BTDF data for one incident direction, versus hours for classical photogoniometers.

3.3.2 Image acquisition and processing

The transformation of information from black and white images into BTDF values asks for the development of complex and clever procedures of acquisition and data processing.

They can be divided into three phases, applied to each screen position:

- image acquisition and calibration in luminance values
- data processing for a conversion into BTDF values
- discretisation of the results according to the output angular resolution requested.

The results obtained for the different screen positions are then gathered and organised in a relevant way for creation, with each incidence, of a complete data file and an image representing the whole transmission hemisphere.

The data generation procedures are explained below; the creation of the hemispherical visualisation is detailed in § 3.4.1.

Image acquisition and calibration

The aim of the image processing is to improve the accuracy of luminance measurements and avoid over-exposure and/or under-exposure of some parts of the digital images, in presence of a high range of luminance values.

a) Acquisition and grey level to luminance conversion

An automated selection of appropriate integration intervals is achieved by the driving software to match the luminance dynamic: the largest one is just small enough to avoid over-exposure and the lowest one just large enough to avoid under-exposure.
Picture snapshots are taken at different selected integration intervals, in a highest to shortest order [Mic99].

All these images, characterised by a 8 bits discretisation (256 grey levels), are then calibrated one by one, the conversion being based on the appropriate grey level to luminance relation. Each one of them is then converted into a 32 bits (floating point) image. These conversions will allow taking benefit from a far greater dynamic in luminance values (2^{32} levels) when the images are superposed for the creation of a complete calibrated image (see c)).

b) Measurement of the illuminance on the sample plane $E_1(\theta_1)$

For each snapshot, the illuminance on the sample plane is simultaneously measured by an illuminance-meter positioned on the edge of the sample holder and connected to the computer. This sensor provides instantaneous measurements of the $E_1(\theta_1)$ value.

A total simultaneity in the acquisition of the illuminance and the image is necessary to guarantee reliable results. Indeed, all eventual light source fluctuations have to be taken into account, in particular during picture exposure.
Therefore, the multiple instantaneous illuminance values recorded during the integration time of the concerned image are averaged to obtain the effective simultaneous illuminance $E_1(\theta_1)$.

As for practical reasons the illuminance-meter is placed next to the sample holder instead of on its centre, a correction has to be applied to the measured values in order to compensate this difference.

A comparison between the values obtained on these two positions for the same luminous situation was therefore realised by simultaneous measurements with a pair of identical illuminance-meters. The results obtained are given in Fig. 3.29 by the ratio of the illuminance measured on the sample centre E_{centre} and on the sample holder's edge E_{edge}.
The deduced polynomial relation between these quantities is applied to the measured illuminance associated to the different snapshots.

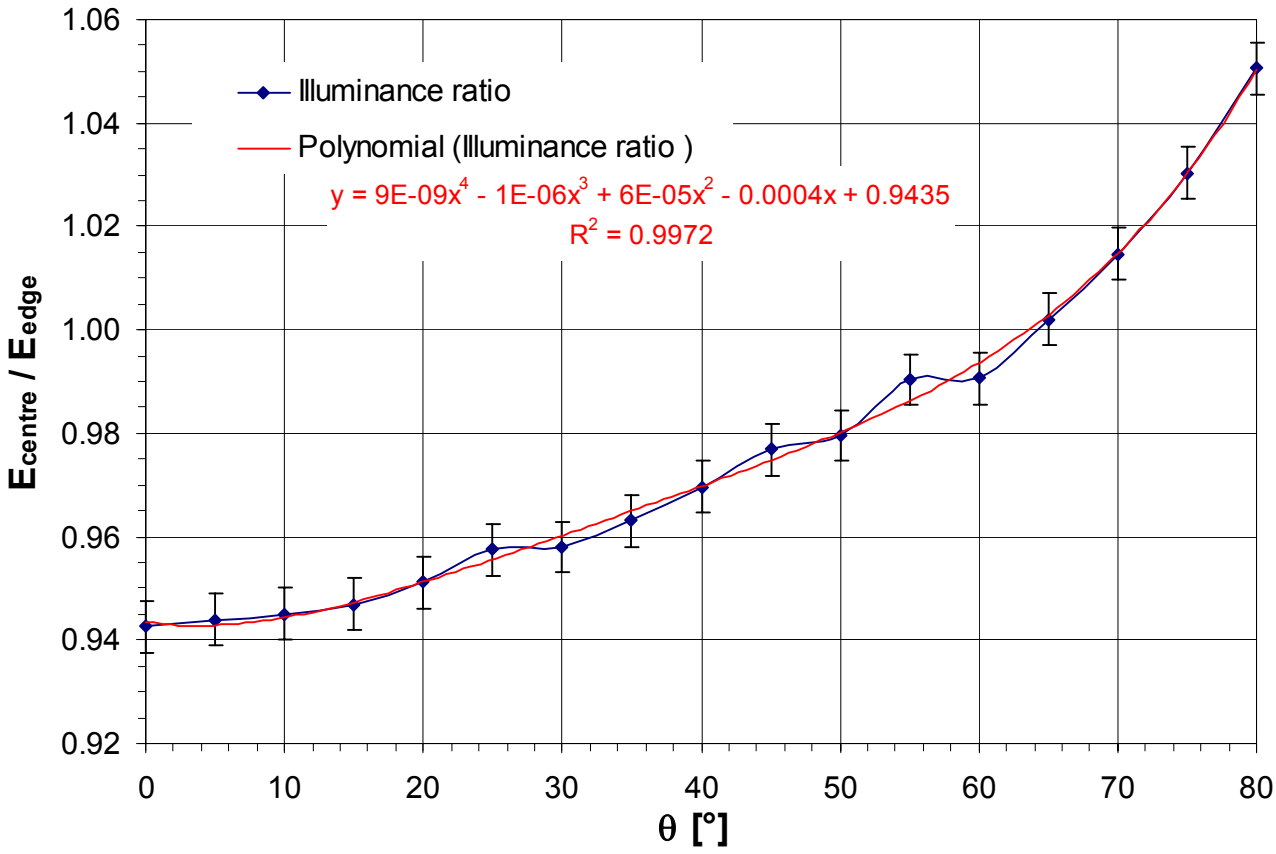

Fig. 3.29. Relation between the illuminance measured on the sample centre and on the sample holder's edge.

Each calibrated 32 bits image is then divided by the corresponding corrected simultaneous illuminance $E_1(\theta_1)$: the value of every pixel, in consequence, is at this stage equal to the ratio of the "screen luminance" $L_{screen}(\theta_1, \phi_1, \theta_2, \phi_2)$, sensed by the CCD camera after appropriate calibration, to the sample plane illuminance $E_1(\theta_1)$.

c) Combination of the calibrated images and multiplication by the correction figure

Placed in the order of the brightest to the darkest, the different grey level images (8 bits images) will have their over-exposed (grey level > 200) or already treated pixels (by a higher integration interval) set to null; the remaining pixels are set to one [Mic99].

These obtained binary images, called masks, are converted into 32 bits (floating-point) images, and each one is multiplied by the corresponding calibrated $L_{screen}(\theta_1, \phi_1, \theta_2, \phi_2)$ / $E_1(\theta_1)$ image.

The different partly nullified 32 bits images achieved are added to form a complete calibrated 32 bits image, providing a continuous map of the $L_{screen}(\theta_1, \phi_1, \theta_2, \phi_2)$ / $E_1(\theta_1)$ values, each one being based on a calibration appropriate to the concerned luminance dynamic.

The obtained image is finally multiplied by the correction figure shown in Fig. 3.21, in order to compensate the image non-uniformity and the imperfect diffusion of the triangular screen.

The different procedures are summarised in Table 3.1.

<table>
<tr><td>1</td><td colspan="2">Selection of the set of N integration times adequate to analyse the given luminous situation.</td></tr>
<tr><td>2</td><td colspan="2">Acquisition of N grey level images, each one associated to a selected integration time.</td></tr>
<tr><td rowspan="2">3</td><td rowspan="2">For each of the N grey level images :</td><td>Conversion of grey levels into luminance values.
Division by simultaneous illuminance $E_1(\theta_1)$.
Transformation into a floating-point image → calibrated image.</td></tr>
<tr><td>Creation of a mask figure, composed of pixels equal to:
• 1 if not under or over exposed, and if not treated by a higher integration time
• 0 otherwise.
Transformation into a floating-point image → mask.</td></tr>
<tr><td>4</td><td colspan="2">Multiplication of each mask with its corresponding calibrated image → N calibrated masked images.</td></tr>
<tr><td>5</td><td colspan="2">Combination of the N calibrated masked images → complete calibrated image.</td></tr>
<tr><td>6</td><td colspan="2">Multiplication of the complete calibrated image by the correction figure (Fig. 3.21) → complete calibrated corrected image = final screen image.</td></tr>
</table>

Table 3.1. Basic list of operations effectuated on a given image in order to achieve the complete calibrated figure.

A more detailed presentation of the applied procedures is given in a synoptic flow chart in Fig. 3.30:

- the ellipses correspond to the kind of operations effectuated
- the diamonds to conditional tests
- the rectangles to achieved objects.

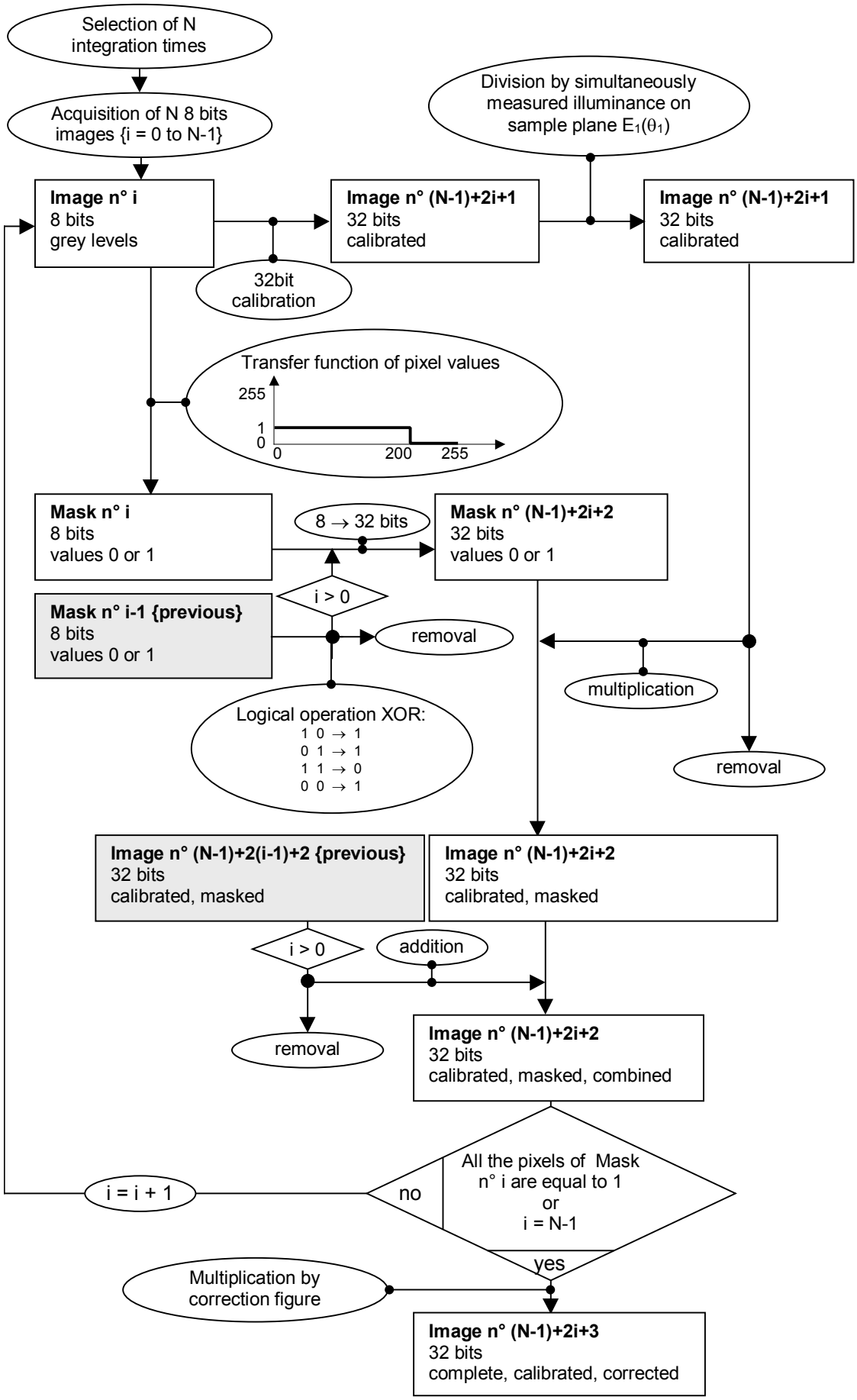

Fig. 3.30. Synoptic flow chart of image calibration and combination procedures.

Application of angular discretisation grid

Depending on the desired angular resolution, a discretisation grid has to be created before characterisation of the fenestration sample. The IMAGEPRO PLUS® software allows producing a grid based on grey level differences and registering it as a set of Areas of Interest (AOI), inside which measurements can be made; in particular, the mean value and the number of included pixels can be calculated for each AOI.
An example of AOI set is shown in Fig. 3.31, which is based on an angular resolution ($\Delta\theta_2$, $\Delta\phi_2$) equal to (10°,15°), like in Fig. 3.19.

As observed in Fig. 3.31, the AOI are automatically numerated by IMAGEPRO PLUS® according to an order based on the X- and Y-axis co-ordinates of their highest pixel. This requires a re-numerating procedure in order to have a new order based on an angular logic. A conversion file is therefore created and is read during data processing.

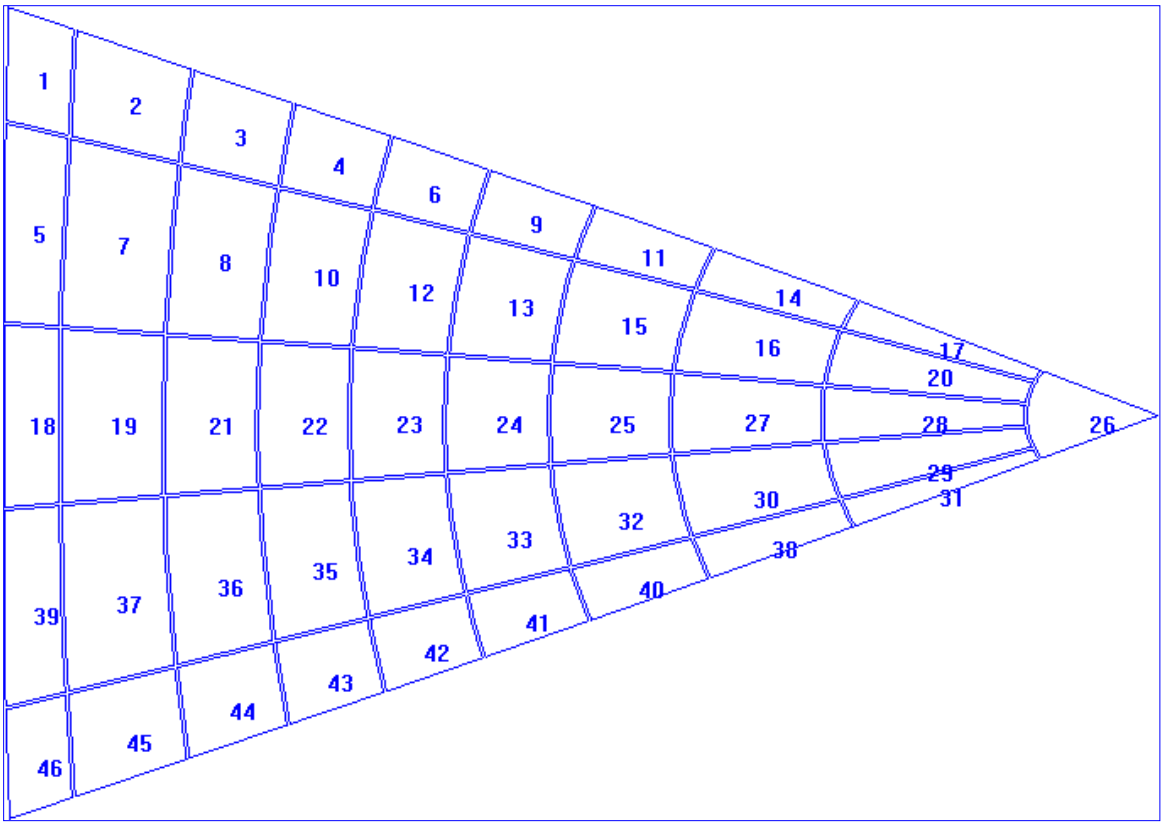

Fig. 3.31. Discretisation grid for an angular output resolution ($\Delta\theta_2$, $\Delta\phi_2$) = (10°,15°).

The pixel values of the complete calibrated 32 bits images are thus averaged to meet this kind of angular discretisation grid; the mean values and concerned areas (in pixels) are registered in a file for each screen position. An analytical conversion is then applied to deduce the BTDF values (coming out from the sample centre) from the associated $L_{screen}(\theta_1, \phi_1, \theta_2, \phi_2)$ / $E_1(\theta_1)$ quantities, taking distance and light tilting effects into account (see § 3.3.3).

At the end of an incident direction analysis, the different screen data files are merged into one, whereby the angular outgoing directions that overlap on two screen positions are taken together through an area pondered average.

As a result of image processing, the achieved data represent average values of the BTDFs measured in the output hemisphere regions limited by (ϕ_2 - ½$\Delta\phi_2$; ϕ_2 + ½$\Delta\phi_2$) in azimuth and by (θ_2 - ½$\Delta\theta_2$; θ_2 + ½$\Delta\theta_2$) in altitude for each outgoing direction. As a matter of fact, they do not only characterise the precise direction (θ_2, ϕ_2) to which they are associated, but can therefore vary according on the angular resolution ($\Delta\theta_2$, $\Delta\phi_2$).

3.3.3 Data conversion

Transformation into BTDF values

The data acquisition procedures lead to the knowledge of $L_{screen}(\theta_1, \phi_1, \theta_2, \phi_2)$ / $E_1(\theta_1)$ ratios that have to be converted into BTDF values. This transformation requires an analysis of the geometrical properties of the photogoniometer, illustrated by Fig. 3.32, and an application of the existing relationships between photometric quantities.

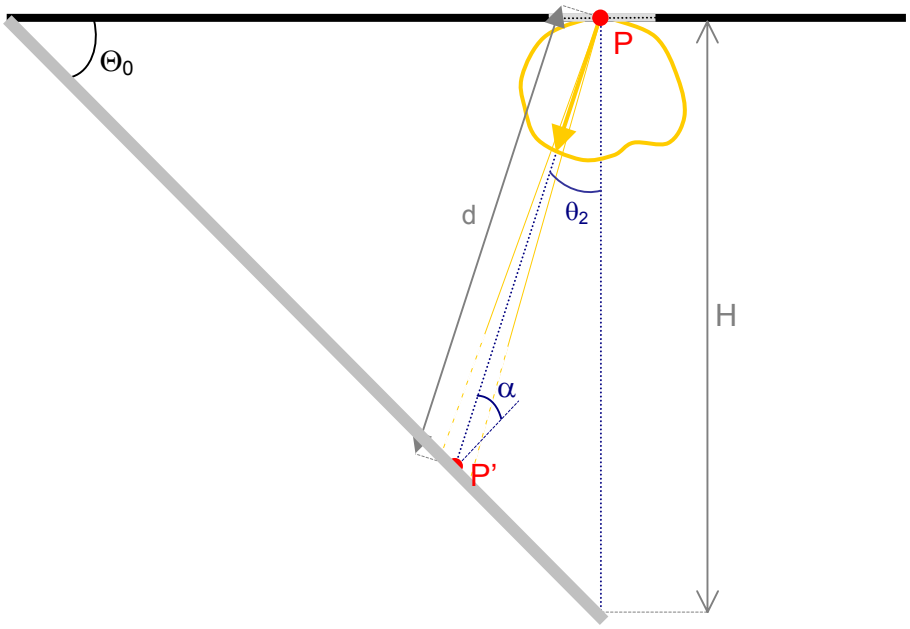

Fig. 3.32. Schematic illustration of an element of light flux emerging from the sample's output interface and reaching the triangular screen.

Let us consider the sample's output interface as a secondary light source; quantities relative to the sample or to the screen are respectively indicated by P and P', as a reference to the points located in Fig. 3.32.

Based on the definition of intensity and luminance, we may write equations (3-9):

$$L_P = \frac{d\Phi_2}{d\omega_2 \cdot A\cos\theta_2} = \frac{d\Phi_2}{\frac{dS\cdot\cos\alpha}{d^2}\cdot A\cos\theta_2} = \frac{I_P}{A\cos\theta_2}$$

$$E_{P'} = \frac{d\Phi_2}{dS} = \frac{I_P\cdot\cos\alpha}{d^2} = \frac{L_P\cdot A\cos\theta_2\cdot\cos\alpha}{d^2} \qquad (3\text{-}9)$$

where

- L_P is the luminance along direction (θ_2,ψ_2) from the output interface of the sample [cd · m^2]
- I_P is the intensity along direction (θ_2,ψ_2) [cd]
- A is the illuminated area of the sample [m^2]
- $d\Phi_2$ is an element of flux in direction (θ_2,ψ_2) [lm]
- $d\omega_2$ is a solid angle under which the surface element dS is seen along direction (θ_2,ψ_2) [sr]
- d is the distance from screen to sample centre, along direction (θ_2,ψ_2) [m]
- α is the angle between direction (θ_2,ψ_2) and the normal to the screen [°]; its analytical expression is given below
- $E_{P'}$ is the illuminance on the screen at the position associated to direction (θ_2,ψ_2) [lx].

As the screen may reasonably be considered as a lambertian surface (see § 3.2.4), a linear relation appears between the "screen" luminance $L_{P'}(\theta_1, \phi_1, \theta_2, \psi_2) = L_{screen}(\theta_1, \phi_1, \theta_2, \phi_2)$ and the illuminance $E_{P'}(\theta_1, \phi_1, \theta_2, \psi_2)$, which is leads to equations (3-10):

$$L_{P'} = \frac{\rho \cdot E_{P'}}{\pi} = \frac{\rho \cdot L_P \cdot A\cos\theta_2 \cdot \cos\alpha}{\pi \cdot d^2}$$

i.e. $$L_P = \frac{\pi \cdot d^2 \cdot L_{P'}}{\rho \cdot A\cos\theta_2 \cdot \cos\alpha} = \frac{\pi}{\rho} \cdot \frac{d^2(\theta_2,\psi_2)}{A \cdot \cos\theta_2 \cdot \cos\alpha} \cdot L_{screen}(\theta_1,\phi_1,\theta_2,\phi_2) \qquad (3\text{-}10)$$

where ρ is the reflection coefficient of the screen [-].

The definition of the BTDF as the ratio of the outgoing luminance $L_2(\theta_1,\phi_1,\theta_2,\phi_2) = L_{screen}$ and the illuminance on the sample plane $E_1(\theta_1) = E_P$ (see § 2.1) leads to the final equation (3-11), where d is defined by (3-3), ρ being taken equal to 0.743 (see § 3.2.4):

$$BTDF(\theta_1,\phi_1,\theta_2,\phi_2)\left[\frac{cd}{m^2 \cdot lx}\right] = \frac{\pi}{\rho} \cdot \frac{d^2(\theta_2,\psi_2)}{A \cdot \cos\theta_2 \cdot \cos\alpha} \cdot \frac{L_{screen}(\theta_1,\phi_1,\theta_2,\phi_2)}{E_1(\theta_1)} \qquad (3\text{-}11)$$

α is defined as the angle between the direction (θ_2,ψ_2) and the normal to the projection screen. Along a vertical plane (i.e. for $\psi_2 = 0$), its expression is simply given by equation (3-12), as observed in Fig. 3.32 for instance:

$$\alpha(\phi_2 = 0) = \left|\Theta_0 - \theta_2\right| \qquad (3\text{-}12)$$

In the general case, the analytical relation defining α is more complicated, as three-dimensional trigonometric considerations have to be applied. These considerations are illustrated by Fig. 3.33 and lead to equation (3-13):

$$\alpha = \arccos\frac{H\cos\Theta_0}{d} \overset{(3-3)}{=} \arccos\frac{2\cos\Theta_0 \cdot (\sin\theta_2\cos\psi_2 + \frac{\sqrt{3}}{2}\cos\theta_2)}{\sqrt{3}} \qquad (3\text{-}13)$$

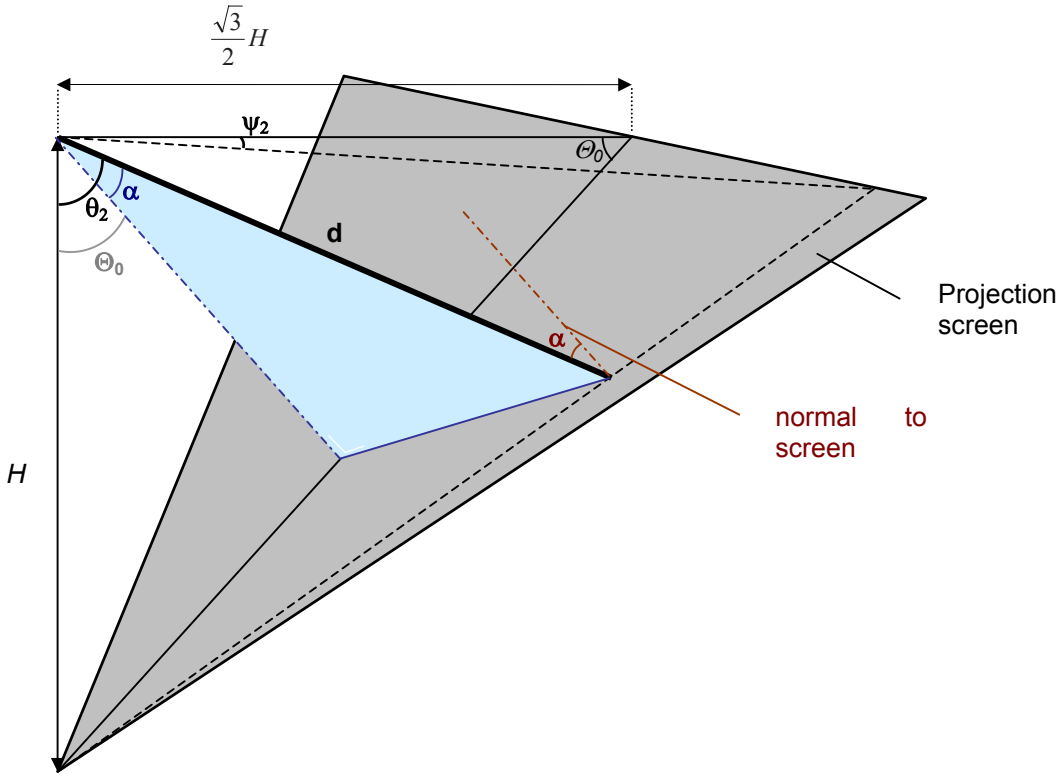

Fig. 3.33. Geometric quantities necessary to define angle α.

As observed in Fig. 3.33, α becomes equal to $|\Theta_0 - \theta_2|$ only if the delimiting lines of these three angles belong to the same plane, which effectively appears to be true only with a null azimuth ψ_2.

The $L_{screen}(\theta_1, \phi_1, \theta_2, \phi_2) / E_1(\theta_1)$ data, obtained after applying the discretisation grid on the calibrated images, correspond to zones of pixels limited by (ψ_2 - ½$\Delta\psi_2$; ψ_2 + ½$\Delta\psi_2$) in azimuth and by (θ_2 - ½$\Delta\theta_2$; θ_2 + ½$\Delta\theta_2$) in altitude (see Fig. 3.14); these zones are associated to the angular couples (θ_2, ψ_2), and therefore to the related distances d.

Except for the edge zones, the angles (θ_2, ψ_2), and therefore the value of d, are very similar to the polar co-ordinates (θ_{2G}, ψ_{2G}), - and the distance d_G -, corresponding to the discretisation zones' centre of gravity. But on the apex (i.e. (θ_2, ψ_2) = (0°, 0°)) and along the borders of the screen (i.e. $\psi_2 = \pm 30°$ or $\theta_2 = \theta_{lim}$), it may not be the case.
Therefore, (θ_{2G}, ψ_{2G}) and d_G are chosen to be the reference values to take into account in the evaluation of the BTDF values through relation (3-11).

As explained before, equation (3-11) is applied after calculation of the different mean values for $L_{screen}(\theta_1, \phi_1, \theta_2, \phi_2) / E_1(\theta_1)$ inside each discretisation zone, and after a renumerating procedure of these zones. The overlap of a zone on two screen positions is treated by an area pondered average at the end of an incident direction analysis, when gathering the different individual screen data files.

Light transmittance

From a complete BTDF data set, it is possible to calculate the hemispherical light transmittance $\tau(\theta_1, \phi_1)$. This information is effectively of great importance in the validation of the measurements on one side (see § 3.3.4) and in the qualification of the global photometric behaviour of a fenestration material on the other side.

In order to determine the relation between $\tau(\theta_1, \phi_1)$ and the BTDF values, a hemisphere centred out of P (see Fig. 3.34) and of arbitrary radius R_0 is considered. Each discretisation zone is projected on the hemisphere according to a spherical rectangle, like illustrated in Fig. 3.34.

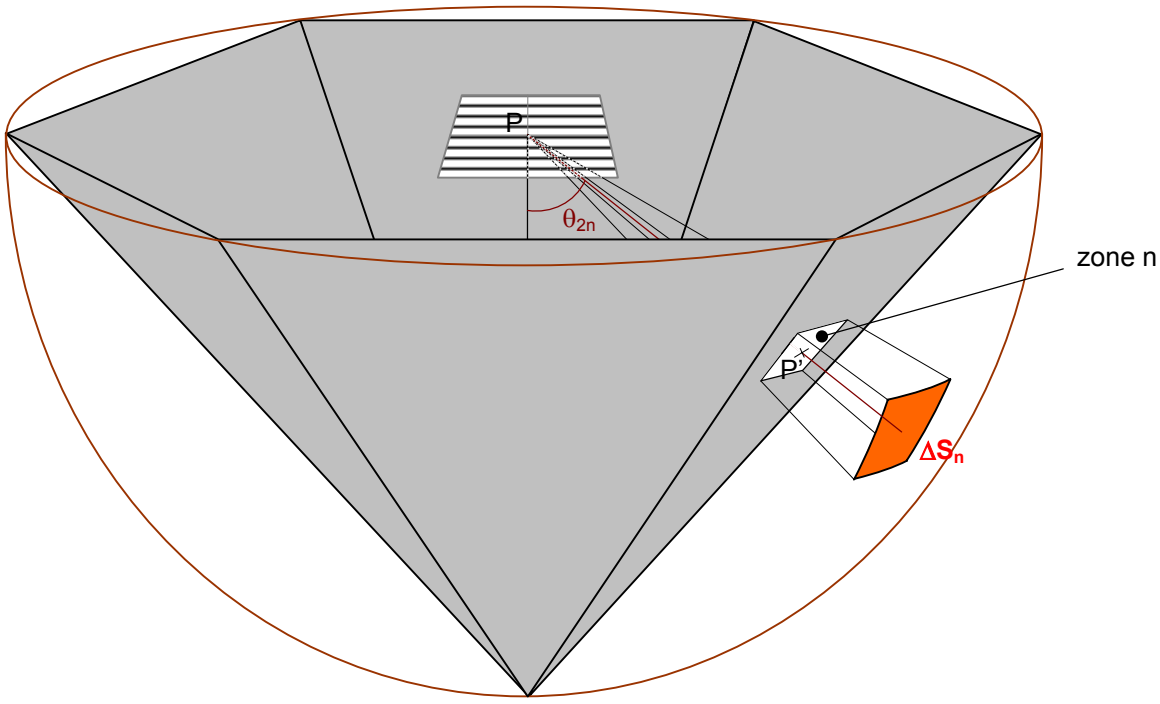

Fig. 3.34. Subdivision of the transmission hemisphere into projected discretisation zones.

Let us consider the subdivision of the hemisphere into such elements of surface, that we shall call ΔS_n, n = 1 to N_{out}, N_{out} being the total number of angular directions, discretising the outgoing hemisphere.
As a result of spherical geometry, we can define ΔS_n as follows:

$$\Delta S_n = R_0^{\,2} \cdot \sin\theta_{2n} \cdot \Delta\theta_2 \cdot \Delta\phi_2 \qquad (3\text{-}14)$$

In addition, from the definitions of luminous illuminance and intensity, we may write equation (3-15), the different quantities being defined as in equation (3-9):

$$E_{\Delta S_i} = \frac{I_P}{R_0^{\,2}} \qquad E_{P'} = \frac{I_P \cdot \cos\alpha}{d^2} \qquad \rightarrow \qquad E_{\Delta S_i} = E_{P'} \cdot \frac{d^2}{R_0^{\,2}} \cdot \frac{1}{\cos\alpha} \qquad (3\text{-}15)$$

where $E_{\Delta Sn}$ is the illuminance recieved on the element of surface ΔS_n.

What we want to calculate is the hemispherical transmission factor, i.e. the ratio of the transmitted flux Φ_2 and the incident flux Φ_1.
The transmitted flux Φ_2 can be expressed as the integration over the whole hemisphere of infinitesimal elements of flux $d\Phi_2$, that we will approximate by a sum over all discretisation zones. It is given through the following equations:

$$\begin{aligned}
\Phi_2 &= \int_{hemisphere} d\Phi_2 \\
&\cong \sum_{n=1}^{N_{out}} \Delta\Phi_{2n} \\
&\cong \sum_{\wedge n=1}^{N_{out}} E_{\Delta S_n} \cdot \Delta S_n \\
&\overset{(3-15)}{\cong} \sum_{n=1}^{N_{out}} E_{P'n} \frac{{d_n}^2}{{R_0}^2} \cdot \frac{1}{\cos\alpha_n} \cdot \Delta S_n \\
&\overset{(3-10)}{\cong} \sum_{n=1}^{N_{out}} \frac{\pi}{\rho} L_{P'n} \cdot \frac{{d_n}^2}{{R_0}^2} \cdot \frac{1}{\cos\alpha_n} \cdot \Delta S_n \\
&\cong \frac{\pi}{\rho} \cdot \frac{1}{{R_0}^2} \cdot E_1 \cdot \sum_{n=1}^{N_{out}} \frac{L_{screen_n}}{E_1} \cdot {d_n}^2 \cdot \frac{1}{\cos\alpha_n} \cdot \Delta S_n \\
&\overset{(3-11)}{\cong} \frac{A}{{R_0}^2} \cdot E_1 \cdot \sum_{n=1}^{N_{out}} BTDF_n \cdot \cos\theta_{2n} \cdot \Delta S_n \\
&\overset{(3-14)}{\cong} \frac{A}{{R_0}^2} \cdot E_1 \cdot \sum_{n=1}^{N_{out}} BTDF_n \cdot \cos\theta_{2n} \cdot {R_0}^2 \cdot \sin\theta_{2n} \cdot \Delta\theta_2 \cdot \Delta\phi_2 \\
&\cong A \cdot E_1 \cdot \Delta\theta_2 \cdot \Delta\phi_2 \cdot \sum_{n=1}^{N_{out}} BTDF_n \cdot \cos\theta_{2n} \cdot \sin\theta_{2n}
\end{aligned} \qquad (3\text{-}16)$$

On the other side, the incident flux Φ_1 is given by equation (3-17):

$$\Phi_1 \cong E_1 \cdot A \qquad (3\text{-}17)$$

These results lead to the following expression for $\tau(\theta_1, \phi_1)$:

$$\tau(\theta_1,\phi_1) \cong \Delta\theta_2 \cdot \Delta\phi_2 \cdot \sum_{n=1}^{N_{out}} BTDF_n(\theta_1,\phi_1,\theta_{2n},\phi_{2n}) \cdot \cos\theta_{2n} \cdot \sin\theta_{2n} \qquad (3\text{-}18)$$

As detailed in § 3.2.4, a certain obstruction to emerging rays may appear for very thin samples, leading to a lack in the determination of the BTDF values for the corresponding directions on the transmission hemisphere. The assessment of $\tau(\theta_1, \phi_1)$, in consequence, requires an extrapolation of the data for extreme values of θ_2.
During the creation of the final data file (see § 3.4.1), the light transmittance is thus calculated thank to relation (3-18) and registered.

It must finally be noted that the calculation of τ becomes heavy and tedious in case of irregular output angular resolutions, which are often used for conventional photogoniometric measurements (mobile photometer) [Api94]. Thanks to digital imaging techniques, this problem disappears, the continuity of the information leading to an exclusion of any risk of missing an important feature in transmission.

3.3.4 Experimental validation

The validation of the results is lead by two different ways:

- a detailed list of the possible sources of error followed by an estimation of the global incertitude associated to the measurements
- a validation of the BTDF values through a comparison of the hemispherical transmittances calculated from a numerical integration of these data (using equation (3-18)) on one hand, and by experimental assessment of this transmittance thanks to an Ulbricht integrating sphere on the other hand.

As a matter of fact, as most bi-directional photogoniometers are still in the testing stage, there is no extended BTDF data set accurate enough to be taken as a reference for validation purposes. A comparison of BTDF values of the same sample measured with different photogoniometers [Pap88] [Api94] [Bak95] will be possible as soon as a larger data set will be available.

Another way to confirm our results is a comparison with analytically expressed BTDF values, for well-known situations (an open hole or a lambertian sample); this verification has already been done when creating the correction figure to compensate the effects due to the image non-uniformity and the imperfect diffusion of the screen (see § 3.2.4). The correction factors' range being of 0.88 to 1.13, it has been observed that the measurements fitted the theoretically expected values with good accuracy (even before a full correction of the values), the maximal differences being of 13%. This result could therefore guarantee quality measurements performed by this digital imaging technique based photogoniometer, after the calibrations detailed in § 3.2.

Error sources

The multiple calibrations necessary to assess the final BTDF values implicate several possible sources of error in their measurement. It is therefore important to evaluate the inaccuracies eventually induced at each calibration step, due to the data acquisition methodology.

a) Spectral calibration

The relative error f'_1, defined by equation (3-19), indicates the degree to which the relative spectral sensitivity $S(\lambda)$ matches the spectral luminous efficiency $V(\lambda)$ of the human eye for photopic vision [CIE87]. It is given by the following equation:

$$f'_1 = \frac{\int_0^\infty |S(\lambda) - V(\lambda)| \cdot d\lambda}{\int_0^\infty V(\lambda) \cdot d\lambda} \cdot 100\% \cong 0.93584 \cdot \sum_{k=1}^{34} |S(\lambda_k) - V(\lambda_k)| \cdot \Delta\lambda_k \quad [\%] \qquad (3\text{-}19)$$

The corresponding f'_1 value obtained for our photogoniometer is equal to 10%.
It must nevertheless not be concluded that the measured BTDF data will present at least an error of 10%. Indeed, this effect will appear only as a second order error, as the

photometric calibration will compensate its influence by providing the grey level to luminance relations by taking the spectral calibration into account.

A more significant error source induced by an imperfect spectral calibration is, in consequence, due to the dissimilarities of the light source used for photometric calibration (halogen lamp) and the one taken as incident beam source for sample characterisation (HMI discharge lamp). This effect can be characterised by the photometric error ε [%], defined in [CIE87] and given in our case by equation (3-20):

$$\varepsilon[\%] \cong \frac{\left(\sum_{k=1}^{34} S(\lambda_k) E_{meas}(\lambda_k) \Delta\lambda_k\right)\left(\sum_{k=1}^{34} V(\lambda_k) E_{calib}(\lambda_k) \Delta\lambda_k\right)}{\left(\sum_{k=1}^{34} V(\lambda_k) E_{meas}(\lambda_k) \Delta\lambda_k\right)\left(\sum_{k=1}^{34} S(\lambda_k) E_{calib}(\lambda_k) \Delta\lambda_k\right)} \qquad (3\text{-}20)$$

where

- $E_{meas}(\lambda)$ is the energetic spectrum of the light source used for BTDF measurements [$\mu W\ cm^{-2}\ sr^{-1}$]
- $E_{calib}(\lambda)$ is the energetic spectrum of the light source used for photometric calibration [$\mu W\ cm^{-2}\ sr^{-1}$]

This photometric error ε is lower than 4%, which indicates a minor influence of the spectral calibration inaccuracies in the achieved measurements.

b) Photometric calibration

Apart from the photometric error ε treated above, the photometric calibration may induce uncertainties in the determination of the relation between grey levels and corresponding luminances. Indeed, even if considering the calibrated luminance-meter (see § 3.2.2) as perfectly reliable, a certain variation in the provided luminance values occurs for a given luminous situation, probably mostly due to incident light source fluctuations. Moreover, the analysed illuminated zone on the diffusing screen (see Fig. 3.10) presents a standard deviation among the concerned grey levels.

These two errors can be considered as almost negligible:

- the relative fluctuation of the luminance values effectively varies only from about 0.3% (high luminance values) to 2% (lowest luminance values)
- the grey level standard deviation stays lower than 1% in relative terms, which means absolute differences of less than 1 level in average.

c) Geometric calibration

As the determined relation between the polar co-ordinates (θ_2, ψ_2) and the cartesian screen co-ordinates (i, j) are based on purely trigonometric considerations, the only errors that may occur are due to:

- an eventual wrong positioning of the triangular screen
- some drawing approximations when creating the map screen (see Fig. 3.13)
- the variation of the co-ordinates' referential with the sample thickness

Indeed, as the incertitude linked to the location of lines intersections on the image (which completes the geometric calibration) is of less than 1 pixel, it can without a doubt be considered as negligible.

The inclination angle Θ_{0meas} of the triangular panel has been measured with a micrometric protractor and found to be equal to 49.05°, which certainly can be accepted as a very good approximation of Θ_0 = atan $2/\sqrt{3} \cong 49.1°$. The distance from base to sample centre has been checked, and corresponds to $\sqrt{3}H/2$ = 9.96 m with a precision of 0.03 m, which has no impact on the geometric calibration.

As far as the calibration grid drawing is concerned, the distances have been reported with half millimetre incertitudes, of no effect either on a 1 pixel inaccurate picture location.

Finally, the uncertainty about the co-ordinates' referential caused by a varying sample thickness appears to have significant consequences only when the desired output resolution becomes very fine (i.e. finer than 2°).
As such accuracy over the output does not need to be reached within the framework of this project, the approximation of a unique referential that was considered for geometric calibration is widely sufficient. Further developments in the data processing methodology could be required to go beyond this restriction.

For the desired sample characterisations accuracy, the geometric calibration can therefore be considered as having no impact on the measurement quality.

d) Image uniformity and screen diffusion correction

The compensation of image non-uniformity and imperfect screen diffusion (see § 3.2.4) allows to reduce the measurement error. This correction nevertheless cannot ensure a complete avoidance of these effects in the data acquisition, as a certain fluctuation of their repercussions cannot be excluded; these variations can however hardly be evaluated with precision.
Based on the growth order of the correction factors represented in Fig. 3.21 and of the effects they do compensate (image non-uniformity and imperfect screen diffusion), an incertitude of 2% on these factors can be considered as reasonable.

e) Incident beam uniformity and collimation

The illuminance uniformity over the 40x40cm^2 sample area has been checked to present a mean deviation of 1.8% on a horizontal plane, and of 3.7% when the inclination is maximal (law of Bouguer, see § 3.2.4).
It must however be noted that the considered area is often reduced, by the use of diaphragms of 10, 17, 24 or 30cm diameter. These variations are therefore decreased and the deviation to ascribe becomes very low for the most used apertures, i.e. 10 and 17cm.
One may therefore consider this source of error as negligible.

The collimation quality of the incident beam has been thoroughly studied (§ 3.2.4), and found to be equal to 0.35°, with an incertitude of about 0.04°. The correction factor applied to the diameter is therefore defined as equal to 1.04 ± 0.02, which directly affects

the area value with a possible error of 3% in relative terms (see equations (3-21) and (3-22)).

f) Parasitic light

It is important to check out if the highly absorbing black velvet covering the internal components of the photogoniometer combined with the light trap placed around the sample holder (see § 3.2.4) are sufficient precautions to avoid significant parasitic light during the measurements.

This analysis was carried out with a fully opaque sample in order to have no incoming light through the sample area.
Snapshots were then taken with every integration interval used: it has been verified that the maximal grey level observed was of 48 on the grey scale, independently of the exposure time, with a mean value of 42.5, which corresponds to a luminance of 0.146 [cd/m^2] for the largest integration time (2.56 sec).
Therefore, the photometric calibration curves were put to zero for grey levels lower than 49 on the grey scale (see Fig. 3.11).

It was then checked that for a highly transmitting element, internal reflections will not affect the BTDF assessment.
For this purpose, snapshots with no sample were calibrated and superposed without nullification below the grey level 49, the plain hole being taken as an extreme case of a highly transmitting sample.
The luminances obtained out of the illuminated zone were analysed: it was observed that the "background" value was of about 0.15 [cd/m^2]. This luminance value can be considered as null, as it is very close to the 0.146 [cd/m^2] obtained with an opaque sample (see above).

In consequence, it was demonstrated that assessing the photometric calibration curves to zero below 49 was a sufficient practical measure to avoid any significant influence of internal reflection.
This method nevertheless implicates that screen luminance values inferior to 0.3 [cd/m^2] will not be detected. Such ranges of luminance can however be considered as negligible for the aimed project applications.

g) Data acquisition and treatment procedures

The measurement of the simultaneous illuminance on the sample plane presents an incertitude of less than 1% in relative terms (as shown by the error bars of Fig. 3.29).
On the other hand, the polynomial approximation of the ratio given by the illuminance on the sample centre divided by the illuminance measured on the sample holder's edge fits the experimental data with a standard deviation of only 0.12%.
It must be noted that the cosine response quality of these sensors has been checked as well by verifying that the measured illuminance varied with the altitude angle θ_2 according to a cosine law. The relative deviations from this ideal model being of less than 1% in general, one can consider these illuminance-meters as of good accuracy.

These results show that no significant error can be attributed to the illuminance $E_1(\theta_1)$ measurement.

Certain approximations inherent to the data processing may induce an incertitude on the obtained BTDF values.
As a matter of fact, the different distances d and outgoing directions (θ_2, ψ_2) considered in equation (3-11) are average values, taking the gravity centre as a reference point.
This simplification induces a loss of quality in the measurement accuracy; a comparison of pixel per pixel evaluations for d and (θ_2, ψ_2) lead to a mean relative error of about 6% on the BTDF values when using average quantities. It is observed that these differences increase with the size of the concerned discretisation zones, influenced by a growing inaccuracy in the distance and direction determination by values corresponding to the gravity centre.

It has been verified that the approximation of the discretisation zones' area by the number of contained pixels was widely sufficient and that an exact calculation of the equivalent areas lead to no modification in the BTDF data.

h) *Global error on BTDF values*

The global error on the final data may be evaluated by considering every individual error on the different factors intervening in BTDF's expression. The relative error of an arbitrary function F defined by $F = X \cdot Y$ is indeed given by equation (3-21), the individual errors attributed to factors X and Y being known:

$$\frac{\Delta F}{F} = \sqrt{\left(\frac{\Delta X}{X}\right)^2 + \left(\frac{\Delta Y}{Y}\right)^2} \qquad (3\text{-}21)$$

Table 3.2 summarises the different error sources and their impact on the BTDF assessment.

Procedure	Error source	Relative error	Affected factor
Spectral calibration	Photometric error ε	4%	L_{screen}
Photometric calibration	Determination of relations between grey levels and associated luminance values	~1%	L_{screen}
Geometric calibration	Negligible	0%	-
Image uniformity and screen diffusion correction	Variation of repercussions of image non-uniformity and imperfect screen diffusion	2%	L_{screen}
Incident beam uniformity and collimation	Incertitude on correction factor of diameter	2%	D
Parasitic light	Negligible	0%	-
Data acquisition and treatment procedures	Consideration of a unique direction (θ_2, ϕ_2) and distance d whereas non punctual areas are concerned	6%	BTDF

Table 3.2. Error sources affecting the BTDF assessment.

In our case, there are two factors presenting significant relative errors and intervening in equation (3-11): the luminance L_{screen} whose incertitude is mainly due to spectral calibration (4%), photometric calibration (~1%), and mentioned correction factors (2%) on one hand; the illuminated area A, expressed by $A=\pi D^2/4$, where the diameter D is defined with a relative imprecision of 2% on the other hand.

We have therefore:

$$\frac{\Delta_a BTDF}{BTDF} \overset{(3-21)}{=} \sqrt{\left(\frac{\Delta L_{screen}}{L_{screen}}\right)^2 + \left(\frac{\Delta A}{A}\right)^2} \qquad (3\text{-}22)$$

$$\overset{(3-21)}{=} \sqrt{\left(0.04^2 + 0.01^2 + 0.02^2\right) + \left(0.02^2 + 0.02^2\right)} = 0.05$$

where index a indicates a relative error on the BTDF value due to individual factors.

The error due to the data treatment procedure (indexed b in equation (3-23)) and affecting the values of d and (θ_2, ϕ_2) in equation (3-11) were directly evaluated on the obtained BTDF values; it has thus to be added to the value indexed a in equation (3-22).

This leads to a global incertitude given by equation (3-23):

$$\frac{\Delta BTDF}{BTDF} = \frac{\Delta_a BTDF + \Delta_b BTDF}{BTDF} = 0.05 + 0.06 = 0.11 \qquad (3\text{-}23)$$

Therefore, a relative error of 11% can be assumed for the final BTDF values.

Comparison of hemispherical transmittances

The determination of the hemispherical light transmittance error cannot be based on equations (3-23) and (3-24), taking the incertitudes ascribed to each $BTDF_n$ value into account.
Effectively, the light transmittance error would then increase with the output resolution, which is opposite to its expected evolution: a decreasing step in outgoing directions should render the sum in (3-18) closer to the integral. It would moreover depend on the BTDF values, which is unacceptable.

$$\Delta T = \sqrt{\sum_{n=1}^{N_{out}} \Delta BTDF_n^{\,2}} \qquad (3\text{-}24)$$

A completely different method was therefore applied to estimate the hemispherical light transmittance error and to validate the BTDF measurements using another approach.

This method consists of a comparison of the hemispherical transmittance obtained through an integration of the different BTDF values achieved by the photogoniometer (equation (3-18)) with the hemispherical transmission measured by an Ulbricht integrating sphere for the same sample [Ayd99].
An Ulbricht sphere presents a perfectly diffusing white internal surface, on which the transmitted light reaches a high-quality homogeneity in luminance. The ratio between the internal illuminance measured by a photometer placed on the inner side of the sphere and the incident illuminance provides the value of the hemispherical light transmittance.

Comparisons with the calculated values of τ (through equation (3-18)) have been performed with three different samples: a lambertian diffuser (plexiglas), a laser cut panel and a 3M prismatic film.
Several measurements were performed with the photogoniometer, considering the same incident directions and azimuth planes C as for the integrating sphere analyses (a particular attention was given to keep the same orientation for the sample).

The values of $\tau(\theta_1, \phi_1)$, achieved for each incident direction and each sample, have been reported and compared to the results obtained by different laboratories equipped with an Ulbricht sphere and participating to Task 21 of the International Energy Agency (IEA) [Ayd99] :

- TUB (Technische Universität Berlin, D)
- BAL (Bartenbach Lichtlabor, A)
- ISE (Institut für Solare Energiesysteme, D)
- LESO (Laboratoire d'Energie Solaire et de Physique du Bâtiment / EPFL, CH).

Two examples of comparisons are shown in Fig. 3.35, for the prismatic film 3M and a Laser Cut Panel: they reveal discrepancies generally lower than 10% in relative terms, even with the quite extreme features in transmission associated to these samples.

The average error on the light transmittance values for a rather complex fenestration material is considered to be of about 20%.

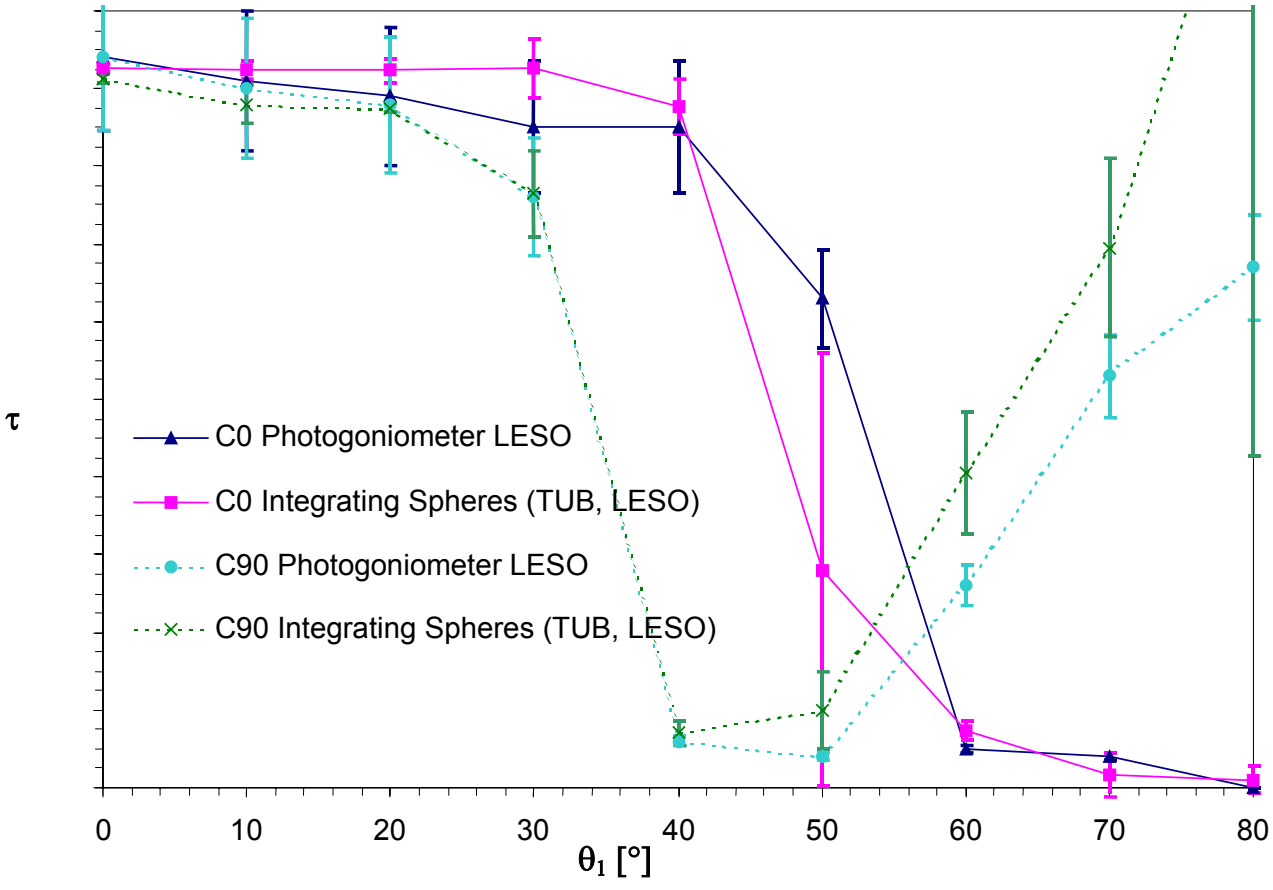

A

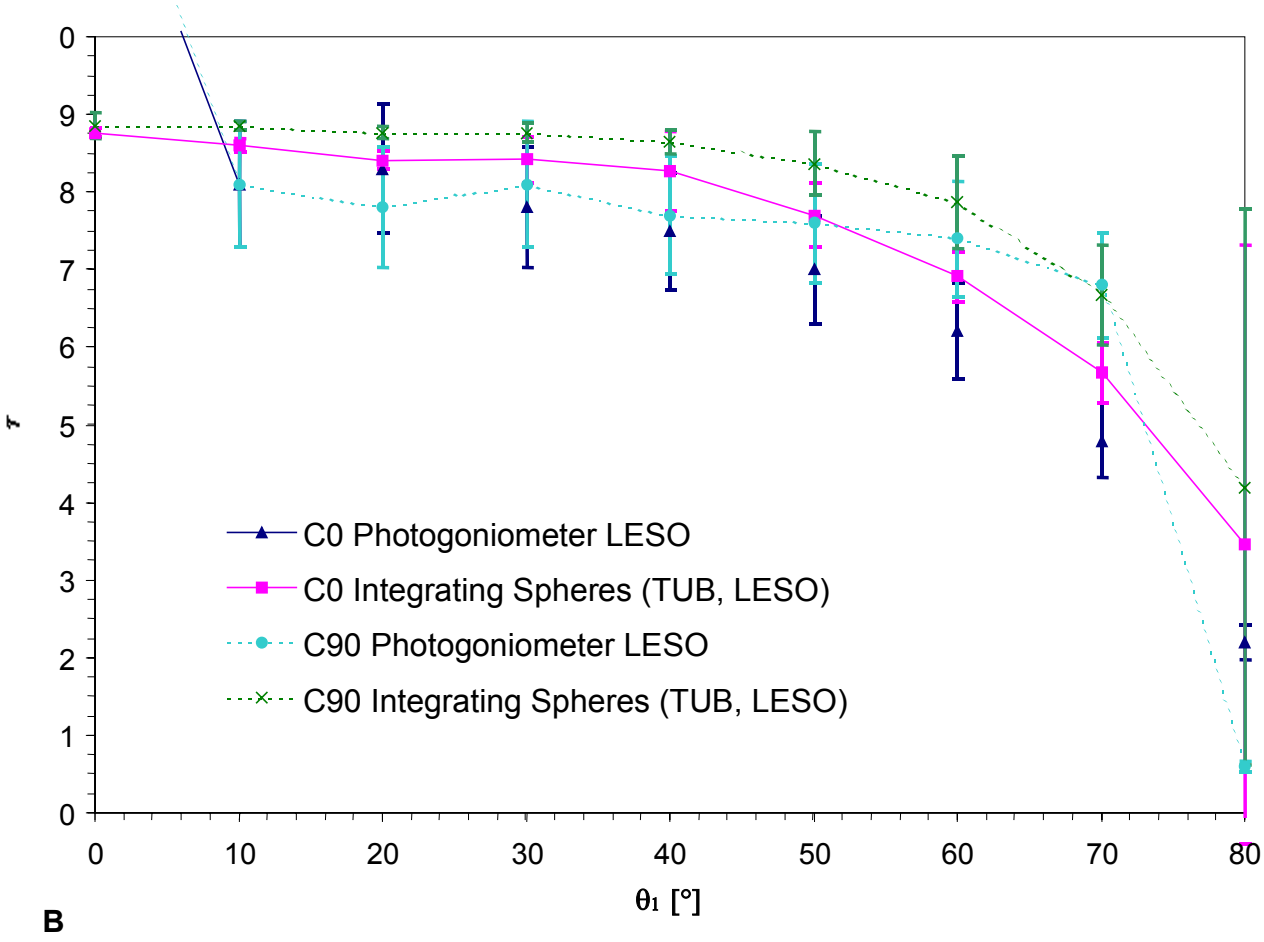

Fig. 3.35. Integrated light transmittance comparisons. The Integrating Spheres results are based on an average value obtained from measurements of the same samples in different laboratories; the standard deviation is given by the error bars. **A** Prismatic SOLF film (3M), with light incidence on prismatic side. **B** Laser Cut Panel.

3.4 VALORISATION OF DATA

3.4.1 Integral data set

Final electronic data

The achieved BTDF data set is saved in ASCII on an electronic file denominated after the sample name, and including the institute's designation and the considered incident direction (e.g. leso_SampleName_θ_1_ϕ_1.txt).

This file contains the following data:

- the sample characteristics: name, manufacturer, symmetry indicator, area, thickness, eventual comments, date of measurement, institute denomination
- the measurement parameters: incident direction (θ_1, ϕ_1), output angular resolution ($\Delta\theta_2$, $\Delta\phi_2$), limit altitude θ_{lim} (see § 3.2.4)
- the hemispherical light transmittance $\tau(\theta_1, \phi_1)$, calculated through equation (3-18) (see § 3.3.3)
- the BTDF values, expressed in [$cd.m^{-2}.lx^{-1}$], for each associated angular direction (θ_2, ϕ_2).

Details about the exact specifications of these final data files and about the conventions of orientation of the sample regarding the adopted spherical co-ordinate system are given in Annex B.

BTDF visualisation on the integral hemisphere

The six calibrated images created for the six screen positions are superposed to build up an integral image of the directional transmission represented in polar co-ordinates.

The achieved calibrated screen images, composed of L_{screen} / $E_1(\theta_1)$ ratios, corrected for the non-homogeneity and imperfect screen diffusion effects are already available (cf. Fig. 3.21).
The build-up of the integral hemispherical image still necessitates several corrections induced by distance and light tilting effects, accounted through equation (3-9). As they cannot be applied analytically as for the numerical data, equivalent operations have to be effectuated on the different images using digital treatments.

For that purpose, a correction Figure, made of pixel values equal to the compensation factor C_F given by equation (3-25), is created:

$$C_F = \frac{\pi}{\rho} \cdot \frac{d^2}{\cos\theta_2 \cdot \cos\alpha} \qquad (3\text{-}25)$$

Each element of equation (3-25) is independent of the screen position or the sample type, as can be seen from this expression.

The construction of such a correction figure requires the application of several arithmetic transformations on a 32 bits image, in order to account for the effect of the factor of equation (3-25) for each pixel.
Practically, these operations are led through mutliplications by a series of 32 bits images whose pixels are respectively equal to π, $1/\rho$, $d \cdot d$, $1/\cos\theta_2$, $1/\cos\alpha$. The corresponding images are created thanks to MATLAB® matrix calculations and handled with digital image operations tools, provided by IMAGE-PRO PLUS®.

The achieved correction figure is approximated by grey levels in Fig. 3.36. The dynamic range of these correction factors is by far too large to be adequately represented by grey levels (256 levels, from 0 to 255): with no obstruction, it varies from about 37'000 ((θ_2, ψ_2) = (Θ_0, 0°)) to $1.4 \cdot 10^{21}$ ((θ_2, ψ_2) = (90°, $\pm$30°)).

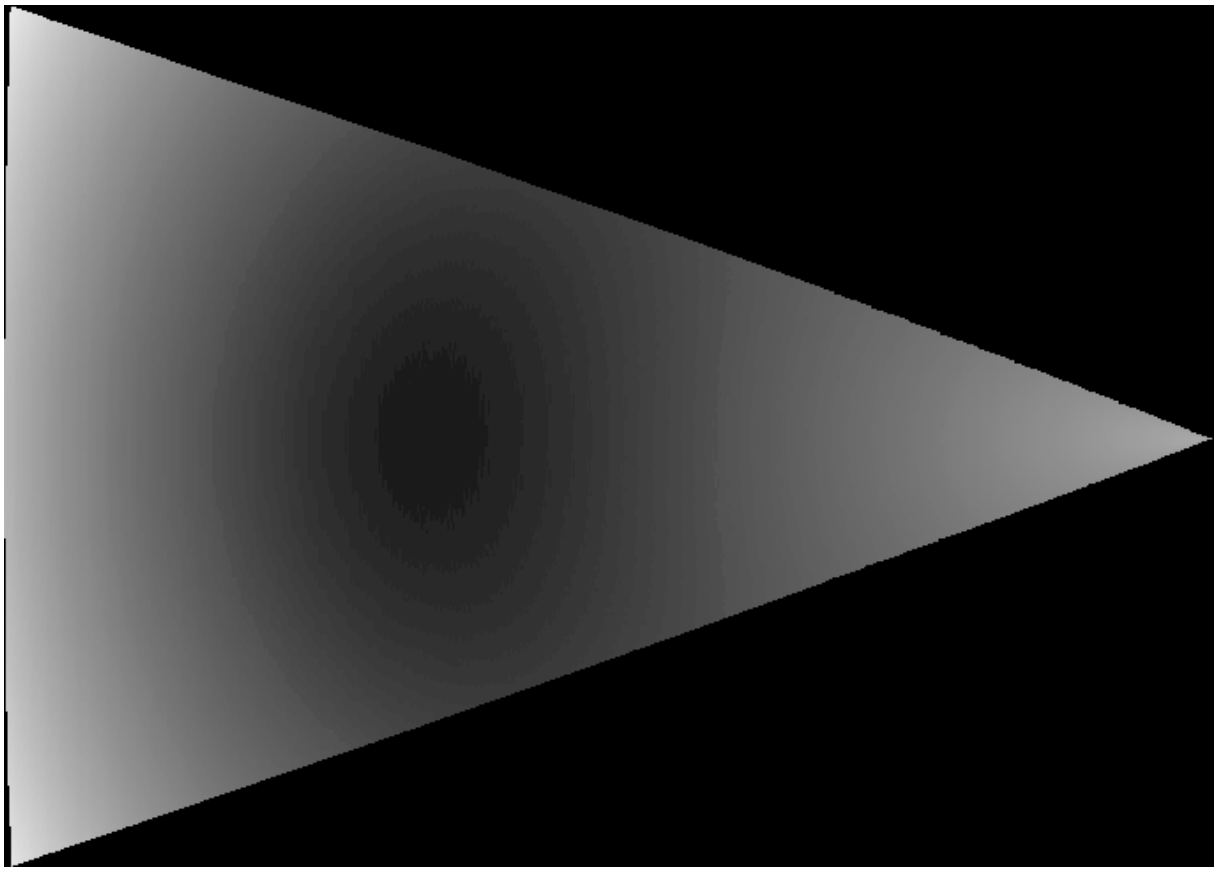

Fig. 3.36. Illustration of the correction factor, aiming to compensate distance and light tilting effects.

Each pixel on the achieved image is, in consequence, corrected according to its particular location.
Finally, a division by the sample area A leads to a picture representing the approximate BTDF values for each screen position.

These six final pictures, fully corrected and calibrated, are then resized (in order to produce equilateral triangles), rotated (according to the considered screen position) and appropriately positioned on an integral view.

These operations are illustrated by Fig. 3.37: a white screen is chosen to illustrate the applied procedures.

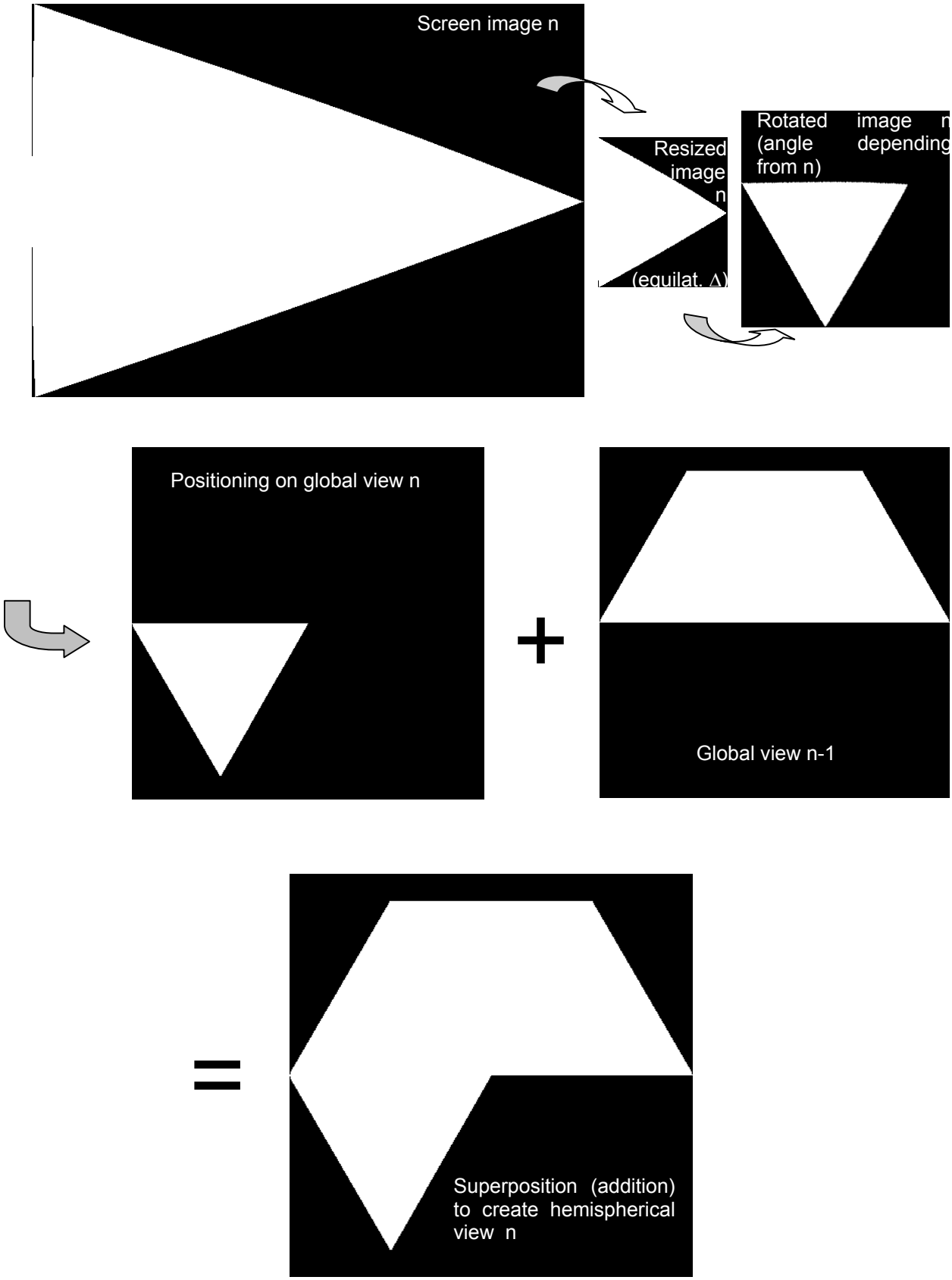

Fig. 3.37. Operations carried out on each screen image (n = 1 to 6) in order to produce a hemispherical view of the BTDF (n = 4 in this case). The screen image n is composed of 488x685 pixels; the final hemispherical image is smaller (reduction of required memory): its size is 400x400 pixels.

As a consequence of image construction, the final view is not exactly a visualisation of the “transmission hemisphere” projected on a horizontal plane; the angular corrections, required to build such a projection, have not been applied on the pictures, the orthogonal projection being too heavy for the image handling procedures.

Nevertheless, the obtained images offer direct information about the directional transmission of the analysed sample. The possibility to observe some details about transmission features, that could have been rendered invisible because they were averaged inside the different discretisation zones, can be obtained that way.

Two examples of hemispherical visualisations are shown in Fig. 3.38 for a 3M prismatic film under an incidence of (40°, 0°) and for a pleated tissue blind (type “PLISSEE 3141”, see Annex C), manufactured by Baumann-Hüppe AG and characterised under normal incidence. In order to figure out what kind of angles the transmission features observed on the image correspond to, a polar grid is drawn to approximately show the values of θ_2 and ϕ_2, with 10° and 15° steps respectively.

It may be noted that the output angular resolutions for these two products are different : it is equal to (5°, 5°) for the prismatic film and to (10°, 15°) for the solar blind.
These dissimilarities of course do not affect the characteristics of the hemispherical image; they will however have implications on the graphical representations, as explained in § 3.4.2.

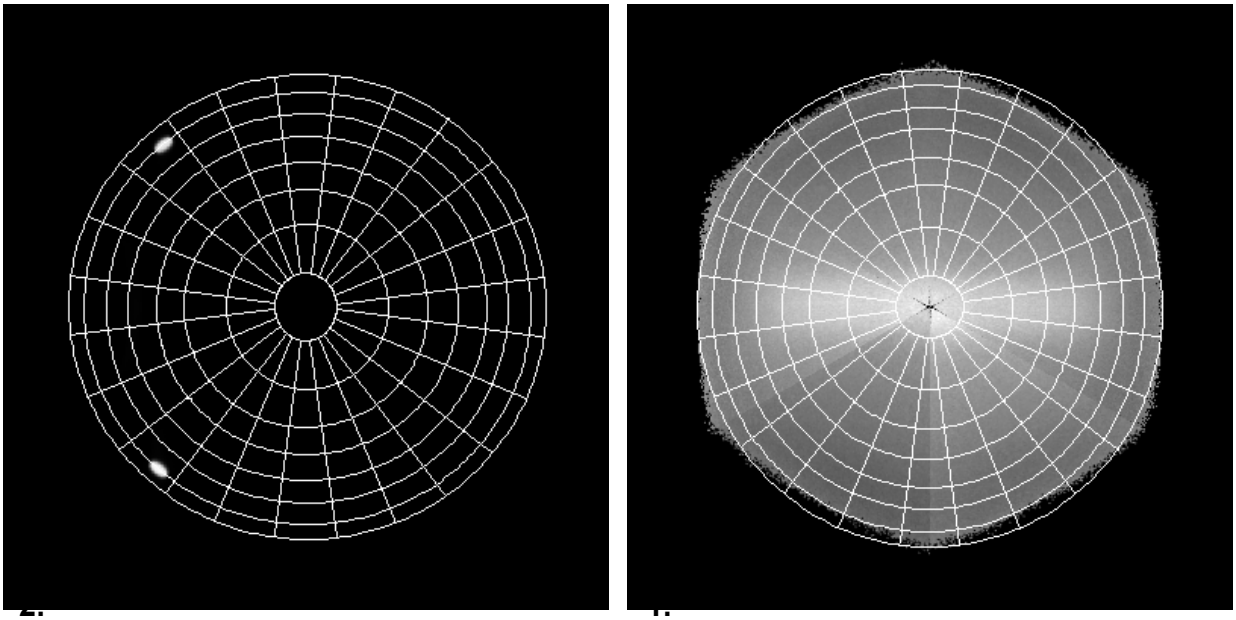

Fig. 3.38. BTDF hemispherical view. **A** Prismatic SOLF film (3M) : light incidence on prismatic side; (θ_1, ϕ_1) =(40°, 0°) ; ∅ = 10cm; ($\Delta\theta_2$, $\Delta\phi_2$) = (5°, 5°). **B** Pleated tissue blind (Baumann-Hüppe AG) : (θ_1, ϕ_1) =(0°, 0°) ; ∅ = 17cm; ($\Delta\theta_2$, $\Delta\phi_2$) = (10°, 15°).

3.4.2 Representation of photometric solids

The set of BTDF numerical data is very large and does not offer a synthetic view of the sample's transmission features. Graphical processing is therefore necessary to provide a reasonable appreciation of the light transmission behaviour. The data are treated for this purpose by MATLAB® to create three dimensional graphical representations of BTDFs; different visualisation possibilities of the transmission features are shown in Fig. 3.39, 3.40 and 3.41 for the prismatic film and the tissue blind presented above under the same incident directions.

Hemispherical projection

The projection of the transmission features on a full hemisphere follows the principle exposed in § 3.3.3. and illustrated in Fig. 3.34: each BTDF value, measured inside a given angular discretisation zone, is represented by the corresponding patch standing out against the hemisphere vault. The colour scale, reproducing the BTDF dynamic range for a given incident direction, allows to visualise the numerical BTDF values. The point of view under which the hemisphere is seen can be freely chosen by simple mouse-dragging and clicking. Fig. 3.39 illustrates this projection for the two previously mentioned products.

This representation leads to a clear understanding of the angular distribution of the transmitted light flux. The values of θ_2 and ϕ_2 can indeed be easily read on this projection.
It must be mentioned that the hemispherical projection is very similar to the visualisation offered by the integral calibrated image (Fig. 3.38), when the viewing direction is vertical. These two representations complement each other:

- the recomposed image provides details about finer transmission features than the output resolution can render
- the hemispherical projection offers a possibility of quantitative evaluation of BTDF and a more precise angular and spatial management.

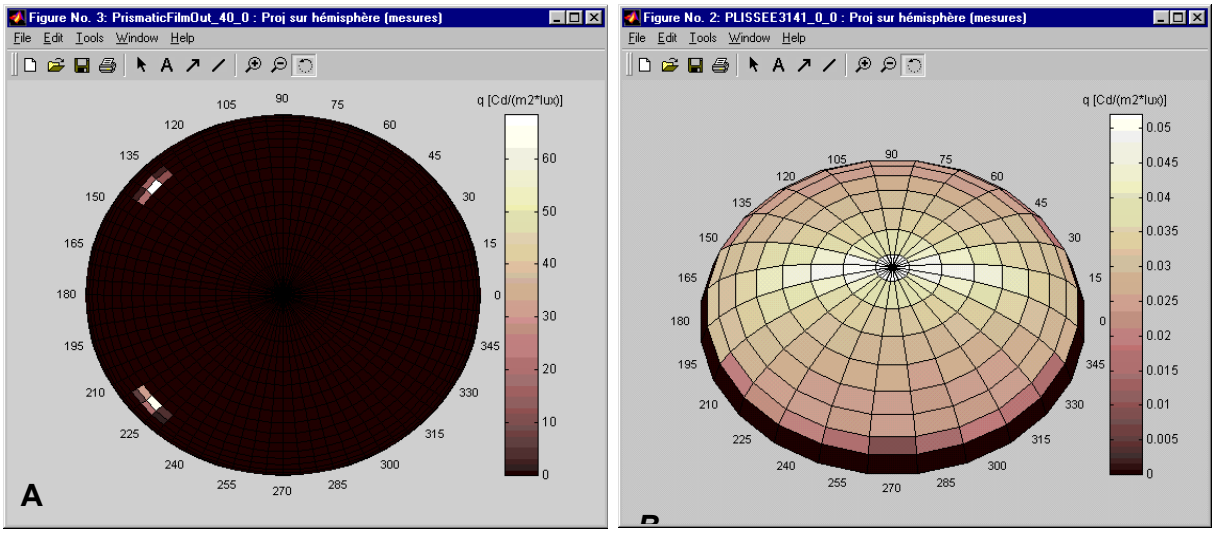

Fig. 3.39. Hemispherical projections **A** Prismatic SOLF film (3M) : light incidence on prismatic side; (θ_1, ϕ_1) =(40°, 0°) ; ∅ = 10cm; ($\Delta\theta_2$, $\Delta\phi_2$) = (5°, 5°). **B** Pleated textile solar blind (Baumann-Hüppe AG) : (θ_1, ϕ_1) =(0°, 0°) ; ∅ = 17cm; ($\Delta\theta_2$, $\Delta\phi_2$) = (10°, 15°).

Photometric solid

The photometric solid can be defined as a three-dimensional representation of the luminous intensity characteristics, commonly given for artificial lighting fixtures. These solids are also represented by section views of the spatial intensity distribution; such section views can be used for BTDF measurements as well, as explained below.
It can be noted that the main difference between artificial and natural light analyses, apart from distinct measured quantities, is that the incident direction of the impinging light flux is of course not considered for artificial lighting, which reduces the number of transmission functions to a unique distribution.

The creation of photometric solids requires to build a grid based on a spherical referential, where each point is represented by a triplet ($BTDF_{val}$, θ_2, ϕ_2), $BTDF_{val}$ being the numerical value of BTDF(θ_1, ϕ_1, θ_2, ϕ_2), used as the radial distance.

In order to visualise the situation more convivially, the incident direction is represented in the opposite hemisphere as well, through its angular direction (θ_1, ϕ_1); a grid representing the polar co-ordinates (θ_2, ϕ_2) (or more exactly (θ'_2, ϕ_2), see Annex B) is projected on a horizontal plane to clarify the three-dimensional perception of the photometric solid and to allow a direct spatial localisation of particular transmission features (especially when choosing a vertical direction of view).

The point of view is freely chosen, which allows observation of every characteristic on the transmission distribution function.
The colour scale is proportional to the BTDF range for a given incident direction. This leads to a double-check possibility of the BTDF values, through the growing radial distance on one hand, and through a brightening of the associated colour on the other hand, for increasing BTDF values.
Two photometric solids are given in Fig. 3.40.

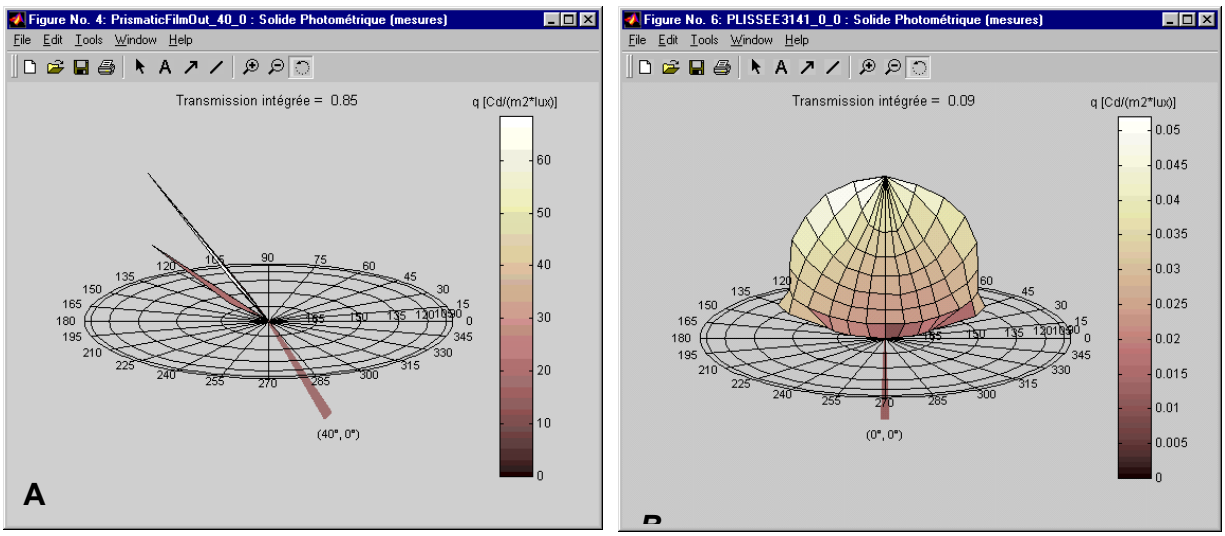

Fig. 3.40. Photometric solids **A** Prismatic SOLF film (3M) : light incidence on prismatic side; (θ_1, ϕ_1) =(40°, 0°) ; ∅ = 10cm; ($\Delta\theta_2$, $\Delta\phi_2$) = (5°, 5°). **B** Pleated textile solar blind (Baumann-Hüppe AG) : (θ_1, ϕ_1) =(0°, 0°) ; ∅ = 17cm; ($\Delta\theta_2$, $\Delta\phi_2$) = (10°, 15°).

This graphical representation therefore gives a synthetic and intuitive idea of the angular distribution of the transmitted light: peaks in transmission will for instance appear like sharp emerging zones, whereas a diffuse transmission will produce a “smooth solid”, that looks like a hemisphere and presents only small colour differences.
This clear-sighted visualisation of the material’s transmission features allow a good understanding of its photometric performances as a fenestration material.

On the examples illustrated by Fig. 3.40, one can easily observe:

- a splitting of the incident beam into two distinct outgoing directions for the prismatic film, which do not correspond to the extension of the incident direction
- a privileged direction for transmission along the vertical plane C0-C180 (see Fig. 3.43), induced by the pleats of the tissue blind, as well as a rather diffuse transmittance for the other directions.

Section views

The third possible representation consists of several section views of the previously described photometric solid, along vertical planes (C planes perpendicular to the sample plane). It has been chosen to give a planar curve of each 15° azimuth plane(C0, C15, C30, C45, C60, C75, C90, C105, C120, C135, C150, C165). These curves are therefore similar to the luminous intensity distributions found in artificial lighting catalogues, as mentioned before (these catalogues in general only provide one or two sections).
Each curve is showed on a polar co-ordinates grid, giving the azimuth value of the section planes associated, the BTDF scale and the altitude angles θ'_2. The polar angle θ'_2 is defined as the supplementary angle of θ_2 as illustrated in Fig. B.1(Annex B) in order to distinguish transmission (BTDF) from reflection (BRDF) measurements (θ'_2 is simply equal to (180° - θ_2)).

Fig. 3.41 gives section views of the BTDF distribution for the prismatic film and the solar blind. This representation yields a clear quantitative analysis of the BTDF behaviour, by providing “easy-to-read” and accurate numerical data.

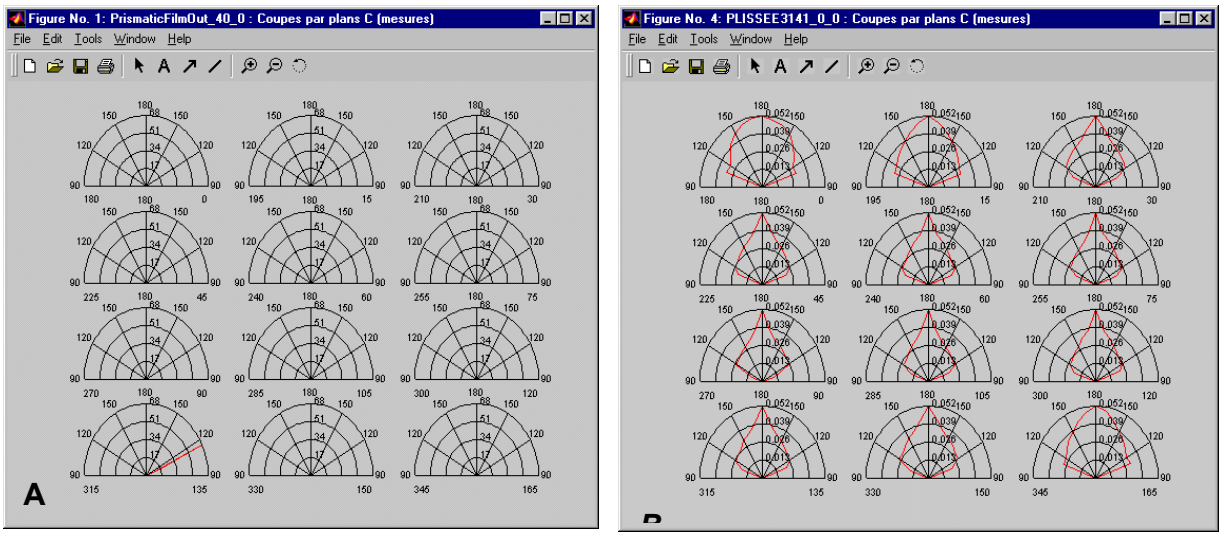

Fig. 3.41. Section views along C planes **A** Prismatic SOLF film (3M) : light incidence on prismatic side; (θ_1, ϕ_1) =(40°, 0°) ; ∅ = 10cm; ($\Delta\theta_2$, $\Delta\phi_2$) = (5°, 5°). **B** Pleated textile solar blind (Baumann-Hüppe AG) : (θ_1, ϕ_1) =(0°, 0°) ; ∅ = 17cm; ($\Delta\theta_2$, $\Delta\phi_2$) = (10°, 15°).

3.4.3 Application case studies

In order to have an idea of the potentialities offered by the BTDF data sets and their graphical processing, application case studies are given in this chapter.

Two venetian blinds have been chosen for that purpose:

- a conventional white lamellae (Fig. 3.42A)
- an optimised solar blind, called “Shine”, presenting a pearl grey quartz coating similar to the painting used in car body manufacturing and of particular shape (section similar to the spoon profile, see Fig. 3.42B).

Both blinds are manufactured by Baumann-Hüppe AG, our industrial partner for this project, and their photometric characteristics have been measured by the formerly described photogoniometer.

In order to be able to compare their performances, the samples have been set with the same inclinations of lamellae (30° with regard to the window plane) and equal dimensions of slats (profile: 10 cm, length: 34 cm, distance between slats: 8 cm).

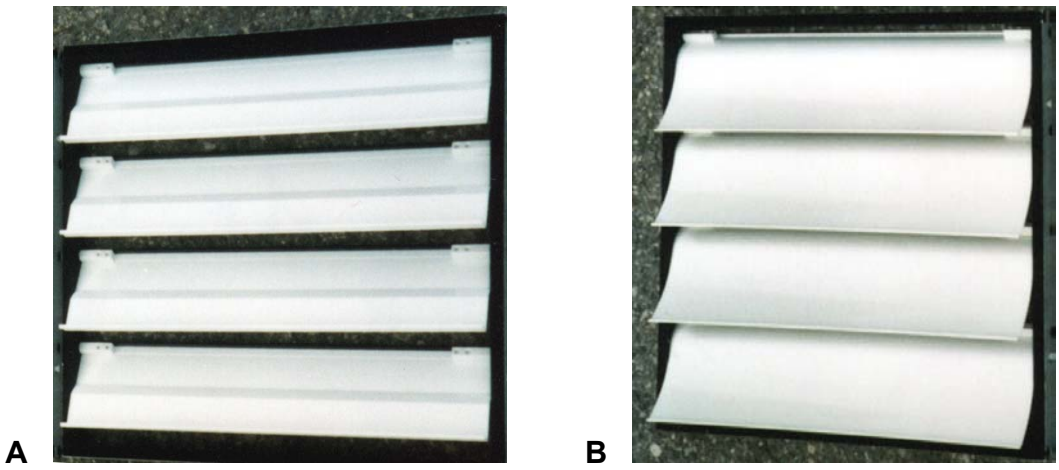

Fig. 3.42. Pictures of analysed venetian blinds. A Conventional white lamellae. B Optimised prototype “Shine”, with pearl grey quartz coating and particular shape of slats.

BTDF measurements have been performed with a 17 cm diameter diaphragm and under different incident directions. These directions present :

- a step in incident altitude $\Delta\theta_1 = 30°$
- a step in incident azimuth $\Delta\phi_1 = 90°$

If the altitude θ_1 is null, it does not make sense to perform measurements with more than one azimuth value ϕ_1, therefore taken arbitrarily equal to zero as well.
Moreover, the symmetries being taken into account, analysing the transmission under incidences of both azimuths $\phi_1 = 0°$ and $\phi_1 = 180°$ with the same altitude θ_1 is not useful. Therefore, as can be seen in Fig. 3.43, incidences along the C180 plane were not considered.

This leads to a set of seven distinct incident directions given by the following couples (θ_1, ϕ_1) illustrated in Fig. 3.43: (0°, 0°), (30°, 0°), (60°, 0°), (30°, 90°), (60°, 90°), (30°, 270°), (60°, 270°).

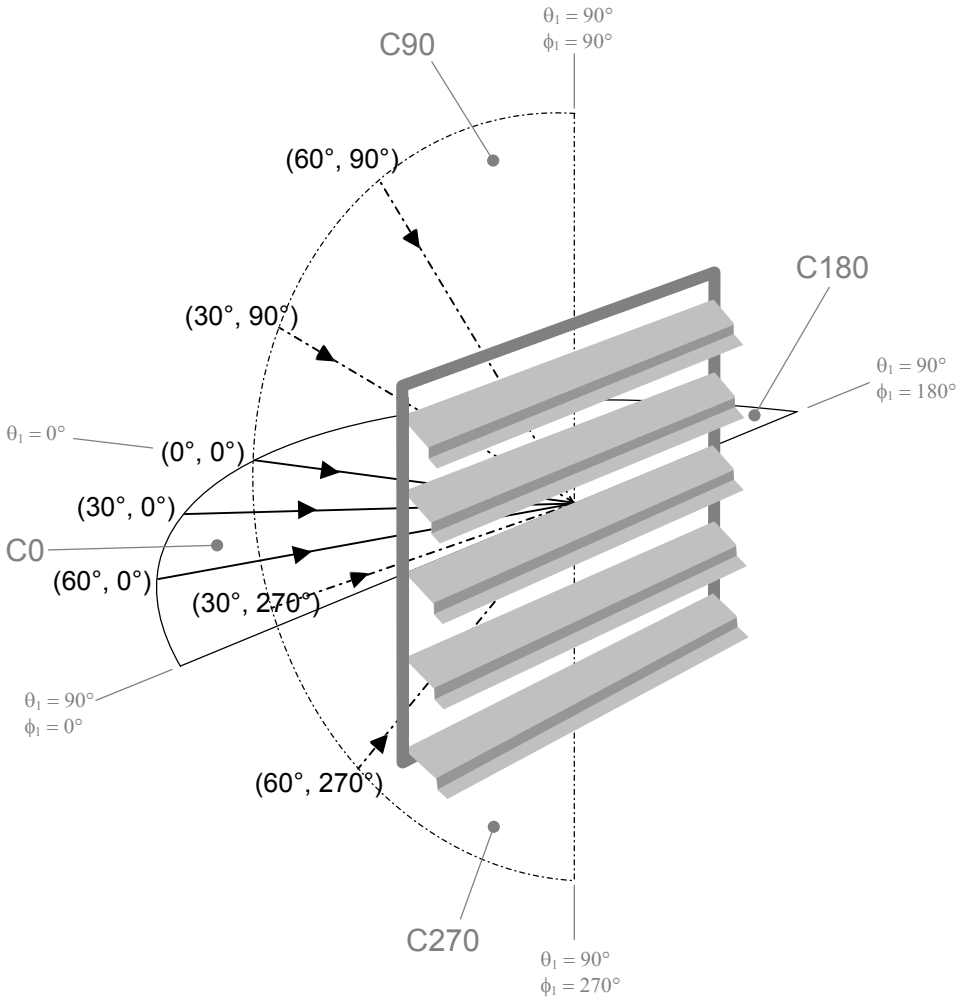

Fig. 3.43. Representation of incident directions considered for the characterisation of the solar blinds.

For each incident direction, one BTDF data set is assessed, providing the transmission features of the considered sample under this particular light incidence configuration. These incidences have to be considered along the possible incoming sunlight directions, in order to have practical applications.
It can be mentioned that the sun never appears in the low “incidence hemisphere” part ($180° < \phi_1 < 360°$); this part nevertheless must be considered in order to figure out the sample’s behaviour when rotated upside down (or in a minor way to predict the effect of external reflections on the ground).

The BTDF data can be used to analyse the sample’s adequacy for the visual comfort conditions, for instance by comparing the measured values with the reference ranges accounting for glare effects or high luminance contrasts. An example of analyse aiming at this kind of objective is presented below.

The graphical representation of photometric solids is useful to get a synthetic idea and an intuitive approach of the transmission from a global point of view (diffuse, specular, etc.) and to pick out its particularities (specular component whereas globally diffusing, apparition of transmission peaks or troughs, etc.).
Some of the different graphical representations are given for the two types of solar blinds in the next paragraph (Fig. 3.44 to 3.51).

Analysis using graphical representations

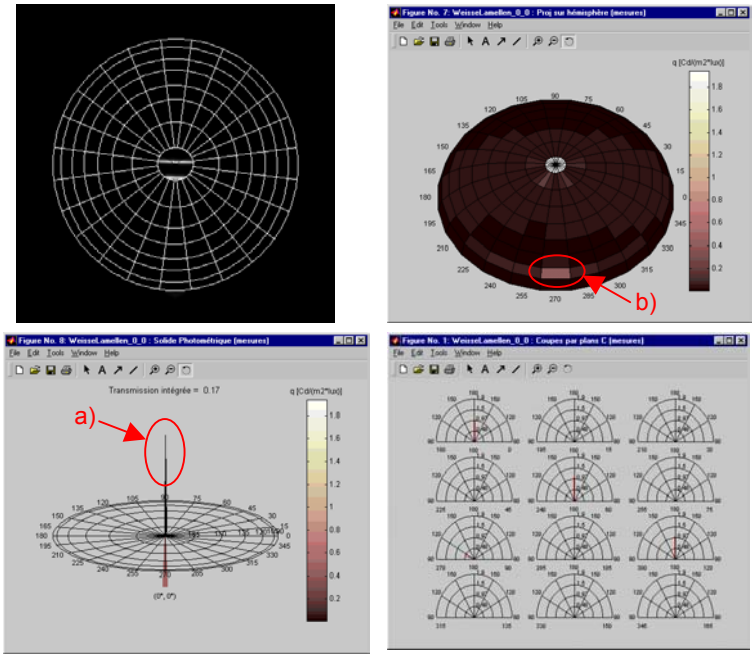

Fig. 3.44. White slats. Graphical representation of BTDF data under incidence (θ_1, ϕ_1) = (0°, 0°).

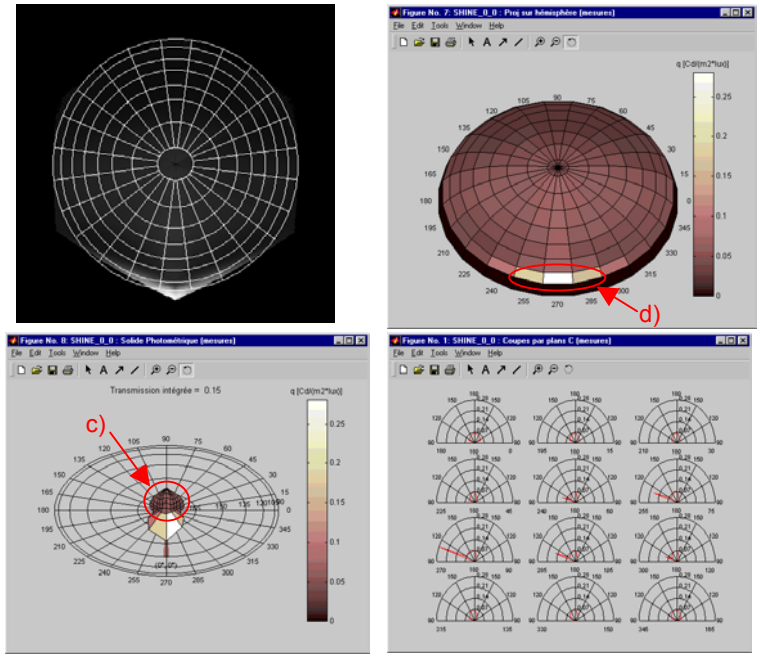

Fig. 3.45. Shine. Graphical representation of BTDF data under incidence (θ_1, ϕ_1) = (0°, 0°).

The observation of Fig. 3.44 and 3.45 shows important dissimilarities between the transmission features of the conventional white blind and the “Shine” prototype under normal incidence (i.e. θ_1 = 0°, cf. Fig. 3.43).
The first one mainly presents a regular transmission through the slats (peak along the incident direction, pointed out by a)), with a small effect of reflection on the coating, leading to a little increase of BTDF values in direction (θ_2, ϕ_2) = (60°, 270°), pointed out on the hemispherical projection by b).

The second one shows no direct component and presents a quasi diffuse transmittance (with only a slight deformation of the photometric solid in favour of normal transmittance, see c)), except along a particular direction, which shows an important deviation of light due to reflection on the slats (pointed out by d)). This effect leads however to BTDF extrema seven times lower than the light peak with conventional slats, showing a diffuse redistribution that could be beneficial to reduce glare risks under clear sky.

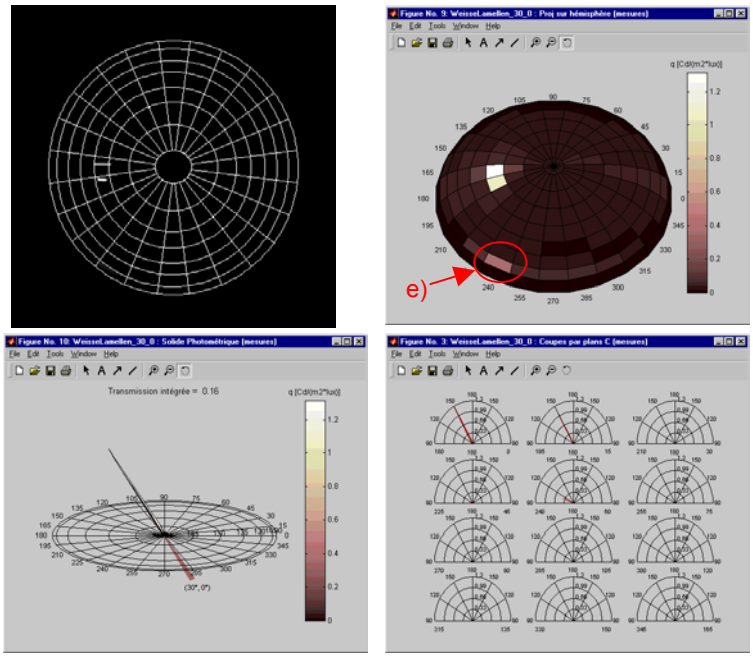

Fig. 3.46. White slats. Graphical representation of BTDF data under incidence (θ_1, ϕ_1) = (30°, 0°).

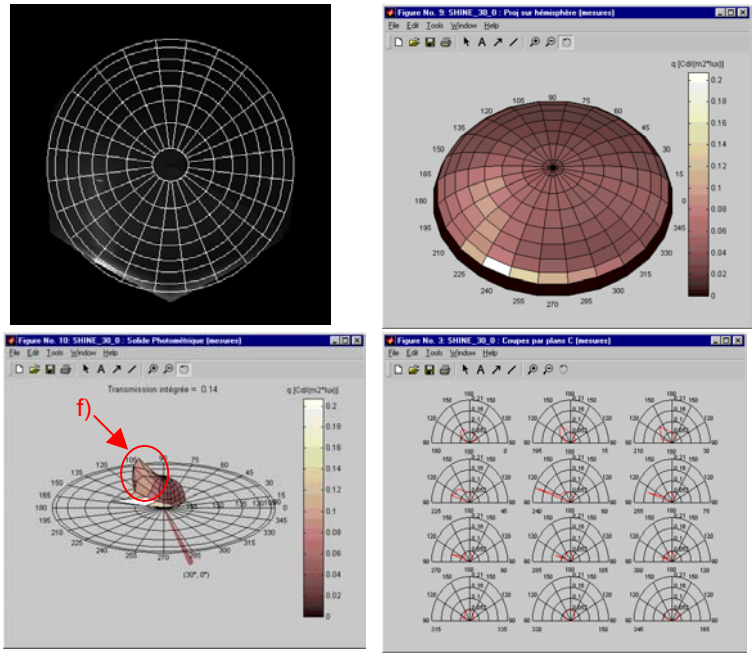

Fig. 3.47. Shine. Graphical representation of BTDF data under incidence (θ_1, ϕ_1) = (30°, 0°).

The same features appear for larger incidence angles θ_1 (Fig. 3.46 and 3.47): one can observe a regular transmission for the white slats, with small effects of reflection, displaced towards lower azimuth values (clockwise on the projections, see e)). For the

“Shine” prototype, the light transmission is quite diffuse, yet with a clearer deformation along the direct transmission direction (see f)); this direction indeed gets closer to the reflected direction, which generates a superposition of effects.

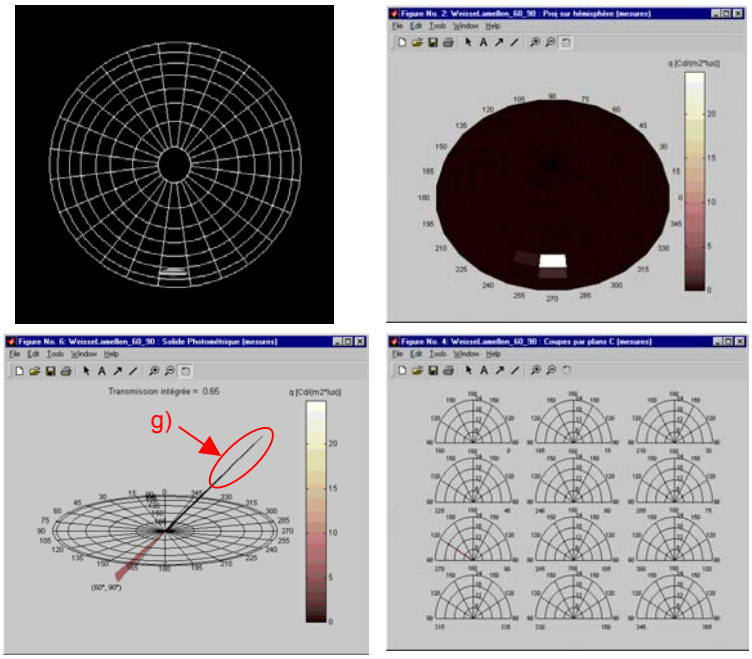

Fig. 3.48. White slats. Graphical representation of BTDF data under incidence (θ_1, ϕ_1) = (60°, 90°).

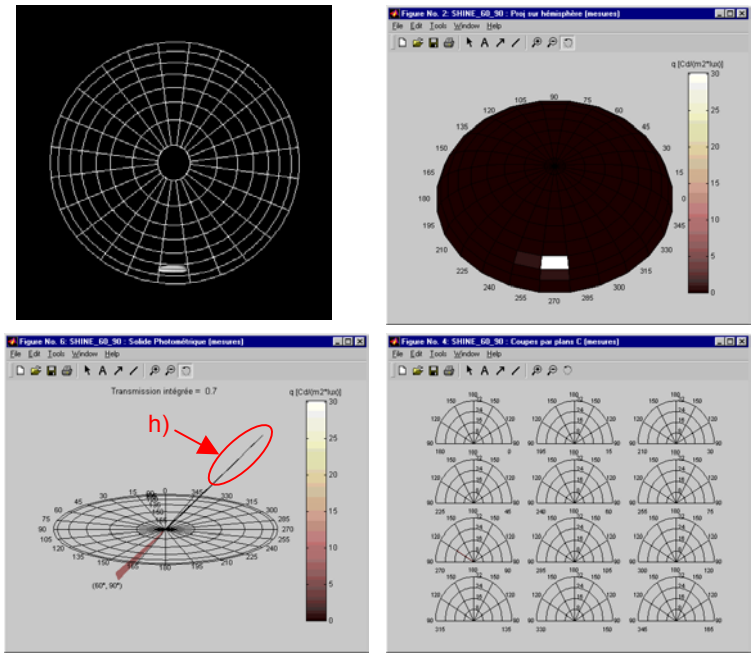

Fig. 3.49. Shine. Graphical representation of BTDF data under incidence (θ_1, ϕ_1) = (60°, 90°).

For other angular incidences along the azimuthal plane C90 (i.e. ϕ_1 = 90°, cf. Fig. 3.43), the incoming light flux is almost not deviated, when passing through the blind types (see g) and h)). Fig. 3.48 and 3.49 effectively show that both blinds present almost the same regular transmitted components, and even similar BTDF ranges. These kinds of incidences therefore show no improvement of performances for the optimised blind.

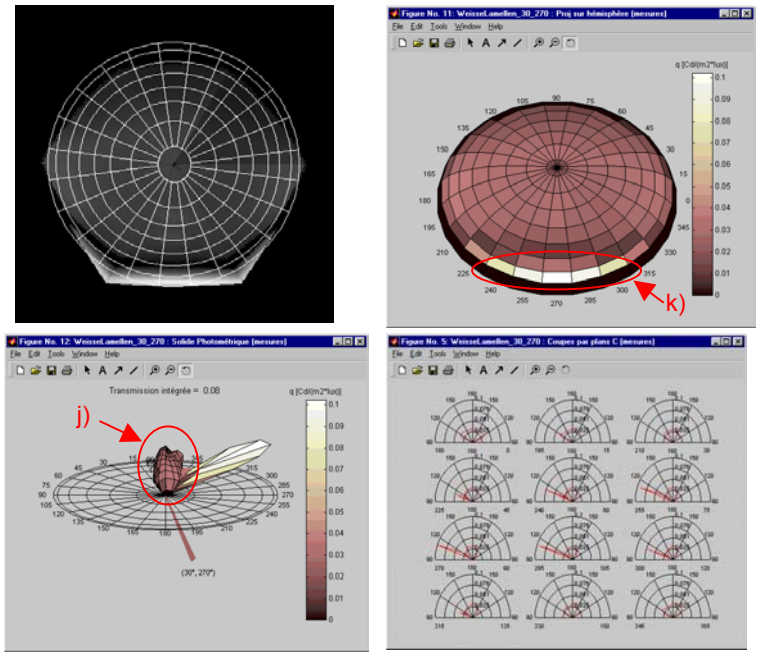

Fig. 3.50. White slats. Graphical representation of BTDF data under incidence (θ_1, ϕ_1) = (30°, 270°).

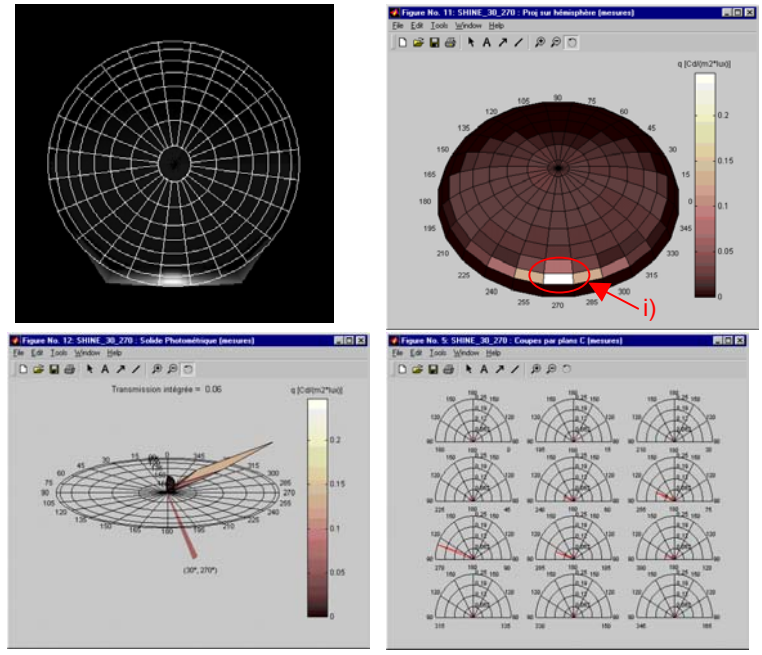

Fig. 3.51. Shine. Graphical representation of BTDF data under incidence (θ_1, ϕ_1) = (30°, 270°).

Finally, along the azimuthal plane C270 (i.e. ϕ_1 = 270°, see Fig. 3.43), the transmission features of both blinds are quite similar as well: the major part of the incoming light is reflected on the slats and redirected along a coplanar direction (transmission peaks around ϕ_2 = 270°, cf. i)); a minor part is slightly diffused, more significantly for the white slats (see j)), which also presents a more extended region for the reflection peak (cf. k)).

The analysis of these figures leads to a good understanding of the transmission features of the two products. It allows pointing out the positive, as well as the restricting

characteristics of the samples and leads to an improvement of their performances through a modification of their shapes and/or their reflection coefficients.
It can be deduced for instance that the “Shine” prototype, placed upside down with regard to the initial orientation, can take advantage of its diffusing properties to reduce glare risks. Moreover, its significant reflecting properties, even under incidences along the horizontal plane C0, can be used to illuminate the ceiling, which therefore becomes a secondary natural light source.

More specific conclusions concerning the slats shape or coating necessitate a detailed examination of the BTDF graphical representations combined with the analysis of the numerical data.
To achieve a true prototype’s optimisation, the BTDF data based improvements of the samples should be submitted to new measurements in order to assess the reached performances, and to estimate whether they are acceptable or still perfectible.

An example of using BTDF numerical values, in order to evaluate the visual comfort performances of the two analysed solar blinds, is presented in the next paragraph.

Analysis using BTDF numerical values

The purpose of this analysis is to illustrate the use of BTDF data sets with a view to revealing problems or advantages of fenestration systems with regard to visual comfort and VDT screens (BAP, Bildschirmarbeitsplatz).
The BTDF data sets considered in this study, are based on the measurements achieved on the two formerly described solar blinds.

As prescribed by the lighting recommendations, a situation is considered as comfortable for the human eye if the luminance contrasts do not exceed the ratio 1:3 in the ergorama, limited by 30° of angular opening, and 1:10 in the panorama [OFQC94], limited by 60° of angular opening (see Fig. 3.52).

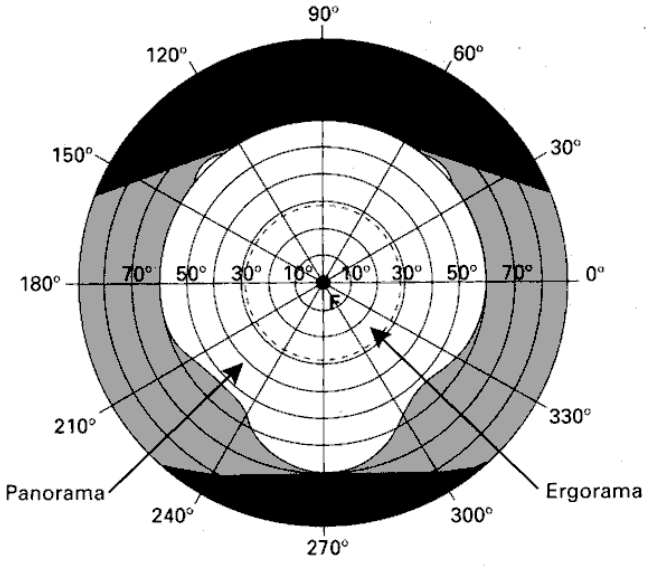

Fig. 3.52. Human field of vision [IES84]. White : field simultaneously seen by both eyes. Grey : Field seen by one eye. F: central field (fovea).

On the basis of the BTDF data set of a given fenestration system, it is possible to deduce whether the observed luminances will induce glare effects or not, and whether daylight will be sufficient for the kind of work considered.

Indeed, the BTDF is defined as the ratio of the transmitted luminance in a certain direction and the incident illuminance on the sample plane (see § 2.1).
Therefore, the luminances produced through a given blind in each direction can be directly deduced from the BTDF values associated to these directions, assuming that the illuminance E_1 of equation (3-26) is known:

$$L_2(\theta_1,\phi_1,\theta_1,\phi_1) = BTDF(\theta_1,\phi_1,\theta_1,\phi_1)\cdot E_1(\theta_1) \qquad (3\text{-}26)$$

A possible value for E_1 can for instance be the illuminance on a vertical plane measured under clear sky for a particular sun position, when studying frontal openings. It may be noticed that equation (3-26) is simply another way to write equation (2-2).

Let us consider the situation of a working place located nearby a window on which a solar blind is installed, and oriented perpendicularly to the wall. This situation is illustrated by Fig. 3.53.

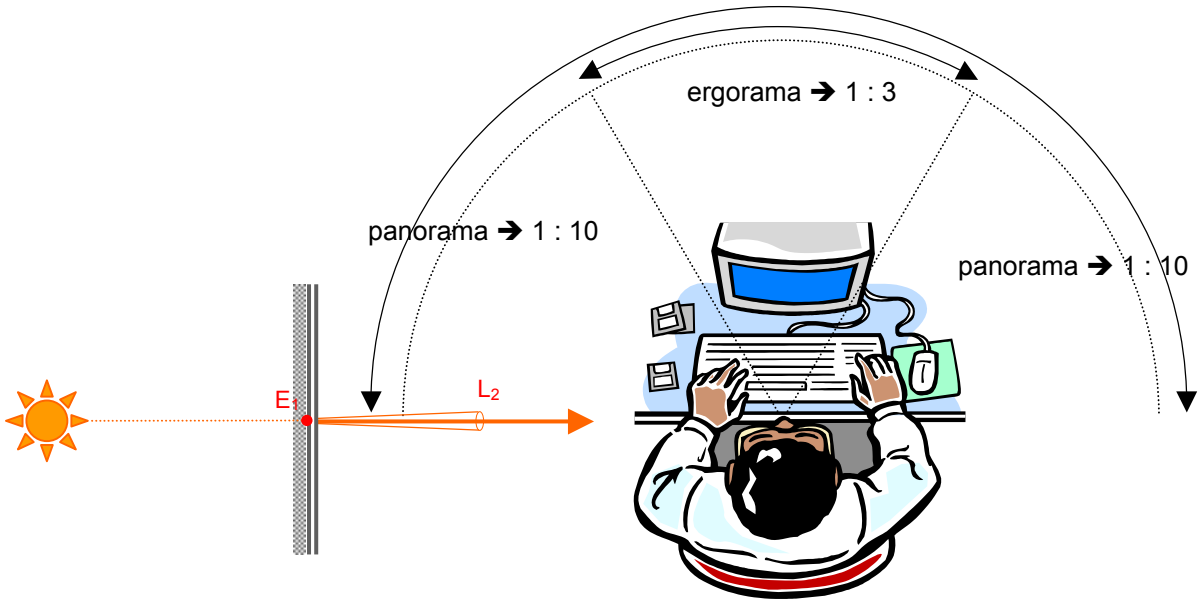

Fig. 3.53. Vertical view of a working place situated nearby a frontal window, with the subdivision of the field of vision into ergorama and panorama, together with the acceptable luminance contrasts associated. The panorama is extended for sake of simplicity to a 180° opening angle

The application of the known BTDF values to the study of a given situation requires the estimation of the outgoing direction (θ_2, ϕ_2), which could produce glare effects for the worker, defined for instance as the window centre to eye direction.
In the fictive case studied here, we consider the window centre as of same elevation as the worker's eyes. This consideration implies that the BTDF values to be examined are the measurements associated to the outgoing angular couple (θ_2, ϕ_2) = (0°, 0°) for the

different analysed data sets (see Fig. 3.53). A generalisation of the method to any couple (θ_2, ϕ_2) is however possible and will allow accounting for real situations as well.
To account for the reduction of the daylight flux by the glazing situated behind the blinds, the corresponding BTDF values are multiplied by the normal transmission of the glazing, which is equal to 0.85 for a double glazing[1].

It must however be mentioned that the consideration of a unique window centre to eye direction is far too restrictive in a real practical application case : as the window cannot be approximated by a point with regard to its distance to the worker, one should take the whole window surface into account, by considering different points on the window together with the emerging light distributions and the associated relations to the worker's eyes.
It can be noted that such thorough analyses are easier when using the information provided by the graphical representations : they effectively allow to build a definite set of situations susceptible to be problematic and to be examined numerically.

In order to be able to directly apply the BTDF data sets, we have chosen to consider the direction (θ_1, ϕ_1) = (0°, 0°), as a simple example of sunlight incidence (cf. Fig. 3.53), even if not really representative of a possible sun course position. This allows to reduce this case study to a single lamellae orientation, as the latter does not affect the transmitted light distribution in a normal incidence situation; other sun positions can be considered as well using the available (θ_1, ϕ_1) incidence angles.

Finally, a value for the illuminance E_1 was chosen : 40'000 lux appears to be a reasonable value, representative of clear sky conditions.

Table 3.3 resumes the numerical data necessary to analyse the situation adequately :

	Incident direction		**Transmitted direction**		**BTDF [cd·m^{-2}·lux^{-1}]**		**E_1[lux]**	**L_2 [cd·m^{-2}]**
	θ_1 [°]	*ϕ_1 [°]*	*θ_2 [°]*	*ϕ_2 [°]*	*100%$_{transm}$*	*85%$_{transm}$*		
White slats	0	0	0	0	1.937	1.646	40'000	65'858
Shine	0	0	0	0	0.070	0.060	40'000	2'380

Table 3.3. Numerical data necessary to assess glare risks for two different blinds (L_2 is determined accounting for the effect of double-glazing).

The luminance produced by a computer screen is in general comprised between 100 and 200 [cd·m^{-2}].
As explained above, a luminance contrast lower than 10 must be reached inside the vision field designated as panorama, to achieve visual comfort. Therefore, one can deduce that emerging luminances superior to 2'000 [cd·m^{-2}] will probably produce glare effects for the worker.

In our case study, one immediately deduces from the L_2 values of Table 3.3 that the « Shine » prototype will induce a far more comfortable situation than the conventional

[1] If we consider that 0.96% of the light is transmitted at each air-glass interface, we obtain a general transmission of 0.96^4 = 0.85% for a double-glazing element, if neglecting the absorption due to dust or veil for instance.

white slats, which without any doubt will induce glare, due to the importance of the direct transmission of daylight under normal incidence (see Fig. 3.44).
We also know from the graphical representations presented in Fig. 3.45, 3.47 and 3.51 that the major part of a beam reaching the « Shine » prototype under incidences lying out from the C90 plane (see Fig. 3.43) is transmitted along a grazing direction (θ_2 = 70° : reflection on the slats), which shows that glare will probably not occur at a reasonable distance from the window, even if we take the aperture surface as a whole.

These kinds of considerations point out the complementarity and usefulness of both information forms (graphical and numerical) and give an example of utilising the knowledge provided by the photometric solids in order to elaborate an efficient comparison of given situations.

The purpose of this rudimentary study is only to show a possible method to practically extract information from the BTDF data sets. Of course, supplementary measurements and analyses are however necessary to assess a reliable expertise of the photometric characteristics of a sample and in particular of its glare potentialities :

- multiple incident directions (θ_1, ϕ_1) and emerging directions (θ_2, ϕ_2) are to be considered
- different sample orientations and slats inclinations can be taken into account
- several positions for the worker and the window must as well be examined in order to provide a complete and reliable description of the transmission features of the analysed sample.

BTDF data moreover offer the possibility to estimate whether the daylight transmitted through a given fenestration system will be appropriate for a given task (work on a VDT screen, paper work, precise manipulations, etc.).
Indeed, with a complete description of the situation, including the geometric (room dimensions, window location, etc.) as well as the photometrical (reflection factors of internal walls, etc.) characteristics of the intervening elements, one could estimate the illuminance value on a particular surface (desk, computer screen, etc.) from the luminance values emerging from the fenestration system, obtained through equation (3-26) from the BTDF data set.
As this analysis requires taking a lot of factors into account, it would be quite fastidious if carried out manually. Daylight computer simulation software (e.g. Radiance or Relux) could therefore provide this kind of information on the basis of BTDF data sets and compare the expected illuminance values to the norms given in the literature.

By integrating the BTDF data into daylight simulation tools, computed simulations of the light propagation inside a given room can be rendered more easily and the information they provide can be used to predict the daylight distribution and to improve its use in building for the sake of sustainability.

4 CONCLUSION

Advanced fenestration systems, which include novel solar blinds, new glazing materials and daylight redirecting devices, can contribute to reduce energy consumption of buildings significantly, while simultaneously improving visual comfort conditions for users. Full knowledge of the light propagation characteristics through fenestration materials is, however, required to obtain a deeper propagation of daylight into the rooms of a building, larger solar gains in winter and lower solar loads in summer.

These rather variable features of fenestration materials can be formulated physically in terms of a Bi-directional Transmission Distribution Function (BTDF), which needs however, to be assessed experimentally though the appropriate photometric equipment.

A novel bidirectional transmission photogoniometer based on digital imaging techniques was designed and set up for this purpose.

After a detailed calibration and validation procedure, it was used to assess the BTDF of several new fenestration products produced by the company Baumann-Hüppe (industrial partner of the project). These data were used by the company to optimise and improve further the visual energy savings performance of their products.

Bidirectional photogoniometer design

The novel type of bidirectional transmission photogoniometer developed within the framework of this project, is made of three major components:
- a calibrated light source that provides a colllumated and spectrally optimal light beam
- a computer controlled movable mechanical support htat allows modifiying the incident light direction on the material sample (40 cmx 40 cm maximal size)
- a computer controlled "light detection device" that consists of a triangular flat projection screen associated to an image capturing camera (CCD video).

To overcome the difficulties encountered by existing photogoniometers (important BTDF data processing time, critical handling of materials with a high luminance range), the novel photogoniometer takes full advantage of advanced digital imaging techniques to obtain:
- a significant reduction in the BTDF data processing time (2-4 minutes instead of several hours for one incident angular direction)
- BTDF data based on quasi-continuous knowledge of the transmitted hemisphere (only discretised by the pixelisation of the images)
- handling of material samples with large dynamical ranges of luminances in transmission ("sharp" transmission figures).

Several other significant services are offered by this device, thanks to its BTDF data treatment capability, made possible by the use od figital image handling software (correction error sources, final graphical representation). This required several calibration procedures to maximise the experimental accuracy of this photogoniometric device.

Experimental Accuracy of the Photogoniometer

The use of digital video techniques (CCD camera) combined with digital image acquisition and handling software, has proven to be very fruitful and successful for this novel approach. The overall video system was, however, calibrated in a detailed and exhaustive manner to achieve an appropriate accuracy for the BTDF measurements. These calibration procedures were focused on the three main sources of experimental errors, which leads to:

- a spectral calibration, aiming to match the spectral response of the video system to the spectral sensitivity of human eyes
- a photometric calibration to allow the conversion of pixel grey levels into luminance values
- a geometrical calibration, linking couples of image pixel co-ordinates to the directions of the outgoing light ray of the material sample.

Other possible sources of experimental errors within the BTDF experimental assessment procedure were also examined; this includes:

- the stability and temperature sensitivity of the video system electronics (CCD sensor, amplifier circuits, etc.);
- the digital image non-uniformity and projection screen imperfect diffusion properties;
- the incident beam characteristics of the calibrated and collimated light source
- the perturbations due to the different sources of parasitic light.

A final assessment of the experimental accuracy of the photogoniometer was carried out throught theses different steps. A comparison of BTDF data, integrated through a numerical method or an Ulbricht integrating sphere, were performed to cross-check the reliability and accuracy of the novel photogoniometer. This comparison was consolidated using similar measurements of the hemispherical transmittance carried out by other international laboratories.

These empirical validations of the BTDF experimental assessment procedure show, in general, discrepancies lower than 10% in relative terms for most fenestration samples; it leads to relative errors lower than 20% for materials with complicated light transmission properties (such as prismatic films). This corresponds to a very satisfactory accuracy for figures as complex as BTDFs.

BTDF data valorisation and application

Special attention was paid to the treatment of BTDF data, to ensure better access to the numerical computer file and a better visualisation of the light transmission properties of the material samples. The following actions were undertaken:

- a data format was proposed and adopted on an international basis for the assessment of BTDF data ("Tregenza configuration")
- the structure of the BTDF computer data file was defined (ASCII format file)
- different types of graphical representations were set up with appropriate software, to visualise the photometric solids of the material samples (heispherical projection, axonometric view, C-planes cross-cutting).

All these BTDF data valorisation possbilities were used by the industrial partner of the project (Baumann-Hüppe Storen AG) to improve the quality and the competitivity of their products. The corresponding BTDF features of more than 20 different prototypes of novel solar blinds designed by the industrial partner were assessed using the bidirectional photogoniometer.

This leads to the following improvement of the products of the industrial partner:
- the optimisation of the luminous performance of an innovative blind design, especially with regard to visual comfort at VDT screens
- a better presentation of the product features for the different clients of the building construction sector
- a common physical description of the photometric transmission properties of these products.

All these advantages were used by the partner and found practical application as the company's novel products were used for different buildings all over Europe.

References

[And00] Andersen M., Michel L., Roecker C. and Scartezzini J.-L., "Experimental Assessment of Bi-directional Transmission Distribution Functions using Digital Imaging Techniques", Energy and Building "CISBAT'99 Special Issue", Elsevier Science, 2000

[And98] Andersen M., "Dispositif de mesure de la distribution de luminance du ciel basé sur des techniques d'imagerie numérique", Diploma report, EPFL, Lausanne, 97 p., 1998

[And99] Andersen M., "BTDF data of Baumann-Hüppe fenestration materials", Technical Report, EPFL, Lausanne, 1999

[Api94] Apian-Bennewitz P., “Designing an apparatus for measuring bidirectional reflection/ transmission”, SPIE 0-8194-1564-2, vol. **2255**, Fraunhofer Institute for Solar Energy Systems, Freiburg, pp. 697-706, 1994.

[Ayd97] Aydinli S. (1), "Report on Physical Quantities to be Measured in Laboratory Facilities", IEASHC Task 21, Technische Universität Berlin, 75 p., 1997

[Ayd99] Aydinli S. (ed.) (2), "Report on Physical Quantities to be Measured in Laboratory Facilities", IEASHC Task 21, Technische Universität Berlin, 50 p., 1999

[Bak95] Bakker L., van Dijk D., "Measuring and Processing Optical Transmission Distribution Functions of TI-materials", Private communication, TNO Building and Construction Research, Delft, 4 p., 1995

[Ber95] Berrutto V. et Fontoymont M., "Application of CCD Cameras to Lighting Research: Review and Extension to the Measurement of Glare Indices", CIE 119 23rd Round Session, pp.192-195, New Delhi, 1-8 November, 1995

[Ber96] Berrutto V., “Métrologie de la qualité visuelle des ambiances lumineuses. Application à l’éclairage des bureaux”, PhD Report, Université de Savoie, Chambéry, 209 p., 1996.

[Bre98] Breitenbach J., Rosenfeld J.L.J., "Design of a Photogoniometer to Measure Angular Dependent Optical Properties", Proceedings International Conference on Renewable Energy Technologies in Cold Climates, pp. 386-391, 4-6 May, Montreal, Canada.

[CIE87] Commission Internationale de l’Eclairage, « Methods of characterising illuminance meters and luminance meters. Performance, characteristics and specifications », CIE **69**, 36 pp., 1987.

[CIE98] Commission Internationale de l'Eclairage, "Practical methods for the measurement of reflectance and transmittance", CIE 130, 1998

[CSD97] Council for Sustainable Development, "Sustainable Development: Action Plan for Switzerland", Swiss Federal Office for Environment, Forest and Landscape, BUWAL, Bern 1997

[IES84] « IES Lighting Handbook, Application and Reference Volume », Illuminating Engineering Society of North America, New York, 1984.

[IES93] Illuminating Engineering Society of North America, "Lighting Handbook", New York, 1993

[Mic99] Michel L., “Méthode expérimentale d’évaluation des performances lumineuses de bâtiments”, PhD Report, EPFL, Lausanne, 209 pp.,1999.

[NBS77] Geometrical Considerations and Nomenclature for Reflectance, NBS Monograph 160, National Bureau of Standards, Washington, 1977

[Och96] Ochi S., Lizuka T. et al., "Charged-Coupled Device Technology", Japanese Technology Reviews, Vol. 30, Section A, Electronics, Amsterdam, 1996

[OFQC94] Office Fédéral des Questions Conjoncturelles, “Eclairage des bureaux”, Programme d’action RAVEL “Utilisation rationnelle de l’électricité”, n° OCFIM 724.329.2f, Berne, 108 p.,1994.

[Pap88] Papamichael K., Klems J., Selkowitz S., "Determination and Application of Bi-directional Solar-Optical Properties of Fenestration Materials", LBL-25124, Lawrence Berkeley Laboratory, USA, 8 p., 1988

[Pas94] Pasini I.C. and Transley B.W., "Assessing the Luminous Environment with IQ CAM SCENE Video Photometer/Colorimeter", Light Wave, IESNA Conference 1994

[Rav95] Programme d'action RAVEL, "La lumière naturelle à bon escient / Neuer Komfort mit Tageslicht", EDMZ, Berne, 1995

[Sca97] Scartezzini J.-L., Compagnon R., Roecker C. and Michel L., "Bi-directional Photogoniometer for Advanced Glazing Materials Based on Digital Imaging Techniques", Lighting Research and Technology, 29 (4), pp. 197-205, London 1997

[Sca99] Scartezzini J.-L. and Courret G., "Anidolic Daylighting Systems", Submitted for publication in Solar Energy, 1999

[SLG92] Schweizerische Lichttechnische Gesellschaft, "Handbuch für Beleuchtung", Ecomed Verlag, Landsberg, 1992

[Tre87] Tregenza P.R., “Subdivision of the sky hemisphere for luminance measurements”, *Lighting Research and Technology*, vol. **19**, CIBSE, London, 2 p., 1987.

[War92] Ward G.J., "Measuring and Modeling Anisotropic Reflection", Computer Graphics, vol. 26 (2), 1992

[War92] Ward G.J., "Measuring and Modeling Anisotropic Reflection", Computer Graphics, Vol. 26 (2), 1992

[Wir97] Wirth H., Gombert A., Wittwer V., Luther J., "Sun Protection and Daylighting with New Angular Selective Structures", Proc. of CISBAT'97 Conference, EFL, 1/2 October 1997

[Wir99] Wirth H., "Richtungsselektive Steuerung von Sonnenstrahlung durch Fenster", Doktorarbeit, EPFL, Lausanne, 1999

[Wri69] H. Wright, C.L. Sanders, D. Gignac, "Design of Glass Filter Combinations for Photometers", *Applied Optics*, vol. **8** (12) , 7 pp., 1969

Annex A

Plan and cross-section view of the bi-directional photogoniometer (final mechanical concept)

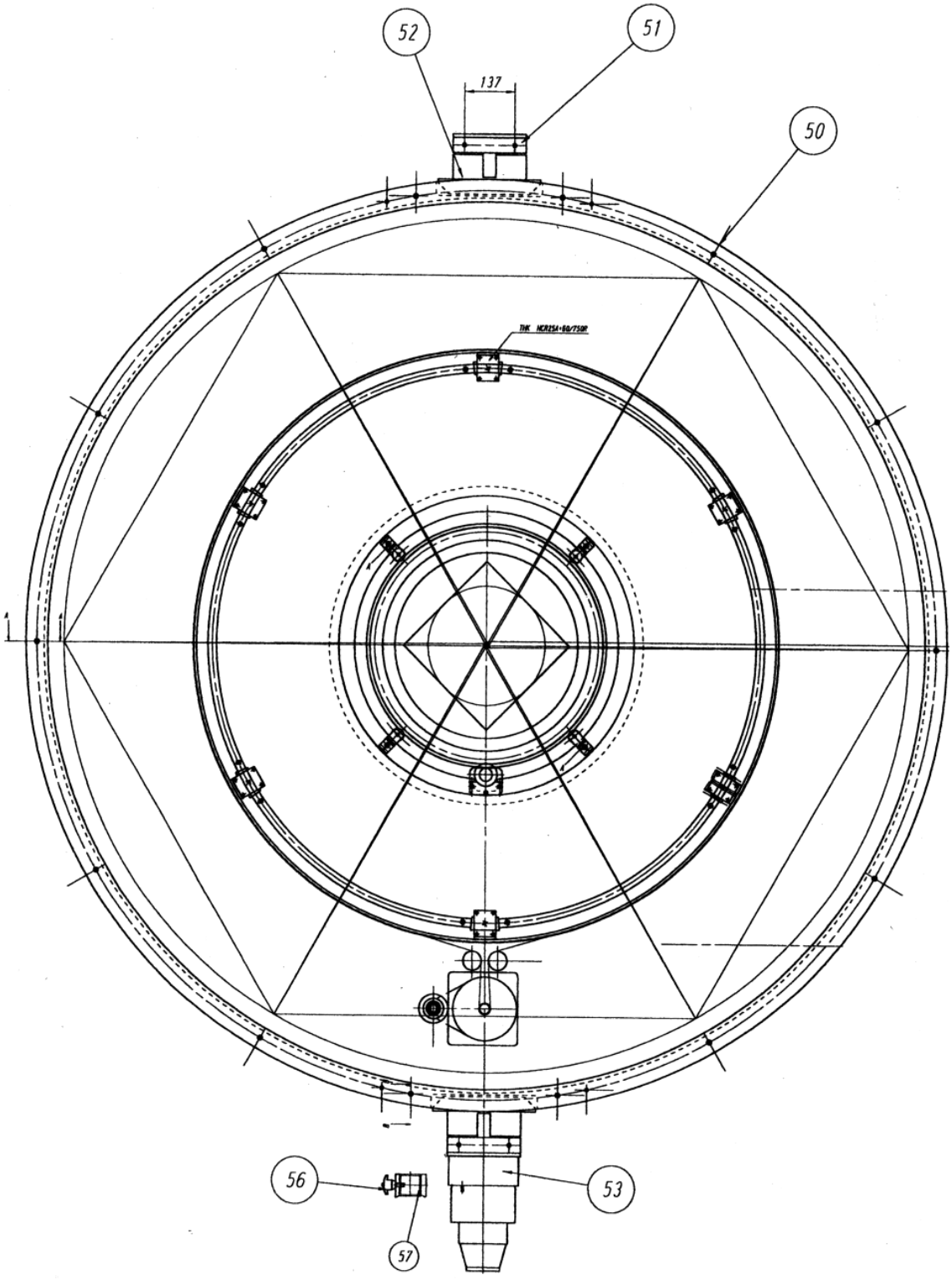

Bi-directional Photogoniometer (1)

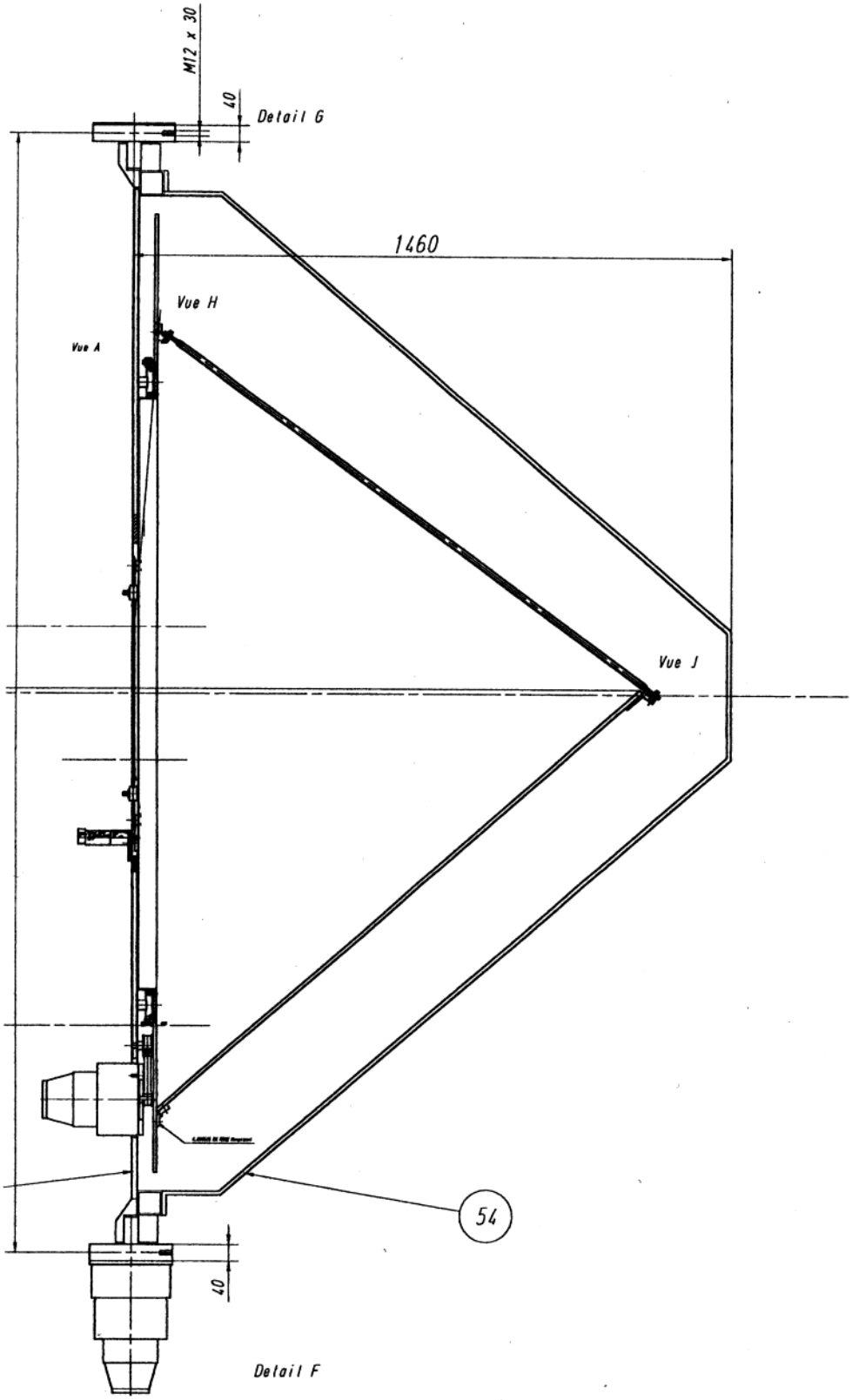

Bi-directional Photogoniometer (2)

Annex B

Data format of bi-directional measurements

The characterisation of a daylighting system with respect to different incident and emerging angles of the light flux requires the definition of a co-ordinate system, preferably based on international agreements.

Within the framework of Task 21 of the International Energy Agency, a common format was determined [Ayd99]:

- The **origin** of the co-ordinate system is placed on the daylighting component. Directions are defined by **spherical co-ordinates**: altitude angle θ_i, comprised between 0° and 90°, and azimuth angle ϕ_i, comprised between 0° and 360° (see Fig. B.1). Index i indicates whether it is related to the incident (i = 1) or transmitted (i = 2) direction.

  In order to avoid any confusion between files providing BTDFs and BRDFs (bi-directional reflection distribution functions), the altitude angle θ'_2, defined as the supplementary angle of θ_2 (i.e. as the angle between the normal to the sample on the incident interface and the emerging light flux direction, see Fig. B.1), is used to give the outgoing direction in the final data files; it is therefore comprised between 90° and 180°.

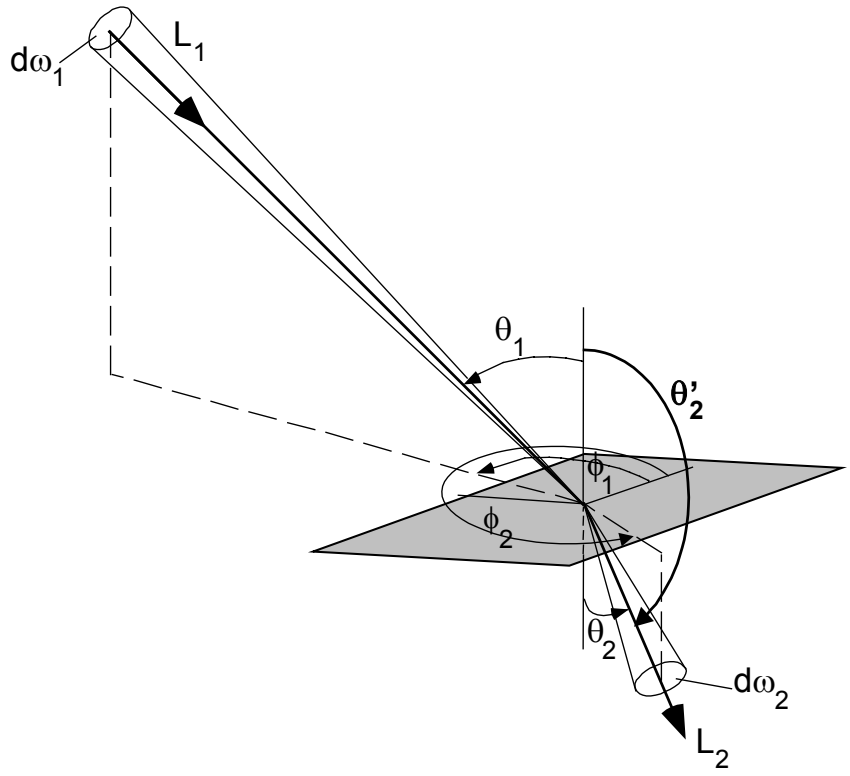

Fig. B.1. Co-ordinate system for bi-directional transmission measurements.

- The relative position of a component to the co-ordinate system being of huge impact to the measurement results, the **orientation** of the sample must be precisely defined as well.

  The following rules, illustrated by Fig. B.2, apply to the adjustment:

  - The sample plane is parallel to a vertical window plane (i.e. the z-axis, orthogonal to the sample element, points horizontally)
  - If a particular direction appears on the sample, e.g. because of slats, colour lines, a prismatic shape, etc., the orientation of the sample within the x-y plane is defined in order to have this privileged direction collinear to direction $\phi_i = 0°$ (see Fig. B.2).
  - The positive z-axis is the outside direction of the sample.

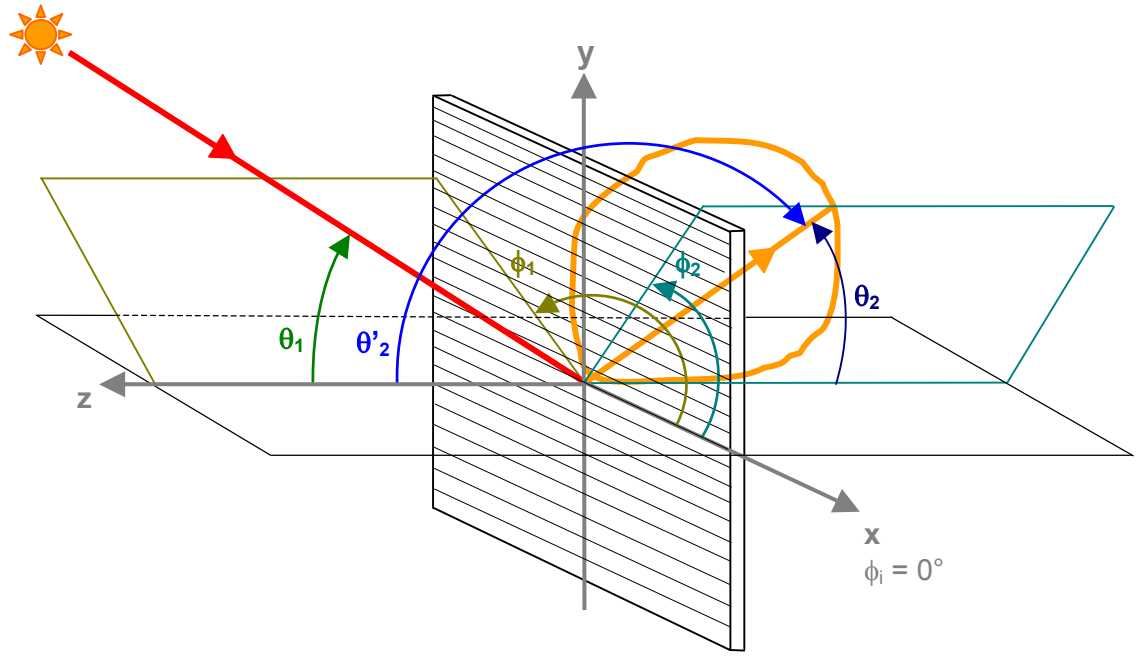

Fig. B.2. Orientation of daylighting system with regard to the co-ordinate system.

- It is agreed that the default set of incident directions conforms to the sky luminance distribution defined by **Tregenza** [Tre87]. This leads to 145 different light incidence directions which are shown on Fig. B.3.

  If the sample presents any **symmetry**, the set of 145 directions can be reduced in a way described by Table B.1. This reduction is automatically applied, if the selected exploration type consists of the whole set of 145 directions matching the Tregenza configuration (as illustrated on Fig. 3.26), and if the symmetry indicator is non null (see Fig. 3.28A).

  Of course, depending on the manufacturer's desires, the incident directions set can be different from this configuration, as explained in § 3.3.1.

θ_1	ϕ_1-step	ϕ_1	**Light incidents must be measured for:**
0°	-	0°	All samples
12°	60°	0°, 60°	All samples
24°	30°	0°, 30°, 60°, 90°	All samples
36°	20°	0°, 20°, 40°, 60°, 80°	All samples
48°	15°	0°, 15°, 30°, 45°, 60°, 75°, 90°	All samples
60°	15°	0°, 15°, 30°, 45°, 60°, 75°, 90°	All samples
72°	12°	0°, 12°, 24°, 36°, 48°, 60°, 72°, 84°	All samples
84°	12°	0°, 12°, 24°, 36°, 48°, 60°, 72°, 84°	All samples
For rotational symmetry, only measurements for θ_1 = 0°, 12°, 24°, 36°, 48°, 60°, 72° and 84° need to be done.			
			Additional Measurements, if the sample is asymmetric to:
12°	60°	120°, 180°	ϕ_1= 90° / 270°
24°	30°	120°, 150°, 180°	ϕ_1= 90° / 270°
36°	20°	100°, 120°, 140°, 160°, 180°	ϕ_1= 90° / 270°
48°	15°	105°, 120°, 135°, 150°, 165°, 180°	ϕ_1= 90° / 270°
60°	15°	105°, 120°, 135°, 150°, 165°, 180°	ϕ_1= 90° / 270°
72°	12°	96°, 108°, 120°, 132°, 144°, 156°, 168°, 180°	ϕ_1= 90° / 270°
84°	12°	96°, 108°, 120°, 132°, 144°, 156°, 168°, 180°	ϕ_1= 90° / 270°
12°	60°	300°	ϕ_1= 0° / 180°
24°	30°	270°, 300°, 330°	ϕ_1= 0° / 180°
36°	20°	280°, 300°, 320°, 340°	ϕ_1= 0° / 180°
48°	15°	270°, 285°, 300°, 315°, 330°, 345°	ϕ_1= 0° / 180°
60°	15°	270°, 285°, 300°, 315°, 330°, 345°	ϕ_1= 0° / 180°
72°	12°	276°, 288°, 300°, 312°, 324°, 336°, 348°	ϕ_1= 0° / 180°
84°	12°	276°, 288°, 300°, 312°, 324°, 336°, 348°	ϕ_1= 0° / 180°
12°	60°	240°	ϕ_1= 0° / 180° **and** ϕ_1= 90° / 270°
24°	30°	210°, 240°	φ_1= 0° / 180° **and** φ_1= 90° / 270°
36°	20°	200°, 220°, 240°, 260°,	φ_1= 0° / 180° **and** φ_1= 90° / 270°
48°	15°	195°, 210°, 225°, 240°, 255°	φ_1= 0° / 180° **and** φ_1= 90° / 270°
60°	15°	195°, 210°, 225°, 240°, 255°	φ_1= 0° / 180° **and** φ_1= 90° / 270°
72°	12°	192°, 204°, 216°, 228°, 240°, 252°, 264°	φ_1= 0° / 180° **and** φ_1= 90° / 270°
84°	12°	192°, 204°, 216°, 228°, 240°, 252°, 264°	φ_1= 0° / 180° **and** φ_1= 90° / 270°

Table B.1. Light Incidences based on the Tregenza configuration, accounting for sample symmetries.

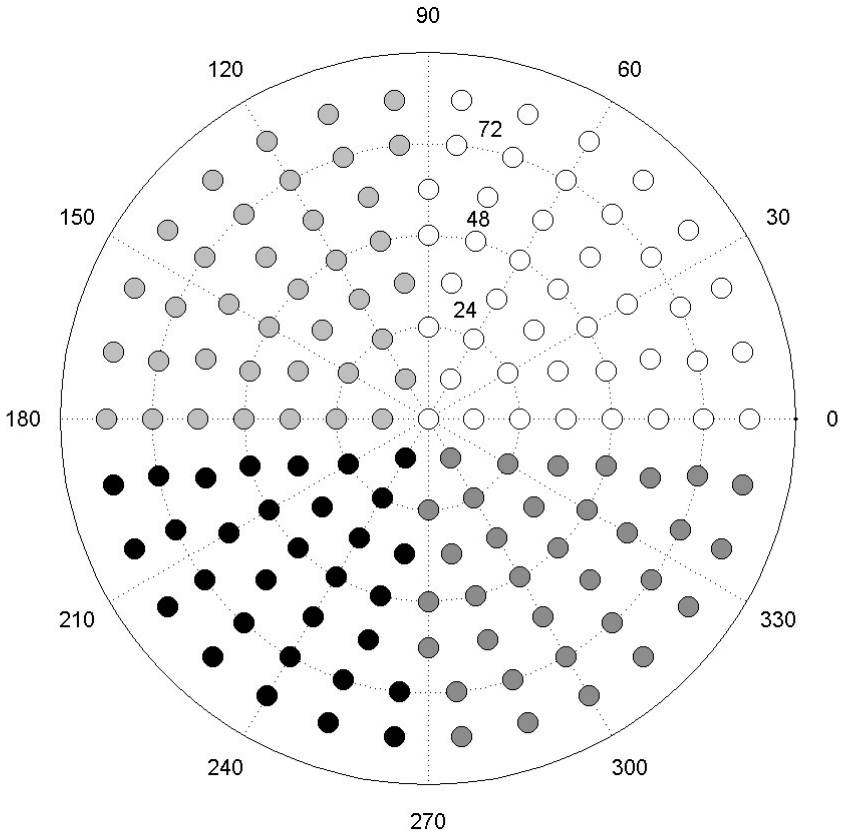

Fig. B.3. Default set of 145 light incidence directions for bi-directional measurements, matching the subdivision of the sky hemisphere for luminance measurements defined by Tregenza. The grey levels associated to the different directions correspond to the backgrounds appearing in Table B.1.

- The **storage** of the bi-directional data is realised through the creation of ASCII-format files (for device independence), with a header section containing all the information about the measurement set-up and the sample. The following data section is divided into three columns separated by a tab character (ASCII code 9): ϕ_2, θ_2, BTDF. An example of file contents is given below. The amount of data being of great importance for a sample, it is recommended to have a single file for each light incidence.

  For convenience reasons, it is useful to put the **filenames** into a system. Four pieces of information are contained in a BTDF data filename:

  - The institution carrying out the measurements
  - The sample name
  - The light incidence angle θ_1
  - The light incidence angle ϕ_1

  The file given below would for instance be named: “leso_Example_50_90.txt”.

```
#material: Example
#manufacturer: Unknown
#Isym = 0       ! symmetry indicator: 0 no symmetry (phi_1 = 0°...360°)
#               1 rotary symmetry (only for one phi_1)
#               2 symmetry to phi=0° and phi=180° (phi_1 = 0°...180°)
#               3 symmetry to phi=90° and phi=270° (phi_1 = -90°...90°)
#               4 symmetry to phi=0° and phi=180° & to phi=90° and phi=270° (phi_1 = 0°...90°)
#considered area [cm2]: 78.54
#thickness [cm]: 2.65
#comments: additional comments about the sample or the characterisation parameters
#measurements done at the Solar Energy and Building Physics Laboratory, LESO-PB/EPFL
#measurements and processing by Marilyne Andersen
#date of measurement: 08.03.00
#contact Marilyne.Andersen@epfl.ch for details
#light incidence :
#phi_1: 90° (azimuth)
#theta_1: 50° (altitude)
#BTDF values averaged over output directions from (phi_2 - 7.5) to (phi_2 + 7.5) in azimuth
#and from (theta_2 - 5.0) to (theta_2 + 5.0) in altitude
#measurements not performed for theta_2 < 95.0
#light transmittance: 0.09
#light transmittance calculated from BTDF values, with extrapolated values for 90 < theta_2 < 95.0
#data
#phi_2  theta_2  BTDF
0       100      0.030
15      100      0.028
30      100      0.018
45      100      0.021
60      100      0.021
75      100      0.018
...     ...      ...
315     100      0.018
330     100      0.016
345     100      0.028
0       110      0.030
15      110      0.030

[a.s.o.]

330     170      0.042
345     170      0.048
0       180      0.052
END
```

Annex C

Solar blinds, manufactured by Baumann-Hüppe AG, characterised through BTDF measurements

An important set of solar blind prototypes was provided by the industrial partner Baumann-Hüppe AG for optimisation and testing on the basis of BTDF measurements. The list of analysed samples is given in this chapter, with their names and properties. The complete catalogue of performed measurements may be found in [And99].

D O L A N

Fabric blinds

- DOLAN 1111 red
- DOLAN 1127 white
- DOLAN 1128 silver grey
- DOLAN 1134 pearl grey

D O L A N D U O C O L O R

Fabric blinds, coloured stripes

- DOLAN DUO COLOR 1234 silver / white
- DOLAN DUO COLOR 1245 cherry / white
- DOLAN DUO COLOR 1247 green / white

P A N A M A

Fabric blinds

- PANAMA 4201 paloma (white)
- PANAMA 4205 strada (pearl grey)

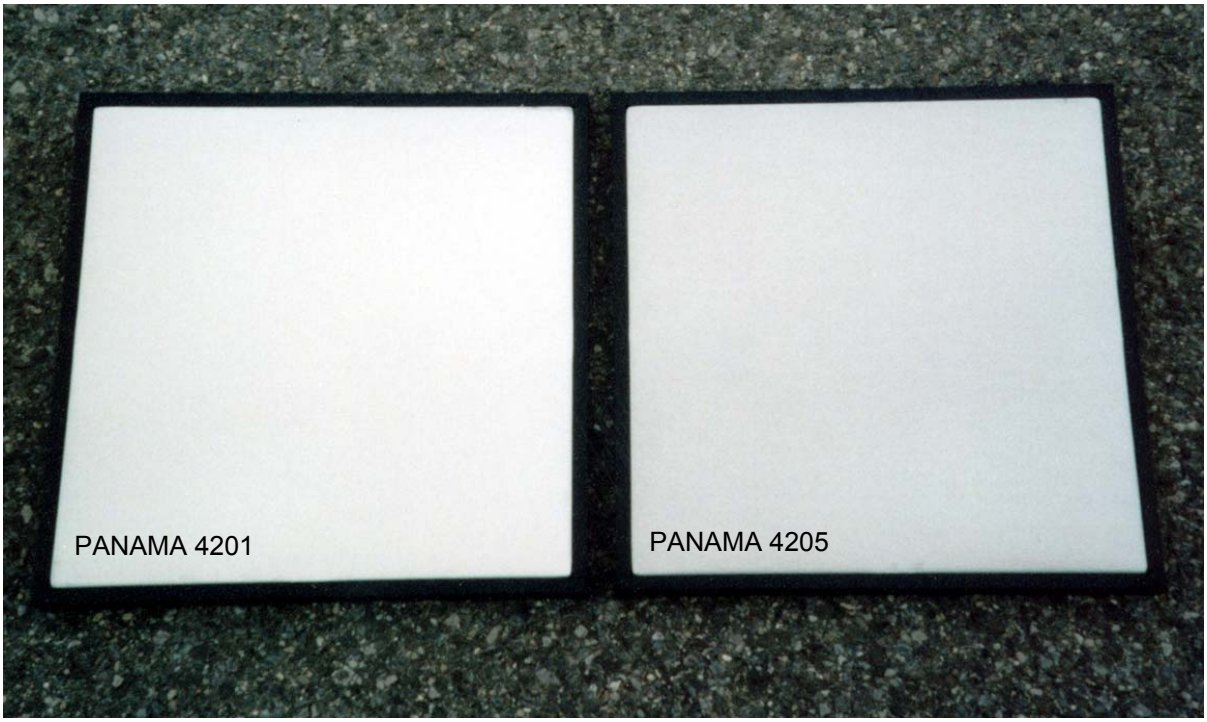

P L I S S E E

Thin pleated fabric blinds

- PLISSEE 1109 standard, semi-transparent (mat silver grey)
- PLISSEE 3014 coating of vaporised aluminium, semi-transparent (shiny pearl grey)
- PLISSEE 3141 standard, not transparent (shiny silver grey)
- PLISSEE 4041 coating of vaporised aluminium, not transparent (shiny pearl grey)
- PLISSEE 4042 coating of vaporised aluminium, opaque (shiny pearl grey)

R O L L O

Thick fabric blinds

- ROLLO 7520 coating of vaporised aluminium (grey)
- ROLLO 9451 coating of vaporised aluminium, opaque (pearl grey)
- ROLLO 9563 foil (dark grey)

S H A D O W

Hatched fabric blinds with coloured stripes

- SHADOW 4120 mirabel / white
- SHADOW 4123 grey / white

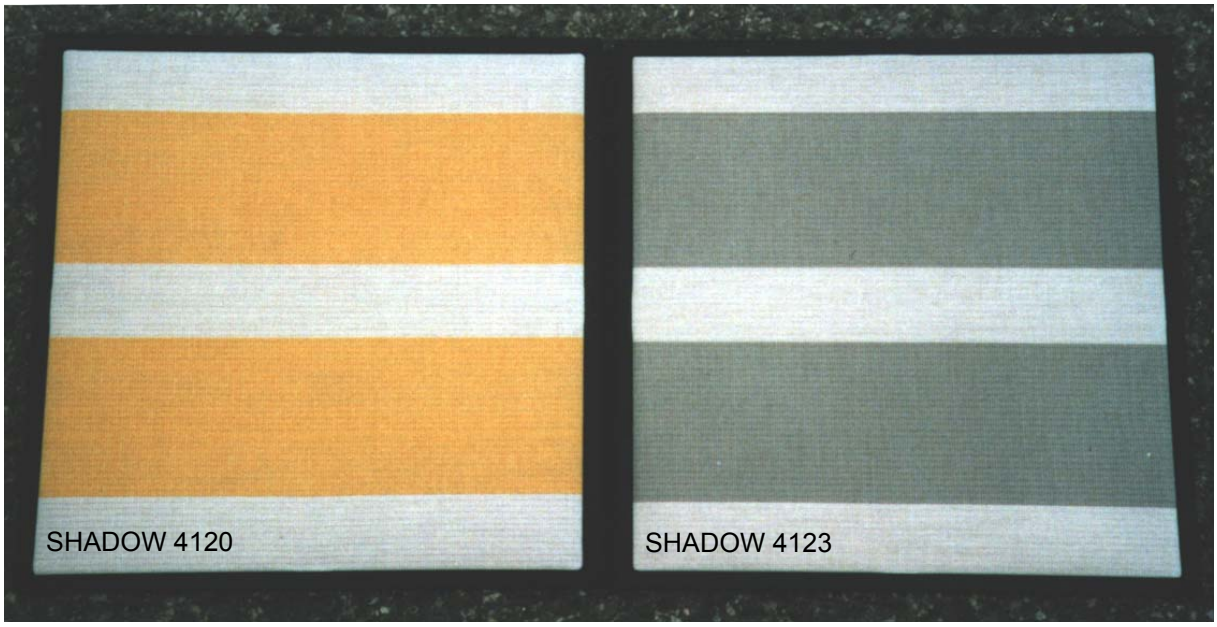

VENETIAN BLINDS

Metallic slats, inclination angle fixed to 30°

- White slats — conventional shape and coating
- Brown slats — conventional shape and coating
- Grey slats — conventional shape and coating
- SHINE — pearl grey slats, optimised shape (spoon profile) and coating (quartz painting used for car body manufacturing)

ACKNOWLEDGEMENTS

The following institutions and/or people supported this project:

- the Commission for Technology and Innovation (CTI) of the Swiss Federal Government, who financed the institutional part of this project
- the Swiss Federal Institute of Technology in Lausanne (EPFL) who provided financial support for the experimental equipment
- the Baumann-Hüppe company, our industrial partner for the project who provided manpower
- Dr. Paul-Eric Gygax, member of the CTI commission, who ensured the follow-up of the project
- Messrs D. Glauser, P. Loesch and F. Leresche, for their considerable contribution to the development of the photogoniometer

The authors express their warm thanks to all of them.